Decay Studies

of Neutron-Rich Nuclei

Thesis submitted in accordance with the requirements of
the University of Liverpool for the degree of Doctor in Philosophy

by

Alan Thomas Reed

Oliver Lodge Laboratory

January 1999

It is a much cleverer thing to talk nonsense than to listen to it.

Oscar Wilde

This thesis is dedicated to my family.

Abstract.

Nuclei near the neutron drip line have been studied following the fragmentation of a ^{36}S beam at an energy of 77.7 MeV/A. The nuclei were separated in-flight using the LISE3 spectrometer and identified through time of flight and energy loss measurements. The γ-rays emitted following the β-decay of ^{17}B, ^{18,19}C, ^{20,21}N, ^{24}O, $^{25-27}$F and $^{28-30}$Ne have been measured. The β-delayed γ-rays emitted from ten of these nuclei have been measured for the first time. The γ-ray energy spectra produced from some of the above nuclei have been compared with shell model calculations and level energies deduced from transfer reactions where available. Further measurements of half-lives have been performed on ^{19}B and ^{29}F. From these measurements it has been possible to obtain $\log_{10} ft$ values for the β-decay transitions which have given spin and parity assignments for some of the parent and daughter states.

Analysis of the β-delayed neutron emission data of some of the above nuclei was carried out in parallel to this work.

Acknowledgements.

I would like to thank Professors P.J. Twin and E. Gabathuler for allowing me to pursue this research at the University of Liverpool and for Professor Twin for financial support throughout my Ph.D.

Dr. R.D. Page for providing me with an interesting and fascinating research project and for his supervision throughout and especially for his attempts to try and teach me the finer points of red wine.

I would like to thank everyone who was on and involved in the experiment and to the support crew at GANIL, there are too many to mention but many thanks must go to Oleg Tarasov for helping me with some of the analysis and to Marek Lewitowicz, without whom none of this would have been possible.

Many thanks to the computer support team at Liverpool, especially John Cresswell and Janet Sampson for helping me with all my sorting problems. Also much appreciated is Andrew Boston for allowing me to hassle him with all my computer problems and to Dave Cullen as well for his programming help and for never letting me forget about ^{172}Hf.

All the effort put in by Paddy Regan, Anna Wilson and Katie Chandler for proof-reading this work is very much appreciated. Also thanks to Dave Cullen for reading some of the work presented here.

Big thanks to everyone who has played football over the last three years especially Kevin Cann, Roger Allatt and Dion Harris.

This would never have been completed without the help of Neil, Jamie, Sarah, Adrian, Steven, Mike, Paul, Ailsa, Katie and the G-man. They gave me an escape route every now and again, and for that they cannot be thanked enough.

Contents

Chapter 1

Aspects of Light Neutron-Rich Nuclei.

Nuclei possessing neutron/proton ratios radically larger than those of stable isotopes can exhibit unexpected phenomena such as neutron halos and the changing of the shell closures. It is only for the lightest elements that nuclei at the neutron drip line can presently be accessed experimentally and their properties investigated. In addition comparatively little is known about their radioactive decay characteristics. Such measurements can probe important details of the underlying microscopic structure of these nuclei. The nuclei close to the drip line are of particular interest as they should show some unique properties due to their very small one- or two-particle separation energies.

1.1 The Neutron Drip Line.

The drip lines represent the point where it is energetically not favourable to keep adding nucleons onto a nucleus. Neutrons experience no Coulomb repulsion and as a consequence the neutron drip line extends farther away from the valley of stability than the proton drip line, figure 1.1, and the difficulties in synthesising nuclei with such large excesses of neutrons means that only for the lightest nuclei has the drip line been approached for neutron-rich nuclei.

Mass models can be a useful tool to predict the position of the neutron drip line [Haus 88] as well as the one- and two- particle separation energies of the nuclei at the drip line. The
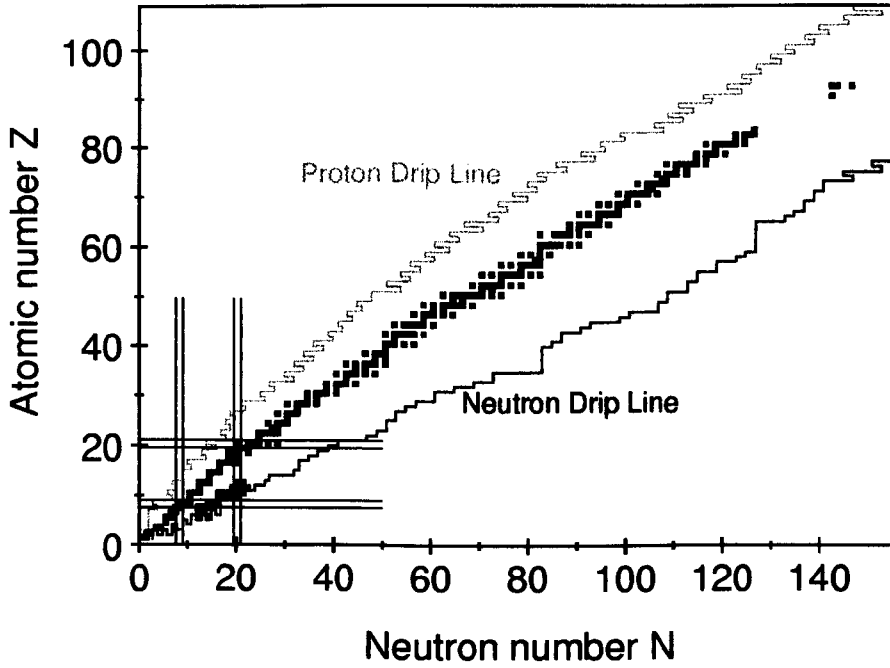
Figure 1.1: Chart of the nuclides showing the predicted proton and neutron drip lines [Haus 88]. The black squares show the stable nuclei. Compared with the proton drip line, the neutron drip line lies a long way off from the valley of stability for heavy nuclei. Also drawn on are the positions of the magic numbers 8 and 20 for neutrons and protons.

Bethe-Weizsacke semi-empirical mass formula describes the variation of mass with proton (Z), neutron (N) and atomic number (A) and is given as

$$M(A, Z) = Zm_H + (A - Z)m_n - B(N, Z),$$ (1.1)

where m_H and m_n are the masses of a hydrogen atom and a neutron respectively $B(N, Z)$ is the nuclear binding energy which is the energy gained by amalgamating the neutrons and protons instead of keeping them apart. Alternatively the formula can be written as:

$$M(A, Z) = Zm_H + (A - Z)m_n - a_v A + a_s A^{\frac{2}{3}} + a_C Z^2 A^{-\frac{1}{3}} + a_a (A - 2Z)^2 A^{-1} + \delta.$$ (1.2)

The first two terms give the total mass of the protons and neutrons in a nucleus and the latter terms the total binding energy of the nucleus. The volume term, $a_v A$, gives the binding energy proportional to the number of constituent nuclei; $a_s A^{\frac{2}{3}}$ is the surface

correction term; $a_C Z^2 A^{-\frac{1}{3}}$ represents the classical Coulomb repulsion of the protons in the nucleus; $a_a (A - 2Z)^2 A^{-1}$ reflects the tendency of stable nuclei to have approximately equal proton and neutron numbers and the final term δ is a consequence of the pairing interaction between like-nucleons which is zero for even-odd nuclei; positive for odd-odd nuclei and negative for even-even nuclei and accounts for the increased stability observed for nuclei which have an even number of like nucleons.

In terms of the semi-empirical mass formula it is possible to map the region of nuclear stability with respect to various break-up and transformation phenomena such as β-decay and neutron and proton emission. For the β-stability region, the mass formula has the condition

$$\left(\frac{\delta M(A, Z)}{\delta Z} \right)_{A=const} = 0. \tag{1.3}$$

With the increase in neutron excess the binding energy, B, of the last neutron will decrease and its value will become extremely small as the drip line is approached. The heaviest attainable isotope of a given element corresponds to zero neutron separation energy, or

$$\left(\frac{\delta B}{\delta N} \right)_{Z=const} = 0, \tag{1.4}$$

which corresponds to the neutron drip line [Beth 68].

At the time of writing the neutron drip line has probably been determined for elements lighter than neon [Tara 97a, Saku 98].

1.2 Neutron Halo Nuclei.

Many exotic structures have been observed near the drip lines and one of the most interesting discoveries has been that of neutron halo nuclei, e.g. ^{11}Li [Tani 85] which was the first observed case of a neutron halo. Other nuclei that are considered to have neutron halos are ^{6}He, ^{11}Be, ^{14}Be and ^{17}B [Tani 96]. A particularly interesting aspect of such nuclei is that, in some cases, it is a three-body interaction which stabilises the nucleus. That is, for some halo nuclei, if one-neutron is removed the resulting isotope is particle unstable.

In nuclei near the drip line the separation energy of the last nucleon(s) becomes extremely small compared with the common 6-8 MeV in stable nuclei. The one- or two-nucleon separation energy can be less than 1 MeV at the drip line, and this low binding energy can

lead to quantum mechanical tunnelling of the neutron(s) away from the core. The simplest case is that of a single odd neutron, e.g. ^{11}Be which has a single neutron orbiting a ^{10}Be core. There are some cases in which the core cannot bind one neutron but can bind two, as in the case of ^{11}Li, because additional energy is gained from the attractive n-n interaction.

The neutron halo arises from the neutron density distribution which shows an extremely long tail in loosely bound nuclei. Although the density of a halo is very low compared to the core, it strongly affects the reaction cross section. By measuring interaction cross sections Tanihata *et al.* [Tani 85] yielded nuclear cross sections that were considerably larger than expected for the $A^{1/3}$ dependence that one would expect for approximately constant density distribution. Figure 1.2 shows that there is a sudden increase in the nuclear radii for ^{11}Li, ^{11}Be, ^{14}Be and ^{17}B. The charge radius in light neutron-rich nuclei in an isotopic sequence
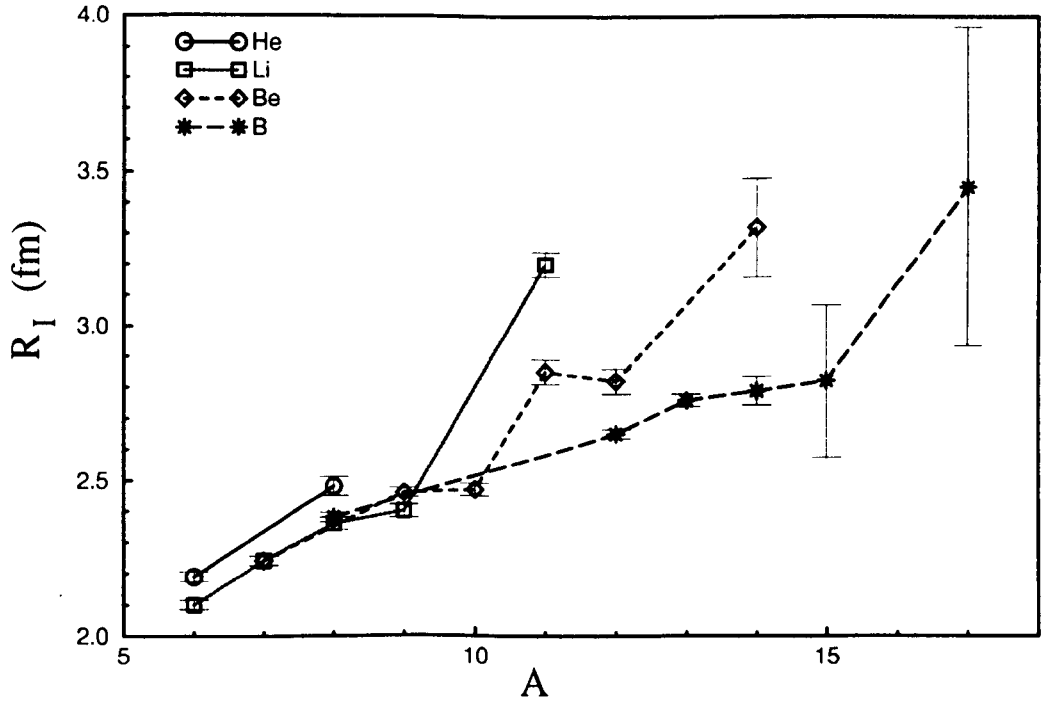
Figure 1.2: Interacting radii for some light nuclei determined from their interaction cross sections. The interaction radius (R_I) is defined by $\sigma_I = \pi[R_I\,(P)\ +\ R_I\,(T)]^2$, where P and T are the projectile and target respectively. Sudden increases of matter radii are seen for nuclei near the neutron drip line. Taken from [Tani 96].

should remain essentially constant as neutrons are added and Bertsch *et al.* [Bert 89] found, for example, that the charge radii (r_c) for ^{7}Be to ^{14}Be change by 0.14 fm while the matter radius (r_m) varies by 1.52 fm.

From Heisenberg's uncertainty principle for the space-momentum relationship, the large size of the neutron halo implies a narrow momentum distribution. Kobayashi *et al.* [Koba 88] found that the momentum distributions from the fragmentation of halo nuclei were much narrower than those from ordinary nuclei.

Except for ^{11}Be and ^{19}C, all known halo nuclei have a pair of neutrons in the last orbital and these nuclei have therefore a three-body configuration of two loosely bound neutrons and a core which is more bound. Many three body calculations have been reported [Proc 95] to study the three body structures of halo nuclei although no experiments have been performed to study the special three body structures of these nuclei.

1.3 Neutron Rich Nuclei in the Region Around N = 20.

The shell model explains how the nucleus is made up of a series of nuclear shells in a way analogous to that of the shell structure of electrons in an atom. Shell closures are evident due to the increase in proton and neutron separation energies at certain numbers and there is an increase in the energy of the 2^+ state in even-even nuclei at the shell closures (called *magic numbers*, Z or N = 2, 8, 20, 28, 50, 82, 126). Figure 1.3 shows where the shells arise as a function of nuclear deformation. Nuclei at the magic numbers should not be deformed. Only those nuclei away from the magic numbers, in mid-shell should show such a property.

Previous studies of neutron-rich nuclei in the region $N \approx 20$, $Z \approx 10$ have concentrated mainly on the nuclei ^{31}Na [Guil 84, Klot 93] and ^{32}Mg [Guil 84, Moto 95]. These nuclei are of particular interest since they both have 20 neutrons which represents a magic number shell closure in the region of nuclear stability, figure 1.3. Recent experiments on ^{31}Na and ^{32}Mg [Guil 84, Klot 93, Moto 95] have questioned the validity of this shell closure near the neutron drip line. These nuclei have been shown to have unexpected physical properties: ^{31}Na has an anomalous ground state spin for an *sd* shell nucleus ($3/2^+$) [Hube 78]; the excitation energy of the 2^+ state in ^{32}Mg [Detr 79] is only 885 keV, indicating nuclear deformation. The binding energies of these two nuclei and the two-neutron separation energy, S_{2n}, values are also higher than expected [Thib 75, Detr 83]. These measurements
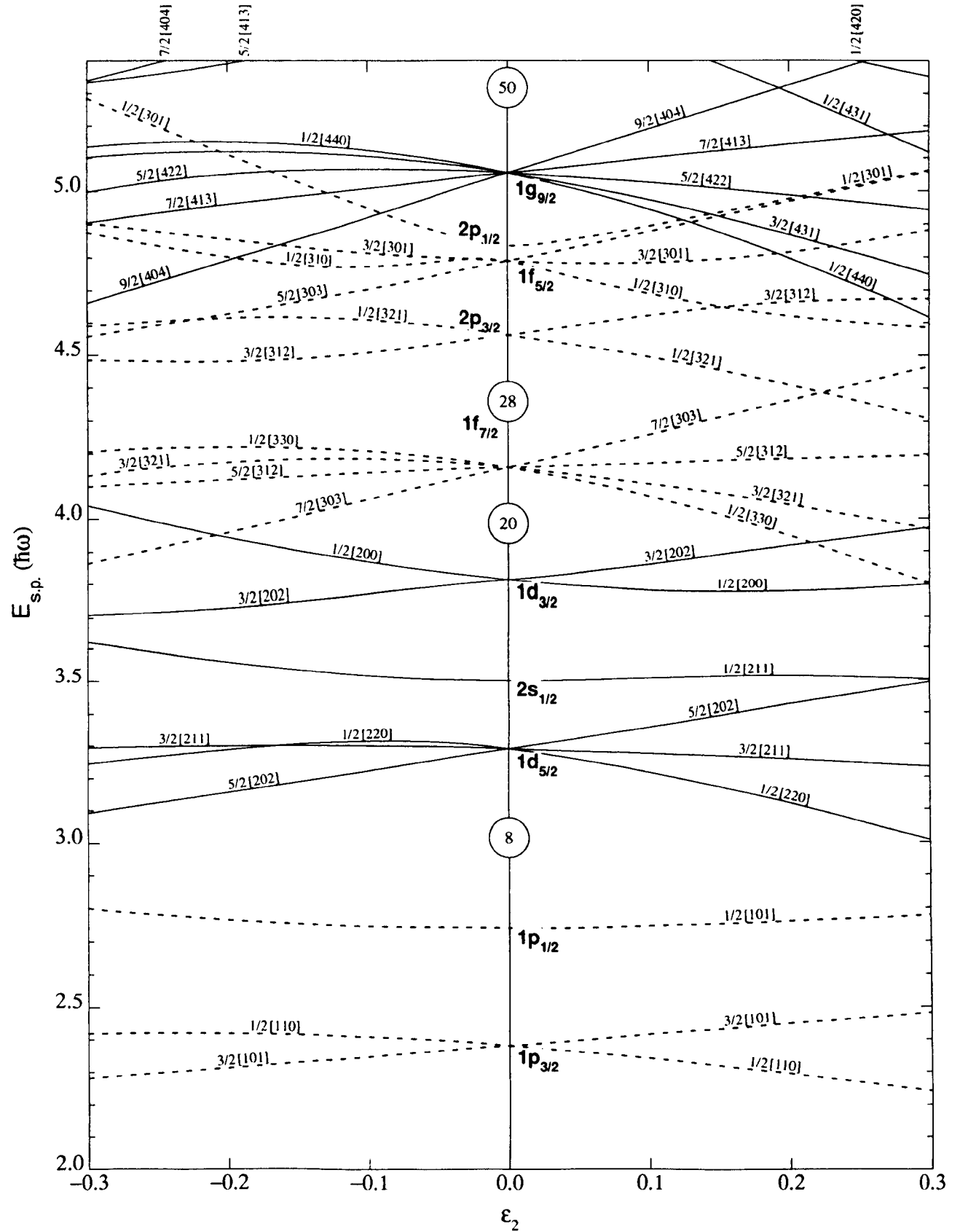
Figure 1.3: Level scheme of the Nilsson model [Nils 55] for protons or neutrons in light nuclei as a function of the deformation parameter ϵ_2. The magic numbers appear at zero deformation where there are large shell gaps.

have led to the suggestion of a new region of deformation and to the collapse of the magic $N = 20$ shell closure at the neutron drip line.

Investigations of the anomalies in the $A \approx 32$ region via the shell model began when Wildenthal and Chung [Wild 80] showed that the binding energies of the $N = 20$ Na and Mg isotones could not be understood on the basis of shell model interactions with the active orbits constrained to the $2s_{1/2}$ and $1d_{3/2}$ major shell alone. They spoke of an *island of inversion*, figure 1.4, with the $1f_{7/2}$ and $2p_{3/2}$ orbitals being preferentially populated rather than the expected $2s_{1/2}$ and $1d_{3/2}$ orbitals. Calculations [Watt 81, Stor 83] which included
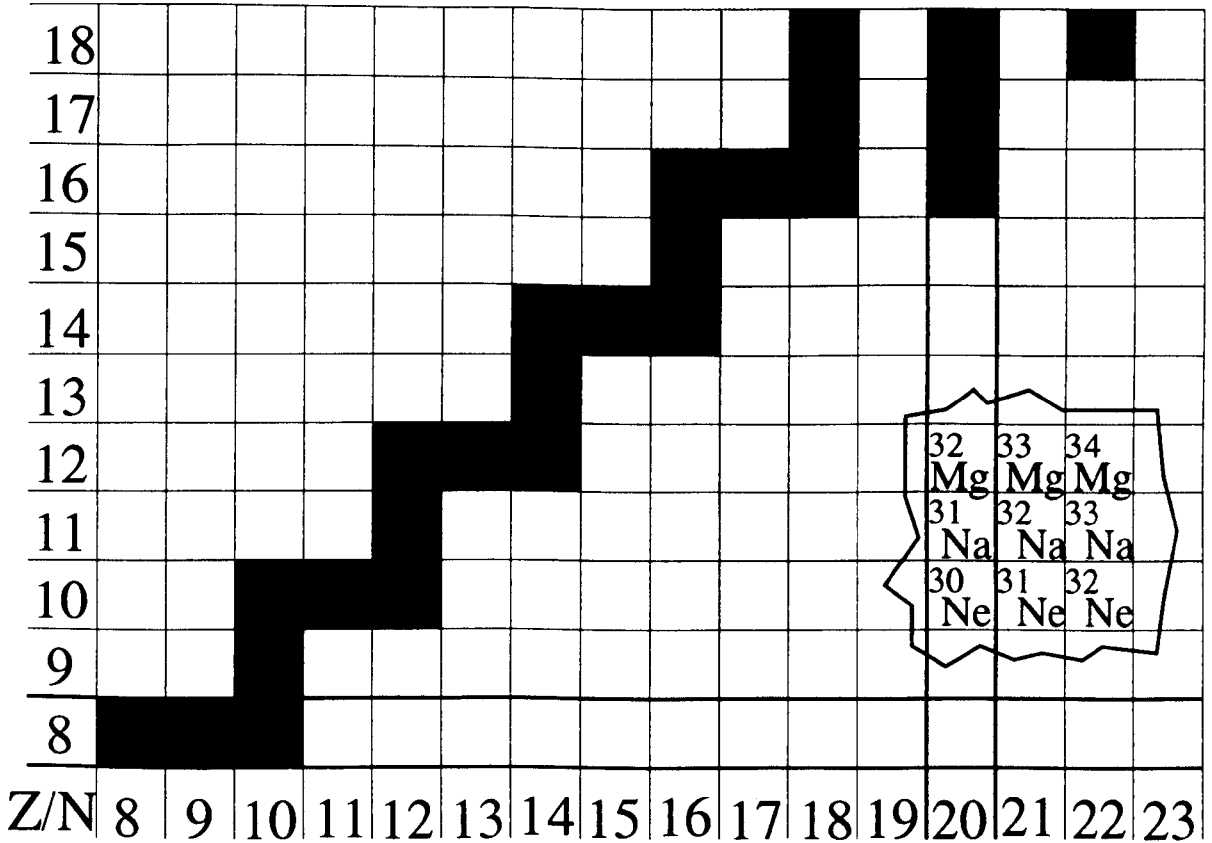
Figure 1.4: Partial periodic table high-lighting the "island of inversion" centred on ^{32}Na. The magic numbers $Z = 8$ and $N = 20$ are emphasised with thick lines. Stable nuclei are shown by filled squares.

intruder states from the $1\nu f_{7/2}$ orbital level led to the correct prediction of the spin of the ^{31}Na ground state. Poves and Retamosa [Pove 87] additionally included the $2\nu p_{3/2}$ orbit and this led to the reproduction of the experimental results and binding energies. For ^{31}Na,

the ground state configuration was found to be dominated by a 90 % contribution by two neutrons from the *fp*-shell.

A large quadrupole deformation is associated with a large B(E2) value and a low 2^+ energy. The much lower measured 2^+ excitation energy of ^{32}Mg (0.885 MeV), compared with other N = 20 isotones (figure 1.5) has led to the prediction of a B(E2) value of 450 e^2fm^4 for the ^{32}Mg ground state [Fuku 92] with a large admixture of the *pf*-orbits and to a well deformed nucleus with a β_2 deformation of 0.51. This B(E2) value is consistent with that
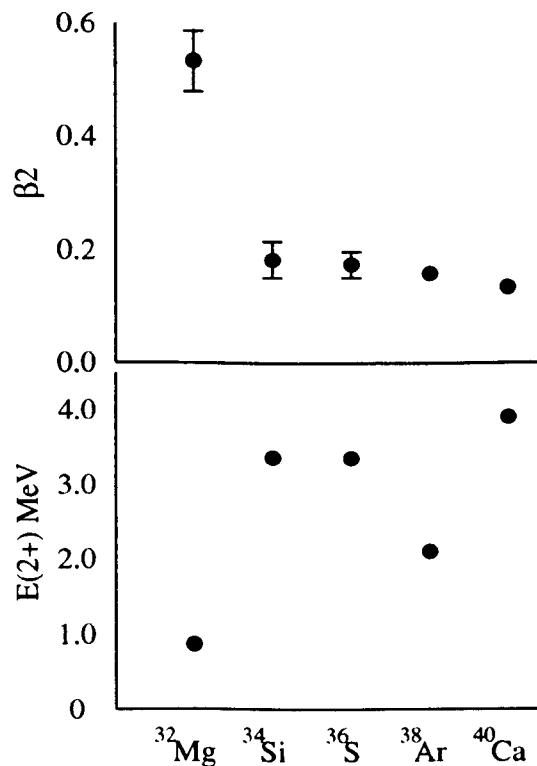
Figure 1.5: The deformation parameter β_2 extracted from the measured B(E2↑) values in the N = 20 nuclei [Endt 90]. The 2_1^+ states of ^{34}Si, ^{36}S, ^{38}Ar and ^{40}Ca appear to have similar non-collective structures despite the considerable variation in excitation energy [Ibbo 98].

subsequently measured by Motobayashi *et al.* of 454 ± 78 e^2fm^4 [Moto 95] by Coulomb excitation of a ^{32}Mg beam at 49.2 MeV/A on a ^{208}Pb target.

The deformations caused by the neutron orbital inversions increases the binding of the Z $\simeq$ 10-12, N = 20 nuclei but there is conflict as to the origin of these excitations. Storm *et al.* [Stor 83] emphasised the effect the large neutron excess has on the effective single-

particle energies. They found that for Z = 8 or 9. the effective $\nu f_{7/2}$ energy actually drops below the $\nu d_{3/2}$ energy at $N = 20$. whereas Warburton et $al.$ [Warb 90] do not see such a drastic effect but rather a diminishing of the $\nu f_{7/2}$-$\nu d_{3/2}$ energy gap with neutron excess for Z = 8 - 12. They state that the major factor would appear to be the very strong effect the T = 0 p-n interaction has on the region in question. De-Shalit and Goldhaber [Shal 53] and later Federman and Pittel [Fede 79] pointed out the crucial role this interaction has on forming deformation throughout the periodic table. The interaction is proportional to the overlap between neutron and proton orbitals and thus is strong when $n_p \simeq n_n$ and $l_p \simeq l_n$ as is certainly the case for the interaction of the $\pi d_{5/2}$ orbit with the $\nu d_{3/2}$ orbitals.

The island of inversion is believed to be centred on the eight nuclei around ^{32}Na shown in figure 1.4 from mass measurements and shell model calculations although what is not as well known is if the island is formed suddenly [Camp 75] or if there is in fact a gradual variation in change of the domination of the ground state from sd-shell to fp-shell configurations. Poves and Retamosa [Pove 94] predicted that the intruders which cause the deformation become dominant in the ground states of the isotopes of Ne, Na and Mg for $N > 19$. The previously mentioned cases of ^{31}Na and ^{32}Mg are significant as they show evidence of β-decay from an intruder to a 'normal' configuration as should be the case for ^{30}Ne if there is a sudden change in configuration.

1.4   Measurements of Neutron Rich Nuclei.

The energy spectra of excited levels for certain nuclei reasonably close to stability have been measured using transfer reactions [Wilc 73, Nann 80, Fifi 85, Wood 85, Orr 89], but rapidly diminishing cross sections as one moves to more neutron rich nuclei limits the nuclei which can be studied using this approach. Beta-delayed γ-ray spectroscopy can probe a different subset of energy levels and has a greater precision. In principle these decay measurements can be applied to nuclei right up to the drip line, although this requires that the nuclei of interest are cleanly and efficiently separated and there is a high detection efficiency for the radiation that these nuclei emit.

Chapter 2

Radioactive Decay.

2.1 Beta-Decay.

The β-decay process causes the atomic number of the nucleus to change while the total nucleon mass number remains constant. The possible β-decay processes are, as shown in figure 2.1: β^-, the emission of an electron and an anti-neutrino which is from the conversion of a neutron into a proton in a nucleus; β^+, the emission of a positron and a neutrino which is from the conversion of a proton into a neutron in a nucleus or EC, the capture of an atomic electron with the emission of an anti-neutrino and converts a proton into a neutron in a nucleus. Therefore, β-decay is a convenient process for an unstable nucleus to transform
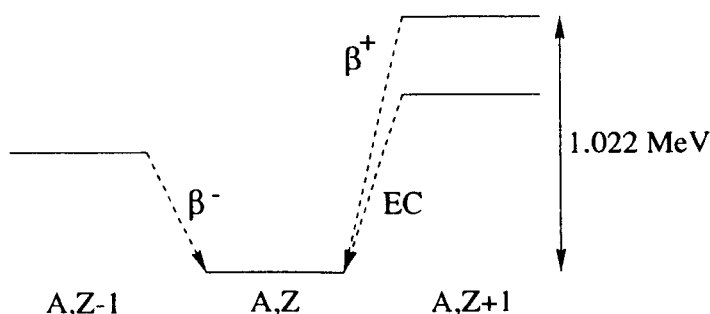
Figure 2.1: Schematic showing the three possible β-decay processes.

into a more energetically stable isobar, figure 2.2.
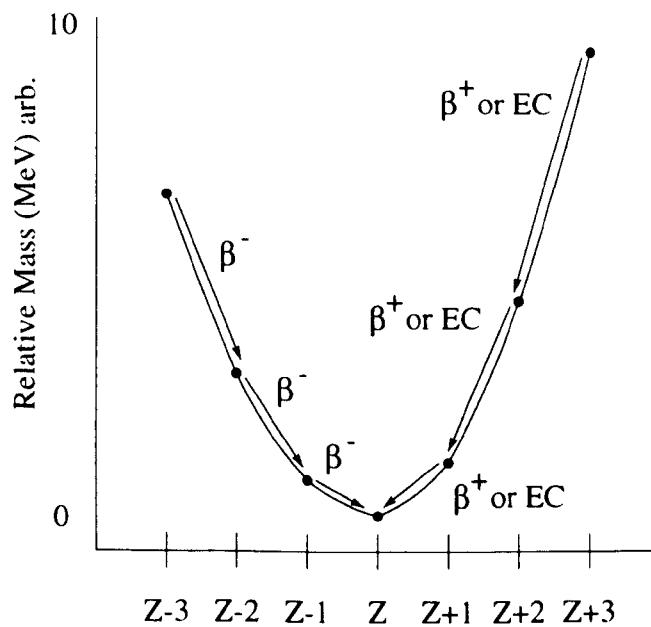
Figure 2.2: A schematic of the relative atomic masses of an isobar chain and their possible β-decay processes as a function of Z.

2.1.1 Energetics.

For a nucleus to undergo β-decay the conservation of total energy requires the mass of the initial nucleus to be greater than the final one. The mass of a neutral atom consisting of Z protons and N neutrons is given by

$$M(Z,N) = Zm_H + Nm_n - B(N,Z), \qquad (2.1)$$

The difference in the masses of the initial and the final nuclei is called the Q-value (Q_0).

The energy spectrum of β-particles associated with a given β-decay process is continuous up to the Q-value of the reaction. This was a surprising discovery as the levels in the nucleus are known to have discrete energies. Pauli offered an explanation in 1933 [Paul 33], when he postulated that a second particle was emitted in the decay process. This particle was named the neutrino by Fermi. There are two types of electron neutrinos, the anti-neutrino associated with β^--decay and the neutrino with β^+-decay.

For β^--decay in a nucleus,

$$M(Z,N) \rightarrow M(Z+1,N-1) + e^- + \bar{\nu}_e, \qquad (2.2)$$

where $M(Z + 1, N - 1)$ is the mass of the daughter nucleus. Q_0 is therefore given by

$$Q_0 = Q_{\beta^-} = M(Z, N) - M(Z + 1, N - 1),$$ (2.3)

This energy released is shared between the kinetic energy of the electron and the anti-neutrino (neglecting recoil of the daughter), i.e.

$$Q_{\beta^-} = T_e + T_{\bar{\nu}_e}.$$ (2.4)

2.1.2 Fermi and Gamow-Teller Interactions.

The theoretical description of β-decay was first proposed by Fermi in 1934 [Ferm 34], although it was not complete as subsequent work showed that it did not take into account parity violation [Lee 56, Wu 57].

The radiation emitted by a nucleus undergoing β-decay can be mathematically described in terms of transitions characterised by their *forbiddeness*. These terms are the constituent components of the field that arise from a series expansion, each additional term of which corresponds to an increased angular momentum change. A finite first term of the series, which is possible if the parent and daughter single particle wave functions are identical, is called an *allowed* transition, there is no resulting change in the orbital angular momentum or the spin of the nuclear system. A special case is that of $0^+ \rightarrow 0^+$ which is called *superallowed*. If the first term is zero (as can arise if the initial and final nuclear states are of opposite parity) but the second term is finite, then the transition is still possible but this time it is called *first forbidden.*

The above transitions were described successfully by Fermi, although some β-decays were observed with comparable transition rates to Fermi allowed with no change in parity but with a change in total angular momentum of 1. Gamow-Teller [Gamt 36] proposed the addition of a spin operator which causes a change in the spin part of the nuclear wave function of 0 or 1 but no change in the orbital momentum component of the wave function. For a Gamow-Teller allowed transition $\Delta J = 0$ or 1 with no change in parity, but $0^+ \rightarrow 0^+$ is not allowed. In a Fermi allowed transition a neutron can change into a proton with no effect on the decaying nucleon's (and hence the total nuclear) wave functions. The transition is therefore between analogue states and this leads towards an isospin selection rule for Fermi allowed transitions, of $\Delta T = 0$. In a Gamow-Teller transition, however, the nucleon's wave

function can alter and the isospin change is due to the single nucleon change. Since a nucleon has isospin 1/2, the Gamow-Teller allowed isospin selection rule is $\Delta T = 0$ or 1.

2.1.3 Angular Momentum and Parity Selection Rules.

Selection rules can be obtained from the series expansion of the β-decay radiation emitted which arise from the combination of the wave function of the initial and final states. Table 2.1 shows a list of the first few possible β-decay transitions. Transitions which have a

Transition	Angular Momentum Change	Parity Change
Superallowed	0	no
Allowed	0,1	no
First Forbidden	0,1,2	yes
Second Forbidden	0,1,2,3	no

Table 2.1: Table of possible β-decay transitions and possible partity changes.

change in parity, or for which the change in the orbital angular momentum component is greater than 1 are called *forbidden transitions*. This arises due to the large reduction in transition rates compared to allowed transitions and consequently the initial states have longer half-lives.

2.1.4 Beta-decay Half-Life and ft values.

Fermi's golden rule describes how the transition rate of a decay is related to the density of final states and the matrix element of the transition. From considerations of both these components [Kran 88], the comparative half-life ft value can be derived as being

$$ft_{1/2} = 0.693 \frac{2\pi^3\hbar^7}{g^2 m_e^5 c^4 |m_{fi}|^2}, \tag{2.5}$$

where g is the β-decay constant, m_e is the mass of an electron and $|m_{fi}|$ is the matrix element of the transition. The quantity f is related to the Z of the daughter and to the Q-value. Therefore, differences in ft values must be due to differences in the nuclear matrix element and hence due to differences in the nuclear wave function. The ft value increases

with the extent to which the transition is forbidden and due to the enormous range of half-life values in β-decay ft values are often quoted as the $\log_{10} ft$ (t in seconds). A summary of $\log_{10} ft$ values and their corresponding degree of forbiddeness are shown in table 2.2 (taken from [Kran 88]).

Transition Type	$\log_{10} ft$
Superallowed	2.9 - 3.7
Allowed	4.4 - 6.0
First Forbidden	6 - 10
Second Forbidden	10 - 13
Third Forbidden	> 15

Table 2.2: Comparison of the $\log ft$ values and their corresponding transition type.

2.1.5 Beta-delayed Gamma-ray Emission.

When a nucleus undergoes β-decay the daughter nucleus is not necessarily populated in its ground state. Excited nuclear states in the daughter system can be populated directly and these states can decay via γ-ray emission as illustrated in figure 2.3. Beta-delayed γ-ray emission is a useful method for placing limits on the spins and parities of these populated states if the $\log_{10} ft$ values can be deduced. This requires knowledge of the Q_0 energy (minus the excitation energy of the populated excited nuclear state), half-life, as well as the ground state spin and parity of the parent nucleus.

2.1.6 Beta-delayed Neutron Emission.

Gamma-rays are not the only form of radiation that can be emitted from excited nuclear states following β-decay. Occasionally the states are unstable against the emission of one or more nucleons. The nucleon emission itself occurs rapidly and thus overall the nucleon emission occurs with a half-life characteristic of the β-decay.

The emission of a single neutron following β-decay to an excited state is possible when the Q-value is larger than the one-neutron separation energy S_n, i.e. $Q_\beta - S_n > 0$. Likewise two-neutron emission can occur when the condition $Q_\beta - S_{2n} > 0$ is satisfied. For nuclei
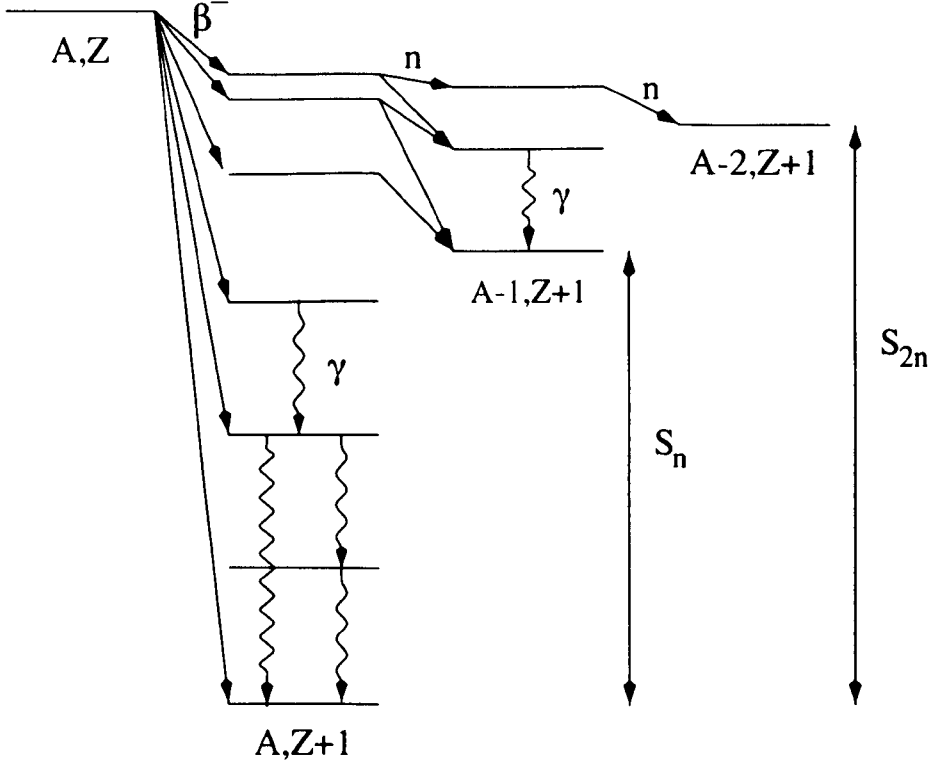
Figure 2.3: Schematic showing β-delayed γ-ray and β-delayed neutron emission.

close to stability, $S_n \approx$ 6-8 MeV and thus it is extremely unlikely that these conditions will be fulfilled. However, as one moves towards the neutron drip line, S_n and S_{2n} decrease and β-delayed neutron emission becomes a possibility (see figure 2.3). Some nuclei in which this behaviour has been observed are $^{11}_{3}\text{Li}_8$ [Azum 79], $^{30}_{11}\text{Na}_{19}$ [Guil 84], $^{15}_{5}\text{B}^{10}$ [Dufo 84] and $^{19}_{6}\text{C}_{13}$ [Dufo 88]. A measure of the probability that a nucleus will decay via the β-n channel is the neutron emission probability, P_n, which is the absolute branching ratio and is defined as the average number of neutrons emitted per β-decay.

$$P_n = \sum_{i=0}^{\infty} i P_{in} \tag{2.6}$$

with

$$\sum_{i=0}^{\infty} P_{in} = 1. \tag{2.7}$$

Chapter 3

Experimental Details

3.1 Reaction Processes.

The production of neutron-rich nuclei near the drip line has been difficult until the recent availability of increased beam energies which have allowed spallation and fragmentation reactions to be performed. The impact parameter, b, (see figure 3.1), centre of mass energy and the nature of the target and projectile determine whether a certain interaction occurs. For impact parameters larger than the grazing parameter the interaction between the target and projectile nuclei is negligible and there is no transfer of nucleons between the two heavy ions. The onset of the nuclear interaction at grazing collisions results in processes such as inelastic scattering and the transfer of a few nucleons between the target and projectile. Significant overlap of the nuclear matter results in reactions such as deep-inelastic and deeply penetrating collisions. Previously deep-inelastic collisions and transfer reactions were used to study the properties of light neutron-rich nuclei although these types of reactions are hampered as it is not always possible to study nuclei at the neutron drip line in this way. Deep-inelastic processes dominate in very heavy-ion collisions with energies of a few MeV/A above the Coulomb barrier. One of the primary reasons why deep-inelastic collisions are useful in producing light neutron-rich nuclei [Artu 70c, Forn 97] is the equilibration of mass and charge. This is because the average neutron-to-proton ratio of both beam and target fragments develops towards that of the intermediate complex [Frei 84]. Angular momentum is transferred from relative orbital motion to the intrinsic spin of the two primary fragments and the amount of transferred angular momentum can be large, allowing the study of the

16

electromagnetic transitions between excited states.
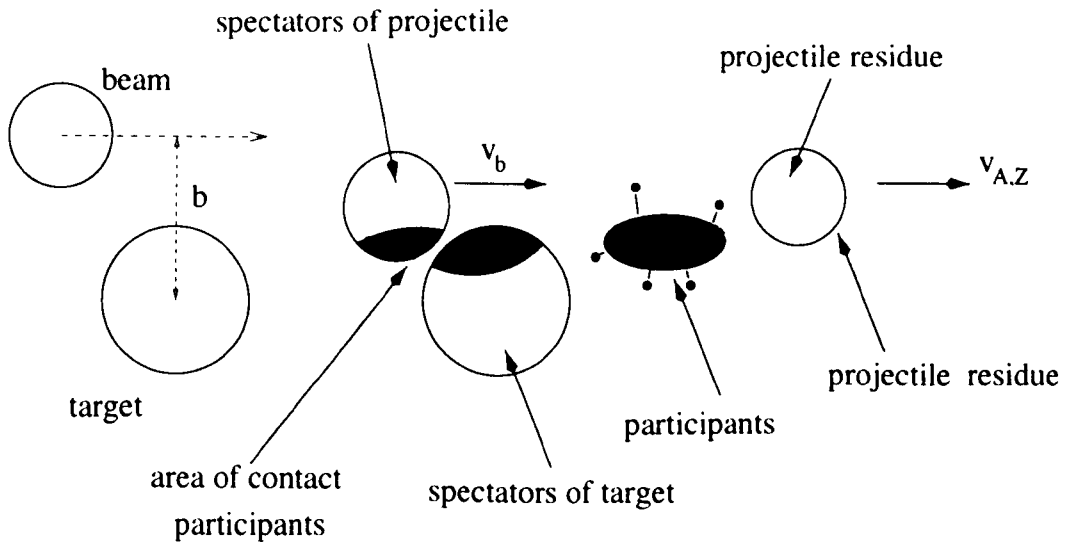
Figure 3.1: Schematic showing the fragmentation process.

At similar energies inelastic scattering and transfer reactions can proceed as direct reactions. Transfer reactions are particularly useful in the study of low-lying shell model excited states and several such states can be populated in a given reaction. The states are identified by the energies of the outgoing reaction products. This shows a significant difference from those studies involving deep-inelastic and fragmentation reactions. In transfer work, the energies of excited states are generally measured directly although typically with a much poorer energy resolution than for γ ray studies. Fragmentation reactions offer the experimentalist a reaction mechanism that can produce the light neutron rich nuclei at the drip line so that excited states populated in their β-decays can be studied.

3.1.1 Fragmentation.

The high velocities used in fragmentation (typically $v/c \approx 20 - 30$ %) imply that the beam nuclei spend a very short amount of time in the vicinity of the target nuclei. The quantity that governs fragmentation, apart from the v/c value, is the impact parameter. As the value of b decreases the likelihood of direct nuclear reactions increases until the beam and target nuclei can interact directly, see figure 3.1.

Momentum distributions [Grei 75] suggest that all the isotopes produced in fragmen-

tation reactions are produced by peripheral collisions between the projectile and target nuclei, since the most probable value of the momenta of the fragments produced practically coincides with that of the projectile. Peripheral collisions also imply that relatively low excitation energies are imparted to the fragments. Due to the very short time of contact (approximately 10^{-23} s for a nucleus of radius 5 fm) a compound nucleus type reaction is not possible.

The point of contact between the two nuclei due to the nuclear surfaces overlapping can become very hot and a transfer of nucleons between the two partners becomes possible via quasi elastic nucleon exchange. This is why it also sometimes possible in fragmentation reactions to observe nuclei with a larger number of protons or neutrons than the beam. For example, Regan et al. [Rega 97], using a ^{92}Mo beam at 60 MeV/A on natural nickel targets observed nuclei with Z = 43 (Tc), 44 (Ru) whilst the beam used had a proton number of 42. In the present experiment it was possible to observe nuclei with neutron numbers greater than that of the beam. However, this is a very weak process and for each nucleon transferred there is a drop in yield by approximately a factor of ten. This loss can be attributed to the large differences between the target and projectile nucleon momenta [Volk 89]. The degree to which the nuclear surfaces overlap due to a projectile fragmentation reaction grows as the number of nucleons transferred increases [Harv 85]. The more the nuclear surfaces overlap though, the greater the excitation energies become in the projectile residues and hence the lower the survival possibilities of the exotic nuclei.

More evidence for nucleonic exchange has been found in the shift in the isotopic distributions with the N/Z ratio of the target material at intermediate energies. Natural nickel (N/Z = 1.1) has been found [Henc 94, Blan 95, Ryka 95] to be useful in the production of proton rich fragments, whereas neutron-rich targets such as tantalum and beryllium (with N/Z ratios of 1.5 and 1.3 respectively) have been found to favour the production of neutron rich nuclei [Gelb 78, Dufo 84, Tara 98, Guil 85]. A projectile having a large neutron excess would, therefore, be expected to fragment into a larger number of neutron-rich isotopes [Borr 83, Guil 90, Dufo 84] as well and the yield of neutron-rich sodium isotopes produced by bombarding a beryllium target with a 215 MeV/A beam of $^{48}_{20}$Ca$_{28}$ (N/Z = 1.4) turned out to be an order of magnitude higher than that observed when a similar target was bombarded with a 205 MeV/A beam of $^{40}_{18}$Ar$_{22}$ (N/Z = 1.2) [West 79].

After the brief interaction the direction of travel of the beam fragments is essentially unaltered due to their large momentum except for the possibility that nucleons have been stripped off the nuclei by the target. It is possible to have both beam like fragments and target like fragments produced in the reaction, therefore the products formed in a fragmentation reaction have a wide dispersion over mass and charge. The high velocities lead also to the loss of all electrons by the fragments during their interaction with the target. This is a useful property of this type of interaction when attempting to separate the nuclei (see section 3.5).

The first experiments involving bombarding targets with high velocity beams showed that the production of isotopes far from the stability line was possible [Grei 75, Lind 75]. Fragmentation type reactions were first used to search for neutron rich nuclei in the late 1970s [Viyo 79, Symo 79], by fragmenting a ^{40}Ar beam at 213 MeV/A on a carbon target. This experiment gave evidence for the existence of ^{28}Ne and ^{35}Al for the first time. This process has subsequently been used for the identification of new neutron-rich isotopes of elements in the region $5 \leq Z \leq 27$ at 40 - 100 MeV/A intermediate energies at GANIL [Lang 85, Poug 86, Guil 85, Guil 89, Guil 90, Prav 91].

3.2 Interaction of Radiation with Matter.

3.2.1 Charged Particles.

Heavy, charged particles will essentially propagate without deflection through a detector with the main contribution to the slowing down process being the long range Coulomb force from electrons in the material as the positive charge contribution due to the target nuclei are shielded by their orbiting electrons. The electrons feel an attractive Coulomb force as the particle passes and, depending on the proximity of the interaction, the force can either raise the electron to a higher orbital shell in the atom (atomic excitation) or completely remove the electron from the atom (ionisation). The maximum energy that can be transferred to the electron is

$$\frac{4Tm_e}{M},$$

(3.1)

where T and M are the kinetic energy and mass of the charged particle respectively. This is a very small fraction of the total kinetic energy and many such interactions are necessary

as the particle slows down. This small energy loss does not cause any significant deviation from the trajectory of the particle and hence an approximately straight line path is followed. see figure 3.2. At any given time the particle is interacting with many electrons so the net effect is to decrease its velocity continuously while maintaining the initial trajectory.

3.2.2 Electrons.

Electrons induce ionisation in the detector in a similar method to heavy charged particles, but the situation is slightly more complex due to the inclusion of radiative processes (Bremsstrahlung) at energies above a few MeV. Since the two interacting particles have the same masses large energy losses are possible as well as large deviations in the tracks of the electrons, see figure 3.2. The range for electrons in material is not as well defined as it is for
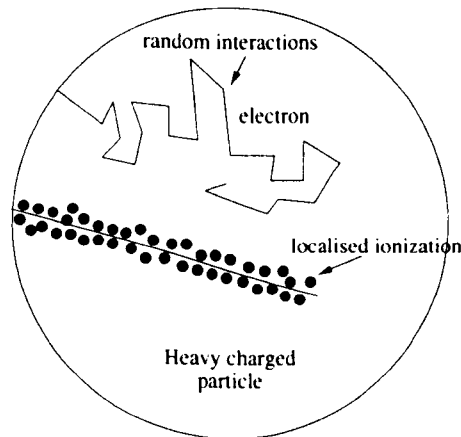
Figure 3.2: A schematic of the difference between the interactions of heavy charged particles and electrons with matter.

heavy charge particles as the actual path length is much greater than its apparent range, as a result of the large deviations in the path that the electron can take.

3.2.3 Photons.

As shown schematically in figure 3.3 photons can interact with matter in three basic processes, these are the

a) Photoelectric Effect

b) Compton Scattering

c) Pair Production

The Photoelectric Effect: This is the predominant form of interaction for low energy ($\leq$ 200 keV) γ rays and for X-rays and can only take place with an atomically bound electron. An incoming γ ray undergoes an interaction with an atomic electron and is completely absorbed. A photoelectron can be emitted in place of the γ ray from one of the bound orbital shells of the atom. The most likely source of the photoelectrons is the most tightly bound, or K-shell, electron of the atom. The kinetic energy of the photoelectron is then given by the relationship:

$$E_{e^-} = h\nu - E_b \tag{3.2}$$

where E_b represents the binding energy of the photoelectron in its original shell.

The interaction therefore creates an ionised absorber atom with a vacancy in one of its bound shells. This vacancy is quickly filled through the capture of a free electron from the medium and/or from the rearrangement of electrons from other shells of the atom emitting an X-ray.
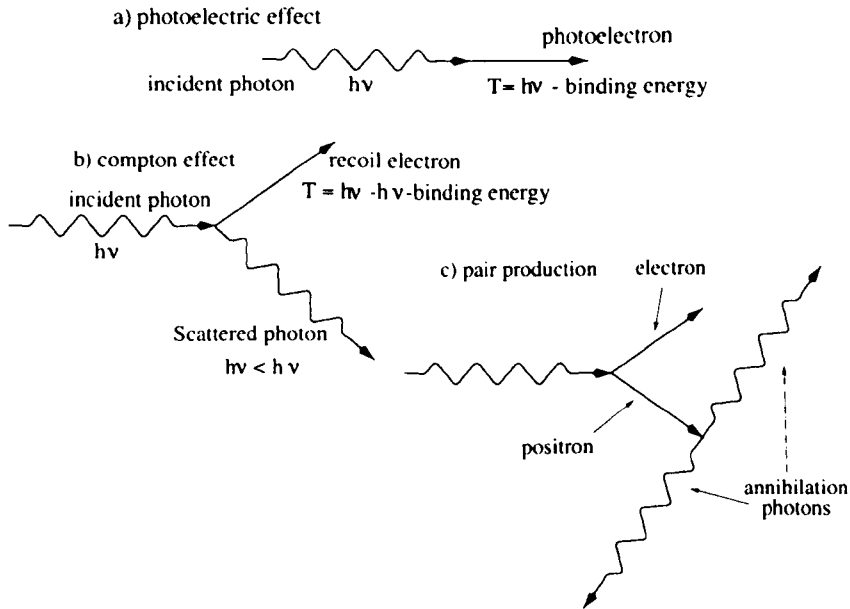
Figure 3.3: The three basic interaction processes of γ rays with matter. The photoelectric effect, Compton scattering and pair production.

The process is enhanced for materials with high atomic numbers, and the probability of

photoelectric absorption per atom over all ranges of E_γ and Z is roughly given as

$$\sigma_{p.e.} \simeq constant \times \frac{Z^{3\to5}}{E_\gamma^{3.5}} \tag{3.3}$$

where the exponent of the numerator varies over the γ ray region of interest [Knol 89].

Compton Scattering: This interaction takes place between a γ ray and a free or nearly free electron. The incoming γ ray interacts with the electron and is deflected through an angle θ with respect to its original direction. The electron, which is thought to be initially at rest, gains kinetic energy from the interaction and is known as the recoil electron. From energy and momentum conservation an expression for the residual energy and scattering angle for the γ ray can be derived [Kran 88]:

$$h\nu' = \frac{h\nu}{1 + \frac{h\nu}{m_e c^2}(1 - cos\theta)}, \tag{3.4}$$

$h\nu$ and $h\nu'$ are the initial and final γ-ray energies; $m_e c^2$ is the rest mass of an electron. Any value of θ is possible up to a maximum of $\theta = \pi$ which represents the angle for the largest energy transfer to the recoil electron, see figure 3.3. The probability of Compton scattering per atom of the absorber material depends on the number of electrons available as scattering targets and increases linearly with Z [Knol 89].

Pair Production: An electron-positron pair is created by the photon. Since the creation of this pair requires $2m_e c^2$ (= 1.02 MeV) pair production is energetically forbidden for photons below this energy. Pair production is the only one of the three major processes whose cross-section increases with increasing energy, and it becomes the dominant absorption mechanism above 10 MeV. No simple expression exists for the probability of pair production per nucleus but its magnitude varies approximately as Z^2 [Knol 89].

The electron-positron pair, which can only be produced in the presence of the Coulomb field of a nucleus, share the excess γ-ray energy over 1.022 MeV, as kinetic energy. Eventually the positron slows down in the medium and annihilates with an atomic electron and the 1.022 MeV rest mass energy of the pair reappears as a pair of 511 keV γ rays, see figure 3.3.

3.3 Detector Design.

3.3.1 Introduction.

The purpose of detecting nuclear radiation is to inspect the properties of the nucleus from which the radiation was emitted. From these measurements it may be possible to determine aspects such as the energy and feeding lifetimes of the excited levels. Also measurable are other properties concerning the ground state decay of the nucleus such as its half-life and mode of radioactive decay. In order to obtain a full picture of the properties of the ground and excited states of a nucleus it is necessary to have a wide range of different detectors which are sensitive to the different types of radiation emitted.

3.3.2 Semiconductor Devices.

The radiation emitted by nuclei can vary in type and energy; the energy ranges can differ from a few keV to a few MeV for γ- and β-radiation and up to many hundreds of MeV for α-radiation and other charged particles. Also the different sorts of radiation interact in specific ways. For example, the absorption of a charged particle creates ionisation all along its path while a photon interacts at random points in the detector to produce secondary electrons.

Semiconductor detectors are solid state detectors which generate an electric current when ionising radiation passes through. These detectors are by far the most useful for detecting radiation due to their versatility since their nature and size can be matched to the absorption characteristics of the radiation to be measured. One desirable requirement for semiconductor detectors is that when a photon or a particle is detected the number of carriers produced in the subsequent ionisation should be linearly proportional to the energy absorbed. The best detectors will require a small amount of incident energy to produce an electron-hole pair, which means that on average a very large number of carriers will be produced for each incident radiation detected. These large numbers produced help to reduce statistical fluctuations and to improve the resolution of the detector.

Another requirement arising from the large amount of statistics required to do a complete analysis of a nuclear reaction is that the detectors also need to be highly efficient. The carriers must be able to move through the material in response to an externally applied

electric field unhindered so that the total charge output can be detected to keep the energy absorbed proportional to the total charge output. High electric fields need to be applied, typical values being 1000 - 3000 V for germanium detectors and $\approx$ 100 V for silicon detectors, to ensure fast and efficient charge collection. The detectors must also have negligible leakage current as this can cause noise in the detector worsening the resolution and hindering the detection of low energy radiation. Of the available semiconductor materials, silicon is the predominant material used primarily for charged particle spectroscopy while high purity germanium crystals are more widely used for the detection of γ rays with high energy resolution.

Germanium and silicon, both valence-four elements, bind to their respective neighbouring atoms with all four electrons forming covalent bonds. Thus, all the electrons are used in covalent bonds and at a temperature of absolute zero the band structure shows a full valence band and an empty conduction band. The difference between an insulating material and semiconductor material is the width of the band-gap between these two energy bands. For insulators, the band-gap is large (many eV) whereas for semiconductors the band gap is smaller, making it easier to excite an electron from the valence to the conduction band. Silicon has an energy gap of 1.115 eV compared with 0.665 eV for germanium at 300 K. It is possible, therefore, to thermally excite an electron from the valence band to the conduction band, this leaving holes in the valence band. Artificially altering the number of charge carriers in a semiconductor by adding dopants can specify what the majority charge of the carriers will be. Adding atoms with one less valence electron leads to *p-type*, adding atoms with one more valence electron produces *n-type* material.

When n-type and p-type material are brought together, initially there is a flux of positive carriers to the n-type material and a flux of negative carriers in the opposite direction. This continues until the point when the electrostatic repulsion builds up so that no more charges can migrate. At this point a *depletion region* is created. Radiation can enter this depletion region and create electron-hole pairs which are swept in opposite directions, and the total number of electrons collected can form an electronic pulse whose amplitude is proportional to the energy of the radiation.

In practice a large reverse bias is applied across these detectors which has two effects; firstly it increases the magnitude of the electric field in the depletion region making charge

collection more efficient and secondly it increases the dimensions of the depletion region, thereby increasing the effective volume and efficiency of the detector.

The signal from the detector is initially passed through a preamplifier whose primary job is to convert the charge pulse from the detector to a voltage pulse for the rest of the electronics. The next module is usually a shaping amplifier which provides the voltage gain to bring the millivolt preamp pulse to the range of a few volts where it can be conveniently processed. The amplifier must be linear, so the proportionality of radiation energy to pulse height can be preserved.

3.3.3 Gamma-ray Detectors.

The study of the γ radiation emitted by radioactive sources is one of the primary means of learning about the structure of excited nuclear states. It is necessary, therefore, to be able to measure accurately the energy of these γ rays as well as the intensities. Germanium detectors enable high energy resolution, typically of the order of 2 keV at 1.33 MeV [Beau 92].

To minimize thermal noise, which is generated by thermally exciting electrons into the conduction band it is necessary to keep the crystals at liquid nitrogen temperature. This reduces the probability of thermally exciting electrons across the band gap, as given by equation 3.5:

$$p(T) = CT^{3/2} exp\left(-\frac{E_g}{2KT}\right), \qquad (3.5)$$

where C is a proportionality constant characteristic of the material, T is the absolute temperature, E_g is the band gap energy and K is the Boltzmann constant. The probability is critically dependent on the ratio of the band gap energy to the absolute temperature [Knol 89, Gilm 95].

When a photon strikes a crystal of semiconductor material the three basic processes described earlier (see section 3.2.3) are possible . For photons whose energy is lower than the threshold energy for pair production only the other two types of interaction are possible. The incident photons can therefore transfer all (in the case of the photoelectric effect) or part (Compton scattering) of their energy to electrons in the detector material creating electron-hole pairs.

3.3.4 Charged Particle Detectors.

The requirements on detectors and signal processing electronics for use in particle identification systems are generally similar to those imposed on detectors for γ-ray detection. In the case of energy loss (ΔE) detectors, the thicknesses can range from about 1 g/cm^2 to 0.1 mg/cm^2 depending on the types of ions being measured. Thinner detectors are required for low-energy and/or heavy-ion measurements. Thick detectors (up to a practical limit of ≈ 5 mm) require very pure silicon or the compensation of impurities by lithium-drifting.

In studies of relatively rare isotopic species which are accompanied by large numbers of less exotic species, good resolution is required as are small fluctuations in the signals of the particles impinging on the detector. To allow many such energy loss measurements it is possible to use multi-detector identification systems. Such systems [Cern 66, Goul 75] were used for the mass determination of particle-stable neutron-rich isotopes near the neutron drip line. The detector thicknesses are chosen so that the particles of interest pass through the ΔE detectors and implant in the E detector which measures the resultant energy of the fragments. An E_{rej} detector behind the E detector permits rejection of any particles that pass through the E detector. These would normally be light fragments, e.g. p, d, t, etc... or heavier fragments that do not lose all their energy.

The β-particle energy spectra produced from β-decays consist of a continuous energy distribution up to a well defined end point and high resolution spectrometry is not often essential. The electrons emitted following β-decay will not have a definite energy or range. For the majority of β-spectra, the absorption curve happens to have a near-exponential shape, and a simple relationship can be derived:

$$\frac{I}{I_0} = e^{-nt} \tag{3.6}$$

where I_0 is the initial count rate, I the count rate with absorber, t is the absorber thickness and n is the absorption coefficient [Knol 89]. The coefficient n is related to the end-point energy of the β-emitter for a specific material [Balt 77].

3.4 Experimental Detection of Neutrons.

Neutrons, being uncharged, cannot be detected by Coulomb interactions which dominate the energy loss mechanism for charged particles. However, when a neutron does un-

dergo an interaction with a nucleus of the absorbing material. nuclear reactions can occur which produce easily detectable charged particles. The ^{3}He(n,p)t reaction has a Q-value = +0.764 MeV, and has a large cross-section (5330 barns) at low energies, which decreases slowly with increasing energy with $1/\sqrt{E}$ dependence [Knol 89]. It is necessary, therefore, to slow down the neutrons produced for detection and this is achieved by using polyethene. The energy produced in the ^{3}He(n,p)t reaction is shared between the proton and the triton as kinetic energy.

The ^{3}He proportional detectors used in the experiment to be discussed in this thesis are those developed by Leake [Leak 68, Leak 80] and shown schematically in figure 4.3 and summarised in section 4.1.3.

The aim of this thesis is to study the β-delayed γ-rays emitted from the decay of the exotic nuclei produced during the experiment and the study of the β-delayed neutrons emitted was performed by Tarasov [Tara 97b] as a parallel analysis to this work and will not be discussed here. The results though ot the parallel analysis will be shown in this work to show to show the consistent results between the β-delayed γ-ray and the β-delayed neutron studies.

3.5 LISE3.

3.5.1 Introduction.

The LISE3 spectrometer [Dufo 86, Anne 87, Sain 87, Muel 91, Muel 92] (figure 3.4) is a doubly achromatic spectrometer in both angle and position consisting of twenty eight quadrupole and four dipole magnets. The physical separation of the nuclei is achieved through two processes. Firstly magnetic analysis (A/Q sensitivity) in the first dipole and secondly by using differential stopping powers (Z^{-2} sensitivity) enabling almost complete separation in mass and charge to give a selected region of nuclides. The dispersion produced in the first half of the spectrometer is cancelled by the latter part which achieves the double achromatism. As a consequence of this achromatic condition, the overall path length, L, for a nucleus is independent of starting position and angle and to a first approximation $\Delta L/L \approx 10^{-3}$. The total length of LISE3 is 43 m, separated into two distinct sections: the distance from the target to the wedge degraders being 8 m and from the wedge to the
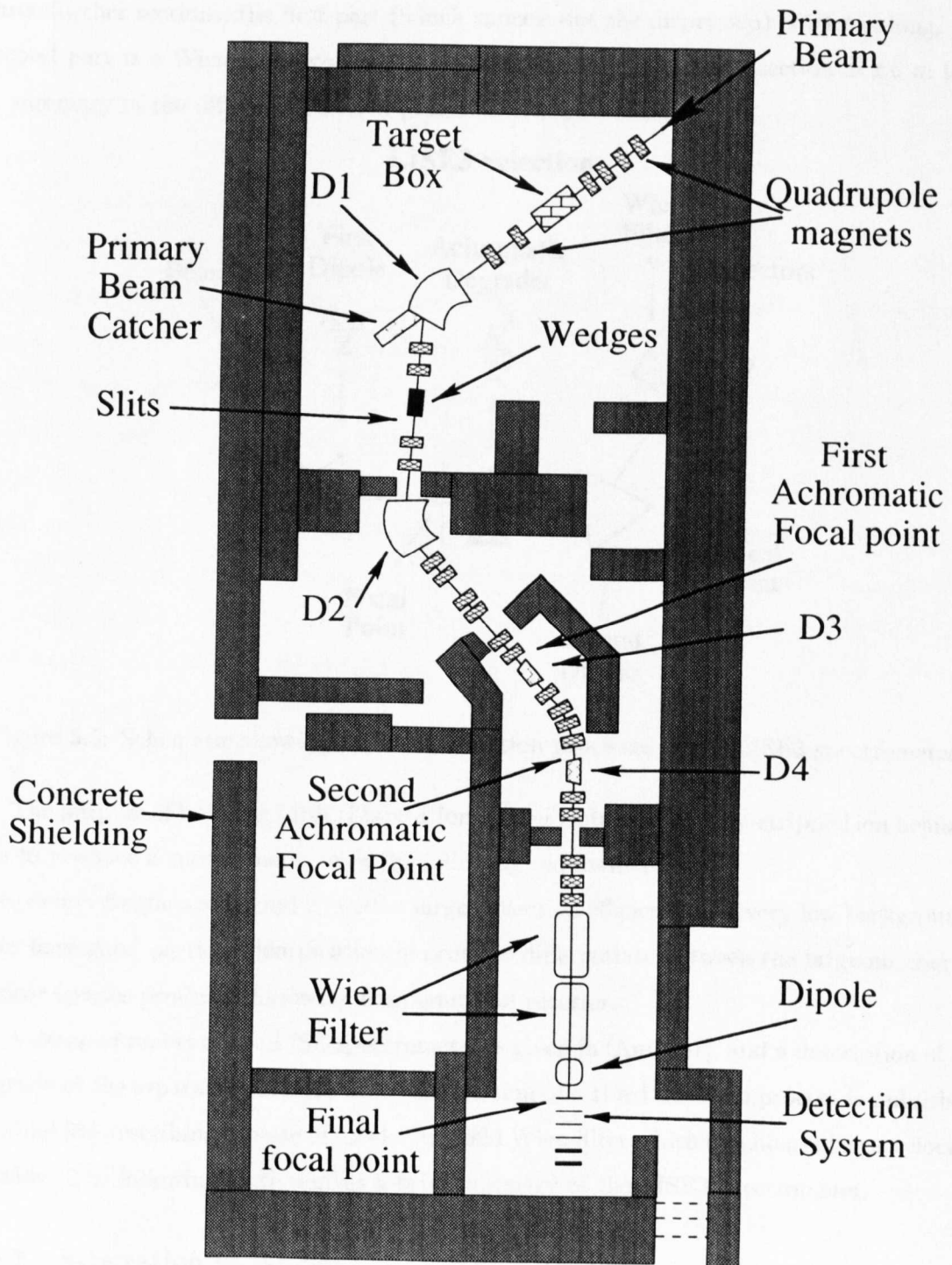
Figure 3.4: Schematic of the LISE3 spectrometer.

final implantation point for the fragments is 35 m. This final section is itself separated into three further sections, the first part (which cancels out the dispersion) is 20.4 m long. The second part is a Wien filter which is 12 m long. The final detection section is 2.6 m long. A summary of the different selection processes is shown in figure 3.5.

LISE3 Selection

Beam — First Dipole $\frac{A \cdot v}{Z}$ — Achromatic Degrader $\frac{A^3}{Z^2}$ — Wien Filter v — Detectors — Focal Point — Focal Point — Second Dipole
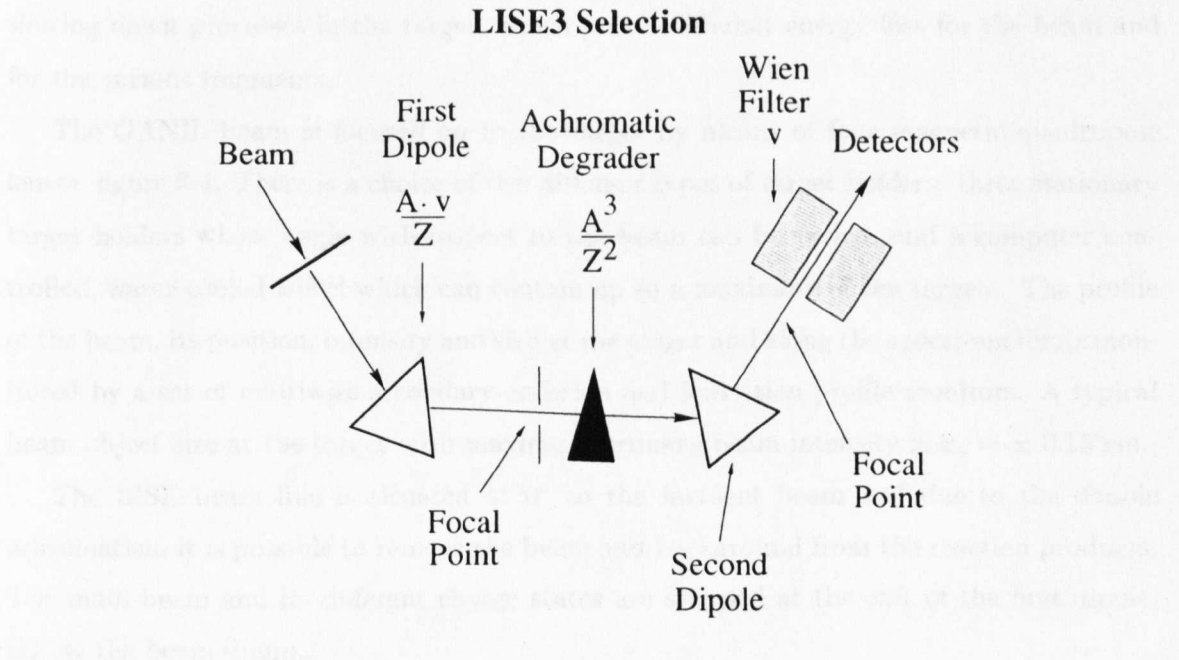
Figure 3.5: Schematic showing the three selection processes of the LISE3 spectrometer.

The purpose of building LISE (Ligne d'Ions Super Epluchés, or fully-stripped ion beams), was to produce a spectrometer with the following requirements:

1) to detect fragments around 0° with a large collection efficiency and very low background;

2) to have good particle identification in order to differentiate between the large number of nuclear species produced following fragmentation reactions.

A detailed report of the LISE spectrometer is given in [Anne 87], and a description of an upgrade of the separator (LISE3) with the addition of a third selection process is published in [Muel 91] describing the use of an electric field Wien filter which can be used as a velocity selector. The following section gives a brief summary of the LISE3 spectrometer.

3.5.2 Separation of Nuclei.

Due to the high bombarding energies (20 to 100 MeV/A) of the heavy-ion beams used, the major part of the reaction cross section goes into fragmentation [Borr 83] and this can

produce a wide isotopic distribution from nuclides close to the beam down to hydrogen. The beam energies selected imply that the velocity of the fragments and secondary products are only slightly less than that of the beam and are emitted in a narrow recoil cone centred about $0°$ [Viyo 79]. The deviations in projectile fragment velocity are mainly due to the slowing down processes in the target, which give a different energy loss for the beam and for the various fragments.

The GANIL beam is focused on to the target by means of four magnetic quadrupole lenses, figure 3.4. There is a choice of two different types of target holders: three stationary target holders whose angle with respect to the beam can be varied, and a computer controlled, water cooled wheel which can contain up to a maximum of ten targets. The profile of the beam, its position, intensity and size at the target and along the spectrometer, is monitored by a set of multiwire secondary-emission and ionisation profile monitors. A typical beam object size at the target with maximum primary beam intensity is $x_o = \pm 0.15$ cm.

The LISE beam line is situated at $0°$ to the incident beam and due to the double achromatism it is possible to remove the beam and background from the reaction products. The main beam and its different charge states are stopped at the exit of the first dipole. D1, at the beam dump.

D1 is a C-framed magnet with a deflection angle of $45°$ and a central trajectory radius of 2 m. The force experienced by a charged particle moving with a velocity v, in a magnetic field of strength B, is, $F_{mag} = q\mathbf{v} \times \mathbf{B}$, using non-relativistic approximations, and equating with the centrifugal force gives

$$B\rho = \frac{mv}{q} = \frac{Av}{Q} \tag{3.7}$$

where the mass of the nucleus is A and ρ is the radius. Hence, the first dipole provides momentum selection, but since the reaction approximately conserves the velocity of the fragments and the ions are fully stripped, this is mainly sensitive to A/Q. The resolution of the initial magnetic analysis is given as $\Delta B\rho/B\rho = 1.3 \times 10^{-3}$ [Anne 87].

Remote controlled variable slits are situated a few cm after D1 at the intermediate dispersive focal plane and these define the momentum acceptance of LISE3. The slits have a maximum separation of ± 4.5 cm corresponding to a maximum momentum acceptance of $\Delta p/p = \pm 2.63$ %.

A series of energy degraders (which are curved pieces of foil mounted on an aluminium

frame) of varying thicknesses can be situated after the slits in the intermediate dispersive plane and select nuclei according to their A^3/Z^2 value due to the different energy losses nuclei experience in the degrader. This selection provides separation inside the subset of nuclei having a constant A/Z, enabling the removal of unwanted nuclei that have the same A/Z values as the nuclei of interest. This has a twofold effect as it removes the majority of the unwanted nuclei and helps prevent pile up of the fragments in the particle detectors, which can be a problem with the high yields of some of the fragments. The characteristic shape of the degraders [Dufo 86, Hoat 86, Schm 87] helps compensate for the energy spread of the nuclei due to the resolution in D1, and to preserve the optical properties of LISE, which gives an energy spread of $E(B\rho_1) \pm \Delta E(\Delta B\rho_1)$,see figure 3.6.
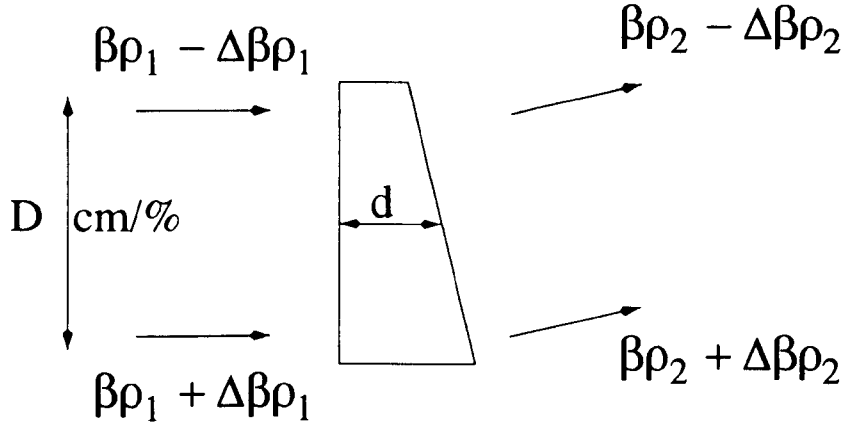
Figure 3.6: The dispersion, D, of ions transmitted through the slits requires a degrader of varying thickness. The fragments with the greater energy have to traverse more of the degrader than those with a lower energy.

It is possible to calculate the energy loss per unit length, or stopping power, of a non-relativistic charged particle of mass A, with Z protons and with energy E and velocity v, moving through matter from the formula derived by Bethe and Block [Livi 37],

$$-\frac{dE}{dx} = \frac{aZc^2}{v^2}ln\left[\frac{bv^2}{c^2 - v^2}\right] \tag{3.8}$$

where a and b are constants, the logarithmic term varies slowly with velocity and can be neglected, and for non-relativistic particles the velocity is just equal to $2E/A$. To a first

approximation equation 3.8 this can be written as

$$\frac{dE}{dx} \propto \frac{AZ^2}{E}.$$ (3.9)

The energy loss is largely due to ionisation of the nuclei that pass within close proximity of the projectile fragments.

Following equation 3.7, from the non-relativistic expression for kinetic energy gives

$$\frac{Q^2}{m} = \frac{2E}{(B\rho)^2}$$ (3.10)

therefore the energy of the ions deflected by the first dipole is proportional to $(B\rho_1)^2$ (where ρ_1 is the trajectory radius of the first dipole) and Q^2/A. As stated above the fragments are fully stripped giving $Q = Z$. Equation 3.10 states that the energy of the particle is proportional to Z^2/A which combined with equation 3.9 gives

$$\frac{dE}{E} \approx K\frac{A^3}{Z^2}t$$ (3.11)

where K is a constant depending on the material used and t is the thickness of the material.

Careful tuning of all the focusing magnets is essential to ensure that the correct nuclei of interest are selected. Although it is not possible to obtain a unique A and Z value due to the high energies involved, it is feasible to obtain a selection for a set of isotones which have a similar magnetic rigidity.

As the intermediate energy degrader reduces the momentum of the reaction products, the value $B\rho_2$ of the second dipole, D2, (which is identical to D1) has to be lowered to compensate for this loss, this helps restore the achromatism for the nuclei of interest.

The original LISE spectrometer ended at the first achromatic focal point and the addition of the Wien Filter has required further achromatic compensation. The dipoles D3 and D4, which have the same magnetic rigidity setting as D2, provide this compensation.

The Wien filter, situated near the end of the beam-line, consists of crossed magnetic and electric fields and acts as a velocity filter. The force on a positively charged particle of charge Ze due to an electric field E, is simply ZeE, and combining with the force experienced due to a magnetic field gives the Lorentz force:

$$F = Z\left(eE + vB\right).$$ (3.12)

For a positively charged particle the Wien filter causes the particle to be deflected in one direction, and causes a negative particle to be deflected in the opposite direction. If a particle feels no net force on passing through the Wien filter then by rearranging equation 3.12 and taking the modulus value one has the condition

$$v = \frac{eE}{B}.$$

(3.13)

Thus only particles with velocity, v, will be allowed to pass through the Wien filter. As the dipole magnets select by Av/Q, the Wien filter places a selection on A/Q.

3.6   Identification of the Fragments.

The fragments are stopped in a silicon stack at the end of LISE3 and are identified unambiguously on an event by event basis. The possible identification processes for the nuclei are (for fully stripped ions):

- energy loss (ΔE) in a silicon detector $\rightarrow$ Z.

- time of flight through the spectrometer $\rightarrow$ A/Q.

- total kinetic energy of fragments $\rightarrow$ A.

- $B\rho$ values $\rightarrow$ Av/Q.

3.6.1   Energy Loss.

At the final focal point for this experiment there was situated a six-element silicon detector telescope. The first element was used as a ΔE detector, the fragments were stopped in the fifth element and the sixth element was used as a veto (see section 4.1.3).

From Bethe's formula [Livi 37] for non-relativistic particles the energy loss can be written as:

$$\frac{dE}{dx} = C_1 \frac{mZ^2}{E} ln C_2 \frac{E}{m}$$

(3.14)

where C_1 and C_2 are constants depending on the material used. The fragments of interest all have approximately the same energy E, and therefore, the energy deposited in the ΔE detector will be proportional to mZ^2 and total separation of different Z-values is possible (see figure 3.7), when dE/dx is plotted for the first element of the silicon-stack.
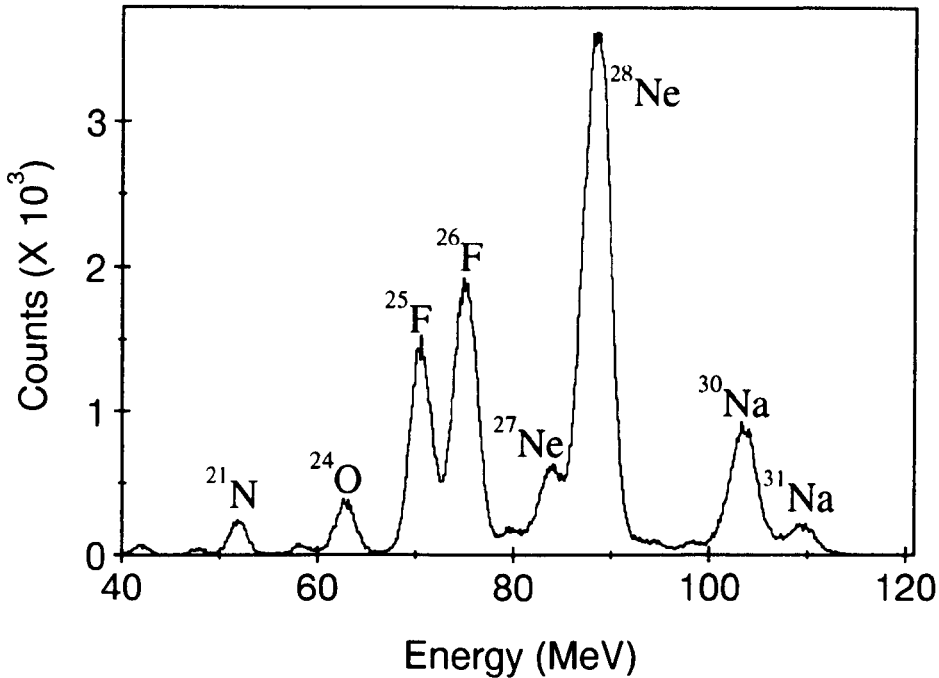
Figure 3.7: Energy Loss Spectrum for the ^{26}F setting.

3.6.2 Time of Flight.

A second identification process is a measurement of the time of flight (TOF) of the fragments through the spectrometer. This is possible as the flight path is constant to a first order approximation for all the nuclei, (see section 3.5.1).

For a TOF measurement the start is taken as the signal from the silicon stack telescope detector in the final focal plane, either element one or element five, and the (delayed) stop signal from the high frequency signal of the primary beam at the target. The start and stop signals are reversed to prevent unnecessary triggering [Muel 88].

The cyclotron emits the nuclei in packets with a width of 1 - 2 ns and a frequency ν, and these beam nuclei all have a velocity v_b. The nuclei produced after the fragmentation have slightly different velocities depending on their A and Z values and for a given fragment $v_{A,Z} < v_b$, due to the energy loss in the target, and $v_{A,Z} \approx v_{A\pm1,Z\pm1}$ for example. Hence fully stripped nuclei with the same A and Z travel down the beam pipe together in bunches.

The distance between the target and final implantation point is known exactly, L, and
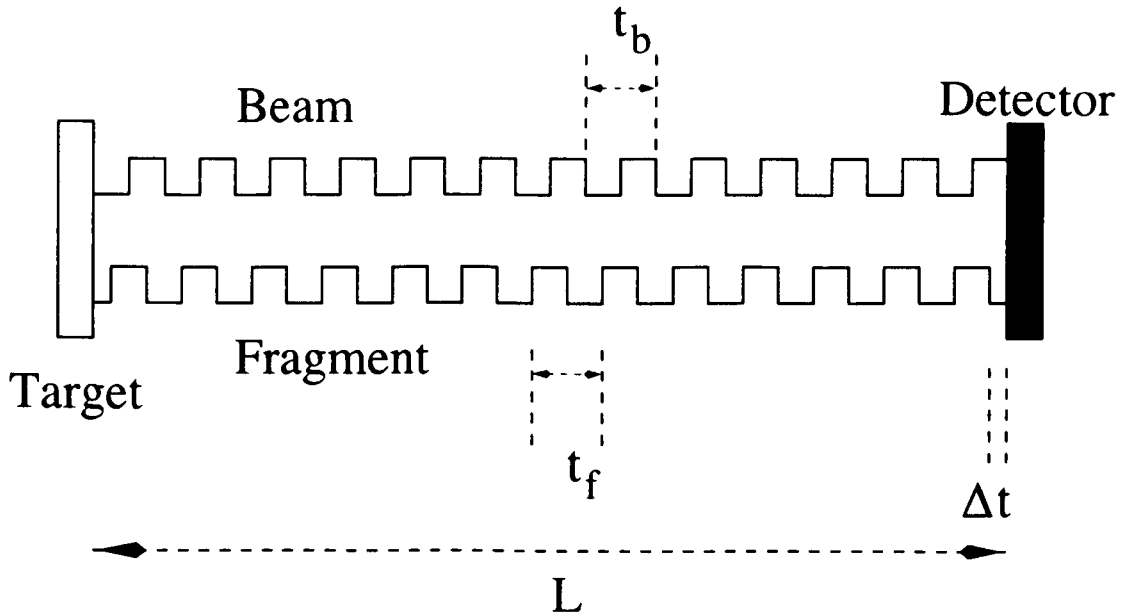
Figure 3.8: Schematic of the TOF measurement.

the time between the start of one beam pulse and the next one, is defined as t_b is also known exactly, see figure 3.8. There will be, therefore, a constant number of beam bunches between the target and detector and this is defined as n. The time for the beam particles to travel the distance L is defined as $n \cdot t_b$, and there is no phase difference between when a beam nucleus impinges on the target and stops in the implantation point. As the fragments travel with $v_{A,Z} < v_b$ they will take a time δt longer to travel the distance L. Hence, by measuring the time difference between a fragment striking the detector at the implantation point and the next beam pulse striking the target (which is equivalent to δt) a TOF measurement can be performed, as

$$t = n.t_b \tag{3.15}$$

where t is the TOF for the beam nuclei, and therefore

$$t_f = t + \delta t \tag{3.16}$$

t_f is the TOF for the fragments, and t is known, therefore t_f is equivalent to measuring δt. Since different isotopes have different $v_{A,Z}$ they will have different values of δt.

The time resolution limit for this method comes from a knowledge of the width of the beam pulse which is of the order of 1 % of a typical TOF value.

From equation 3.7 it can be seen that the velocity of a selected nucleus is inversely proportional to its A/q value and since the velocity is just L/t. then.

$$\frac{A}{Q} = \frac{t \times B\rho}{l} \tag{3.17}$$

Therefore, the TOF is proportional to the A/Q ratio of a nucleus.

A problem associated with this identification method can arise from nuclei which are not fully stripped which gives rise to charge state anomalies. This will cause the nuclei to be deflected by different amounts by the dipole magnet D1 (equation 3.7) and hence will have a lower value of δt. In this experiment, an example of a fully stripped nucleus would be $^{24}_{8}O$ which would have an A/Z value of 3.00. A possible contamination ion to $^{24}_{8}O$ would be $^{24}_{9}F^{8+}$ which also has an A/Q value of 3.00. This problem arises mainly for heavier beams and can be rectified by calculating the total energy that a fragment has from summing the E and ΔE contributions [Lewi 94, Grzy 95].

3.6.3   Identification Plots.

For complete particle identification, a combination of the previous particle identification systems (energy loss and TOF) is used. A two-dimensional (2-D) plot of ΔE (Z^2) versus TOF (A/Z) gives the typical identification plot, see figure 3.9. The plot shows lines of constant Z going horizontally and A/Z vertically.

Figure 3.9 represents a setting of the LISE3 optics centred on maximising the transmission of fully stripped ^{26}F nuclei and is therefore near the the neutron drip line. It can be seen that a broad range of nuclei in this region are also transmitted. The nuclei on the plot are identified from already known physical properties of the nuclei in this region. There are three nuclei which have the same TOF and hence the same A/Z; as the region of interest is near the neutron drip line then this would represent the ratio A/Z = 3. Previous studies of this region [Tara 97a] has shown that ^{24}O is the heaviest bound oxygen isotope. and that ^{28}F is unbound [Guil 89] so a *hole* should appear in the plot where this nucleus would be. It it therefore possible to label two of the A/Z = 3 nuclei accordingly: ^{24}O and ^{27}F. From there it is a simple process to identify the other nuclei produced. Another method of particle identification is to study the β-delayed γ rays emitted from the decaying nuclei. Some nuclei have already been studied. ^{31}Na for example [Guil 84, Klot 93] and determining

model with this method is more accurate ... to the fact that one is looking for already
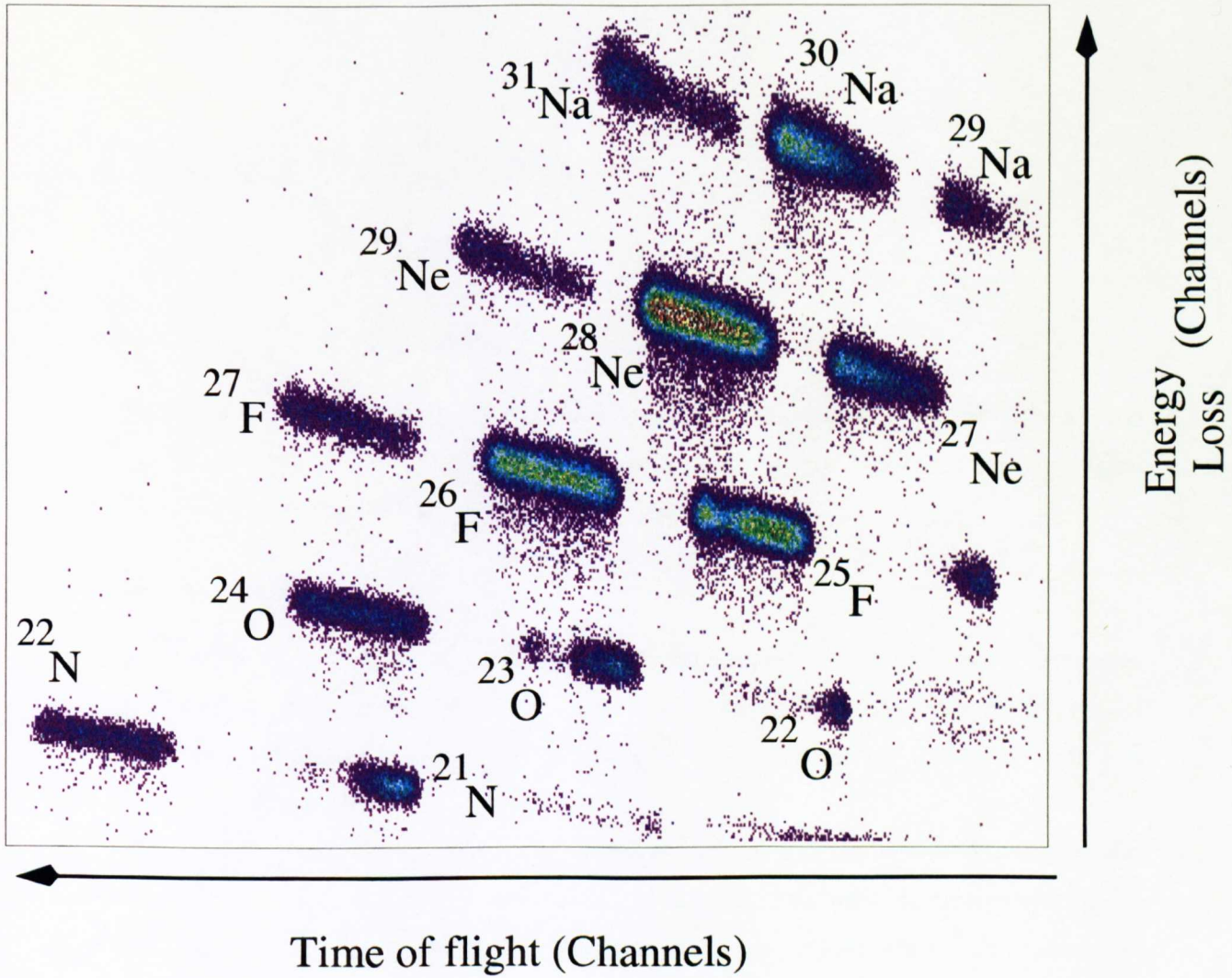... detected decay paths.

Figure 3.9: Two Dimensional spectrum of the energy loss versus TOF for the ^{26}F setting.

nuclei with this method is more accurate due to the fact that one is looking for already determined decay paths.

Chapter 4

The Experiment.

4.1 Experimental Setup.

The experiment was performed using the LISE3 spectrometer fragmenting $^{36}S^{16+}$ at a beam energy of 77.7 MeV/A. The average beam current was 0.5 eμA, and nuclei in the region A/Z $\approx$ 2.7 were selected with the LISE3 spectrometer.

4.1.1 Targets.

A combination of ^{12}C targets was used of varying thicknesses as well as some ^{181}Ta targets with ^{12}C backings on rotating and fixed target supports. A summary of the thicknesses of the different targets are given in tables 4.1 and 4.2 for those mounted on the rotating and stationary targets respectively.

The thicknesses of the targets in the rotating support were determined in a previous experiment [Lewi 96], and the thicknesses of the fixed targets were determined using the primary beam. This was performed by setting up the initial section of the LISE3 spectrometer for the observation of one of the charge states of the primary beam at the intermediate focal point: in this case $^{36}S^{16+}$ was selected using a magnetic rigidity for the first dipole of $B\rho_1 = 2.2319$ Tm. After the beam was focused at the intermediate focal plane the target was inserted into position and the change in $B\rho_1$ that was required to compensate for the energy loss due to the target of the chosen nuclear charge state was measured; the new value was found to be 2.179 Tm. This difference in the $B\rho_1$ value gave a direct measurement of the thickness of the target (see equation 3.10 and equation 3.11 which give the energy loss

39

Target Number	Target	Thickness
1	Empty	
2	^{12}C	100 μm
3	^{12}C	200 μm
4	^{12}C	300 μm
5	^{12}C	400 μm
6	^{12}C	500 μm
7	^{12}C	1000 μm
8	^{12}C	2000 μm
9	^{181}Ta + ^{12}C	288 μm + 127 μm
10	^{181}Ta + ^{12}C	377 μm + 125 μm

Table 4.1: The rotating targets and their thicknesses that were used in the experiment.

Target Number	Target	Thickness
1	^{181}Ta + ^{12}C	853.8 μm + 100 μm
2	^{181}Ta + ^{12}C	539.2 μm + 100 μm

Table 4.2: The stationary targets and their thicknesses that were used in the experiment.

proportional to $(\Delta B \rho_1)^2$).

The centre of the target position was measured by varying the target position and measuring the resultant beam intensity after the target. The edges of the target were reached when no beam intensity was measured. The thickness of the target as it was scanned toward the edges was also measured. This was important as the angle of the stationary target could be varied with respect to the beam so as to vary the thickness of the target. Any imperfections in the target thickness would, therefore, have to be compensated for. The beam intensity and position were monitored using a series of multiwire proportional counters positioned behind the target, which gave information on beam intensity and position and

which also gave the beam dimensions.

4.1.2 Energy Degraders.

The three different thicknesses of the ^{9}Be energy degraders used are given in table 4.3. The thicknesses of these degraders were determined in a similar method to that performed for the targets (section 4.1.1). The beam was focused at the first achromatic focal point and the correction required in the $B\rho$ value of the second dipole to compensate for the energy loss due to the degrader was determined, which gave a measurement of the thicknesses of the degraders

Degrader Number	Thickness
1	215 μm
2	553 μm
3	1047 μm

Table 4.3: The ^{9}Be wedges that were used in the experiment.

4.1.3 Detector Setup.

The projectile fragment detection system consisting of a six stack silicon telescope detector mounted in the small vacuum chamber connected at the final focal point of LISE3 and is shown schematically in figure 4.1. There was a thin (500 μm) aluminium strip in front of the telescope to ensure that the fragments of interest were stopped in the implantation element which was the fifth element of the telescope. The sixth element was used as a veto for the fifth element. On three sides of the thin-walled aluminium vacuum tube were situated the neutron detectors: fourteen either side and fourteen below, a total of forty-two detectors in all. Four large volume tapered 70% single crystal germanium detectors were situated at the end of the telescope for γ-ray detection (see figure 4.2). The β-detectors used were the fourth (Eβ4), fifth (Eβ5), and sixth (Eβ6) elements of the silicon detector telescope. An external clock ran continuously throughout the experiment and each event that was recorded in any of the detectors was marked with a clock time.
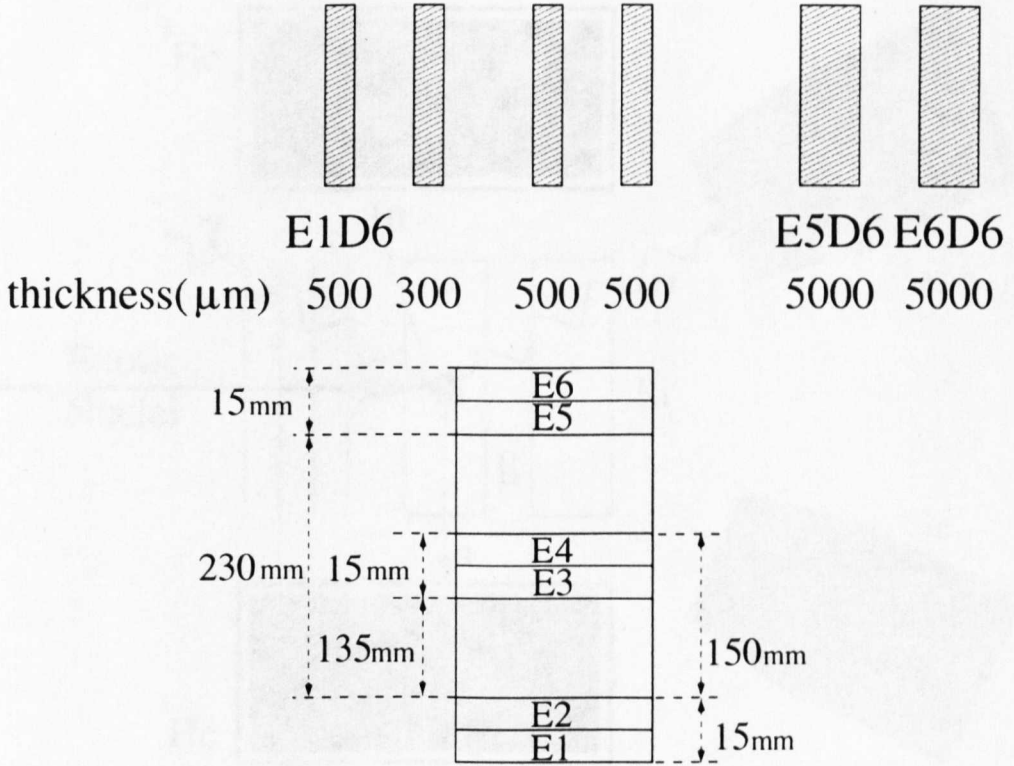
Figure 4.1: Schematic of the Li-drifted Si telescope detector, the first element was used as a ΔE detector, the implantation detector is the fifth element, and the sixth element is an E_{rej} detector.

The fourteen ^{3}He proportional detectors (section 3.4) were cylindrical in shape (see figure 4.3), and were surrounded by polyethene (to give a hexaglobal shape overall) as a moderator to slow the fast neutrons down to thermal energies. They were contained in a 1 mm thick cadmium foil sided box, with the uncovered front side facing the telescope. Cadmium was used due to the very large absorption cross-section for thermal neutrons ($\approx 4 \times 10^4$ barns [Knol 89]) which reduces background signals in the detectors. The detector dimensions are given in figure 4.3. Despite the heavy concrete shielding some neutrons leak through by consecutive reflection between the production and collection room of the LISE3 spectrometer, which gives rise to a continuous background.

The four germanium detectors are situated at the end facing the vacuum tube. The average distance of the centre of one of the detectors from the centre of the telescope cover was 7 mm and a total photopeak efficiency for a 1.33 MeV γ ray of 1.9% (see section 4.2.1)
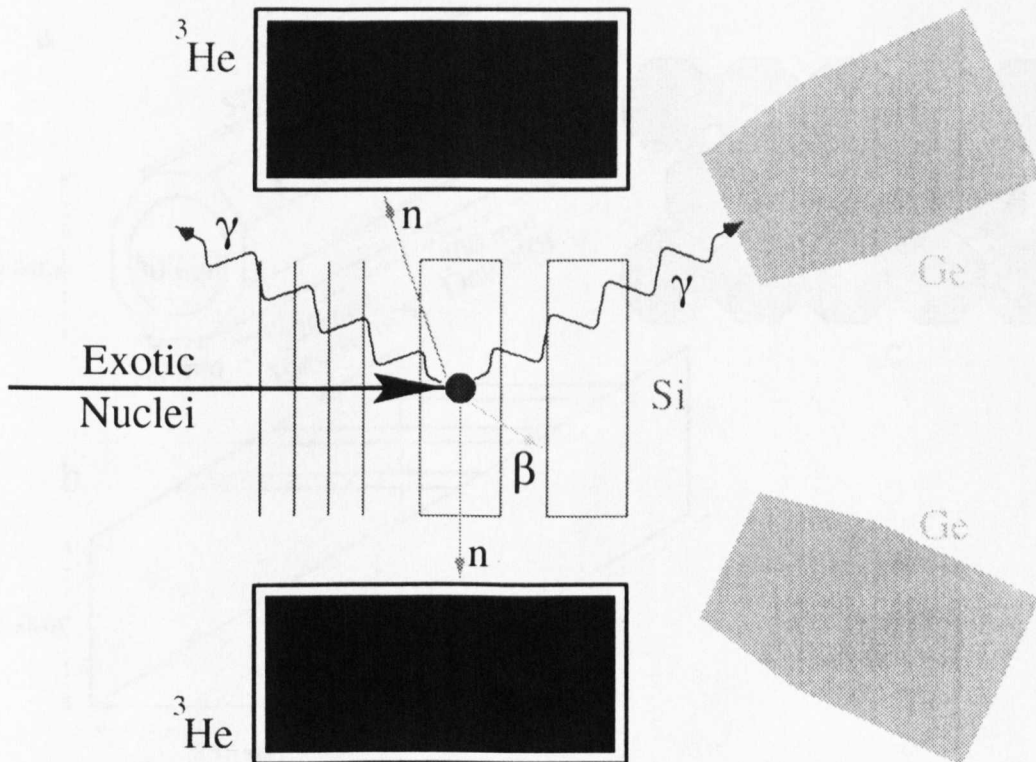
Figure 4.2: Schematic of the setup.

was possible.

Since heavy ions were being implanted in the fifth element of the telescope there was a dead time period of 1.6 ms between when an ion was detected and the ability to detect a β-particle efficiently. This placed a limitation on the detection of shorter-lived nuclei: for example, a nucleus which has a half life of 10 ms has a 10% probability of decaying during the period of dead time.

4.1.4 Electronics.

All data were processed by the GANIL acquisition system, which consisted of several CA-MAC crates connected to a computer via a microprocessor. The data acquisition consisted of two independent systems.Events of the first acquisition, responsible for the particle iden-tification (ΔE, E and TOF) and of the second acquisition (β-particles, γ rays and neutrons) were chronologically stored onto the same data cartridge. Each event was labelled by its time of arrival which was read from a quartz clock. The signal processing was performed
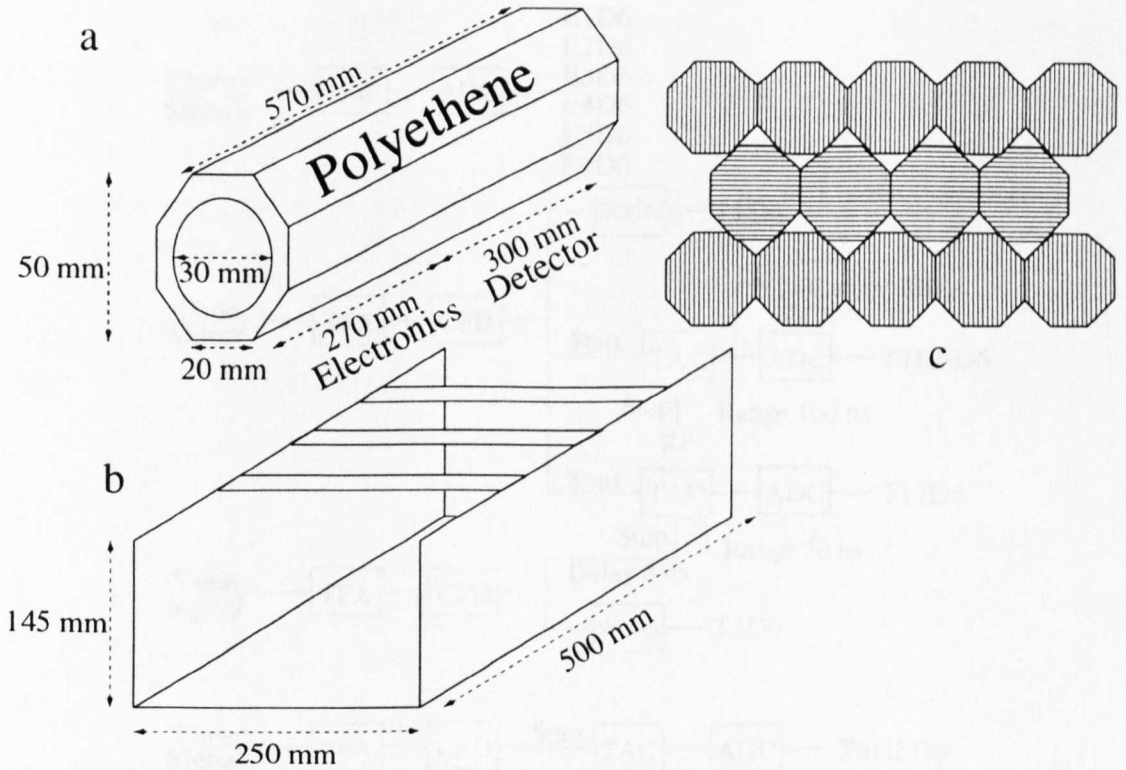
Figure 4.3: Schematic of the neutron detectors; a, shows the dimensions of the polyethene covered detector. Part b shows the dimensions of the cadmium walled container that the detectors were placed into. Part c shows the order of the stacking of the detectors.

by NIM (Nuclear Instrumentation Modules) processing units.

The triggers for the electronics were the detection of a heavy ion event in the ΔE detector at the final focal point or the detection of a β-event in Eβ5 or a γ-event in one of the germanium detectors.

The many different detectors used in this experiment required that there were many detector signals that needed to be processed. Although the basic premise for each of the detector signals to be processed is the same, shaping times and other details differ according to the type of radiation and the type of detector, the various circuits used to perform this will be shown in this section.

Heavy Ion Electronics

The processing for the signals from the six elements of the silicon stack telescope for the detection of a heavy ion event are summarised in figure 4.4. The energy signals for all

```
                                    E1D6
                                    E2D6
Energy        ┌─────┐   ┌─────┐     E3D6
Signals  ─────┤ AMP ├───┤ ADC ├──── E4D6
              └─────┘   └─────┘     E5D6
                                    E6D6

                                 ┌──────┐
                              ┌──┤Scaler├──── T1D6
                              │  └──────┘
                                                    ┌─────┐
                                                 ┌──┤ SCA ├──── BIL
                              │                  │  └─────┘
Time      ┌─────┐   ┌─────┐   │  Start ┌─────┐   │  ┌─────┐
Signal ───┤ TFA ├───┤ CFD ├───┤ ───────┤ TAC ├───┼──┤ ADC ├──── T1HFD6
          └─────┘   └─────┘   │        └─────┘      └─────┘
                              │        Stop│    Range 100 ns
                              │         RF
                              │  Start ┌─────┐      ┌─────┐
                              └ ───────┤ TAC ├──────┤ ADC ├──── T12D6
                                       └─────┘      └─────┘
                                        Stop│    Range 50 ns
                                       Delay 8 ns
                                        ┌──────┐
                                     ───┤Scaler├──── T2D6
                                        └──────┘

Time      ┌─────┐   ┌─────┐ Start ┌─────┐   ┌─────┐
Signal ───┤ TFA ├───┤ CFD ├───────┤ TAC ├───┤ ADC ├──── T5HFD6
          └─────┘   └─────┘       └─────┘   └─────┘
                                   Stop│    Range 100 ns
                                    RF
```
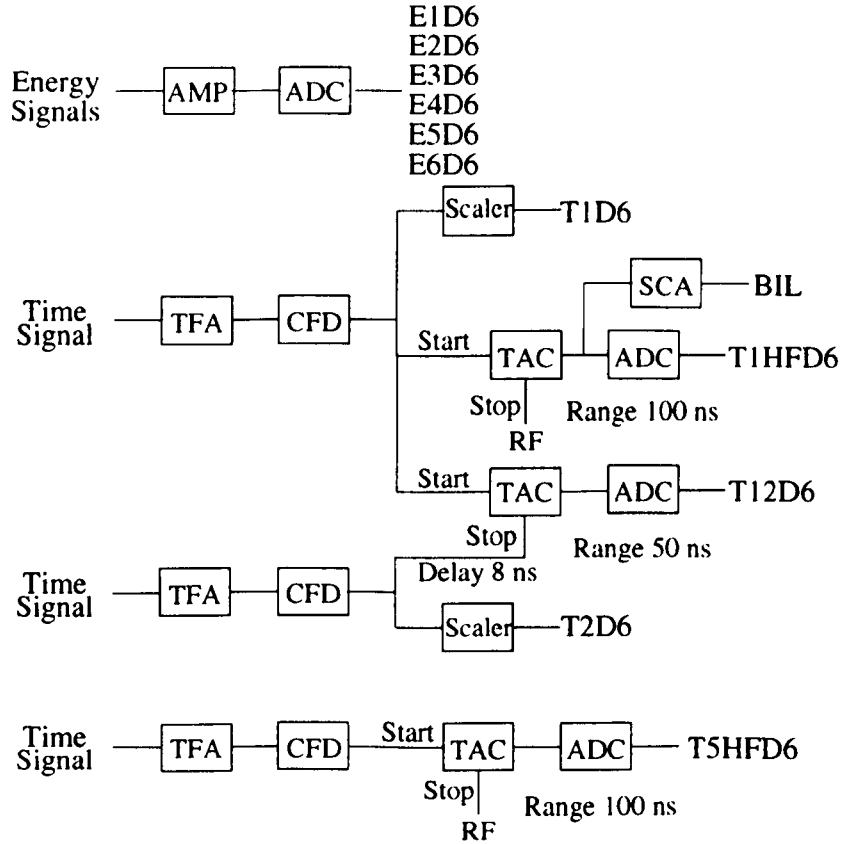
Figure 4.4: Schematic of the electronics for the heavy ion detectors at the final focal point.

the elements of the silicon telescope were processed with a linear amplifier and the signal from the amplifier was passed to the GANIL data acquisition system via the relevant ADCs (Analogue to Digital Convertors). The time signals from elements E1D6, E2D6 and E5D6 were passed through TFAs (Timing Filter Amplifiers) which provided an amplified signal with fast (nanosecond) timing whose output signals are passed through a CFD (Constant Fraction Discriminator) which produced a digital output. The time signal from E1D6 provided the start signal for two TACs (Time to Amplitude Convertors). One TAC was stopped by a time signal from E2D6, thus giving the time difference for a heavy ion passing between the two detectors. The other TAC was stopped by the radio frequency (RF) pulse of the beam each time it impinged on the target, which gave a measurement of the time of flight of the particles. A SCA (Single Channel Analyser) provided a logic output pulse whose output signal provided the trigger for the data acquisition system. The final output from the CFD went to a scaler which counted the number of logic pulses in a predetermined

time range, the output of which was sent to the data acquisition system. The time signal from E5D6 also provided a time of flight measurement with respect to the RF.

Beta Electronics

The energy signals from β detectors were passed through a linear amplifier and to an ADC which passed the signals on to the data acquisition system (see figure 4.5). The time
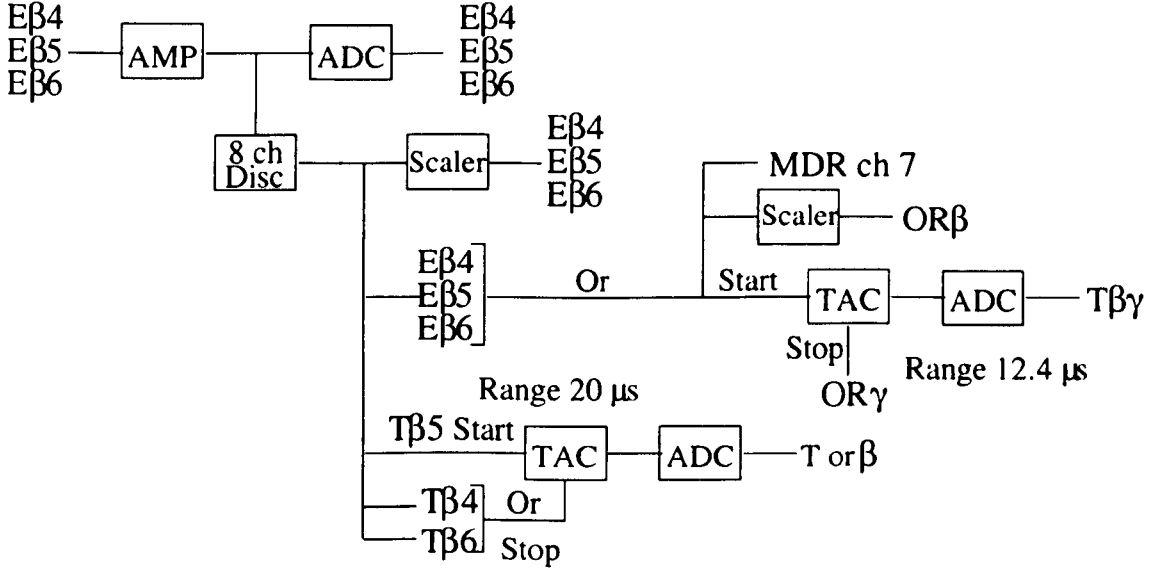

Figure 4.5: Schematic of the electronics for the β detectors.

signals for the β detectors were taken directly from the energy signals of telescope elements four, five and six. A discriminator after the linear amplifier provided a conversion of the analogue pulses to digital pulses for the scalers and TACs. One TAC was started with a β signal from any of the detectors and stopped with a pulse from any of the γ-ray detectors with a coincident window of 12.4 μs. Also measured were coincident events between adjacent β detectors with a coincident window of 20 μs.

Gamma Electronics

The energy signals from the germanium detectors were amplified and processed using linear amplifiers and the signals from these were passed to the data acquisition system by ADCs, figure 4.6. The time signals from the germaniums were amplified by a TFA and the outputs were converted to logic pulses by a CFD, one output of which went to a scaler which counted the number of individual germanium detector signals in a predetermined
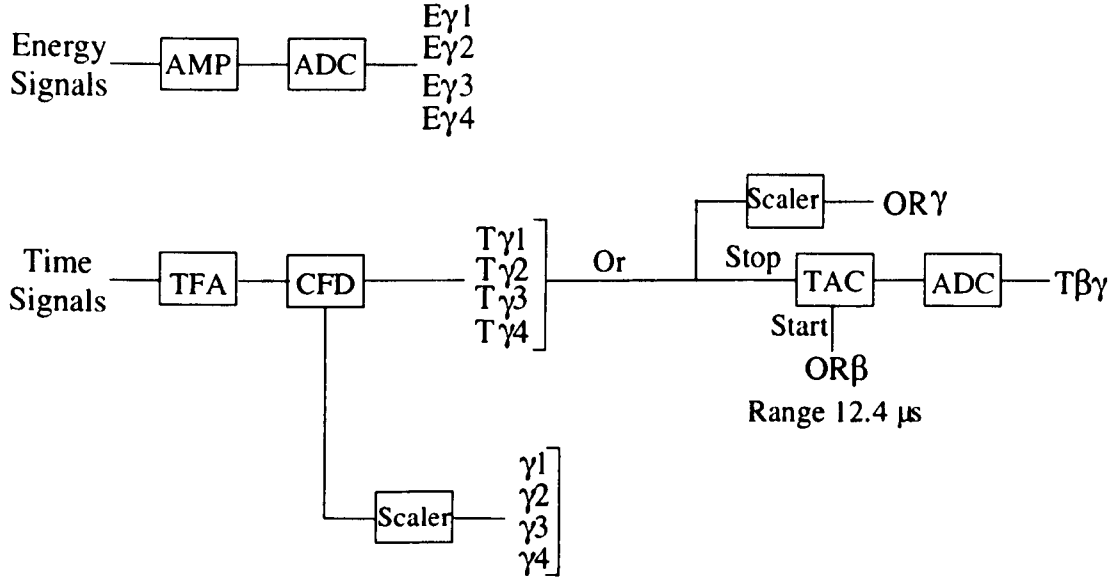
Figure 4.6: Schematic of the electronics for the germanium detectors.

time. The four germanium time signals were also used as an OR to stop the TAC which had a start from the β detectors.

Clock

The signal from the heavy ion detectors acted as one of the master triggers that stopped the acquisition system (figure 4.7), the time of arrival was stamped with a clock time by the OPA system (open data acquisition) which had a resolution of $100\mu s$.

4.2 Energy and Efficiency Calibration.

4.2.1 Germanium detectors.

The detection efficiency of a γ-ray detector, ϵ, is dependent upon the energy of the incident radiation, E_γ. At $E_\gamma \gtrsim 300$ keV the efficiency slowly decreases as a function of energy; below this energy the efficiency decreases rapidly due to the fact that low energy γ rays are stopped quickly in the front of the detector where the electric field is not homogeneous and therefore the charge collection time is poorly defined.

For the purpose of calibrating and gain-matching the γ-ray detectors as well as obtaining the efficiency of the detectors a ^{152}Eu source was used.
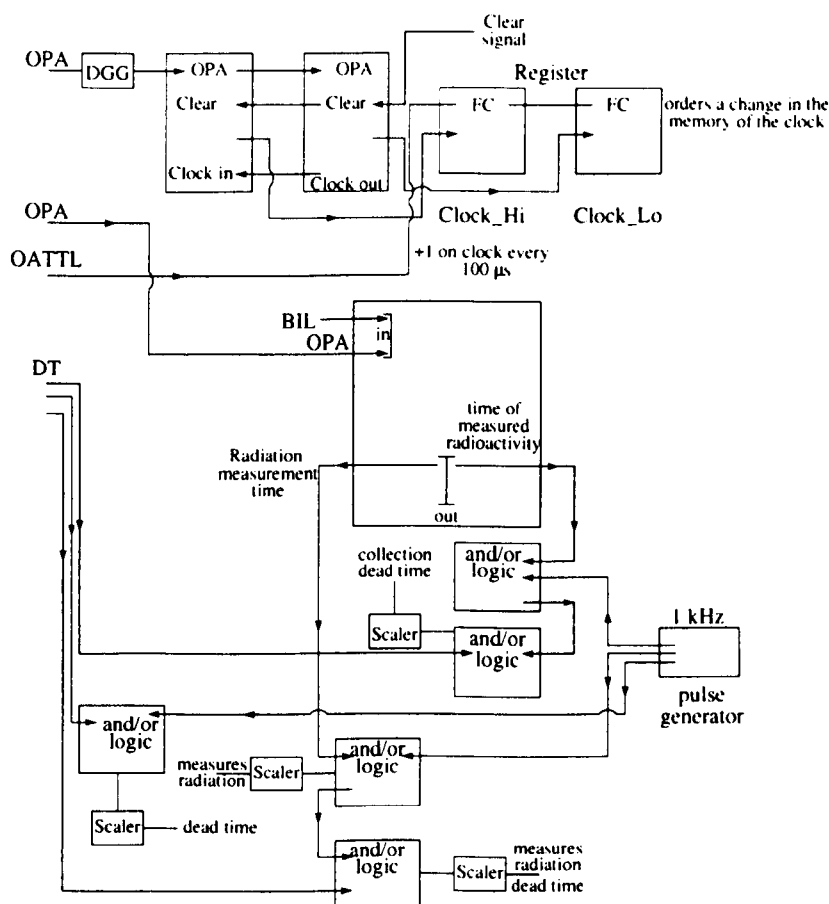
Figure 4.7: Schematic of the electronics for the clock.

The intensities of the transitions in the spectrum produced were measured and were compared with known relative intensities using the EFFIC Oak Ridge computer code. This produces an efficiency curve of relative intensity against energy. The gain-matching procedure eliminates the problem produced by the different gains of the germanium detectors.

The source was placed into the detector array and data were recorded. The data were then sorted into individual spectra for each of the detectors and a linear function was applied to align all the gains for each individual detector.

Figure 4.8 shows the low energy portion of the γ-ray spectra for the four germanium detectors with the ^{152}Eu source, on each of the spectra the low energy threshold is indicated.
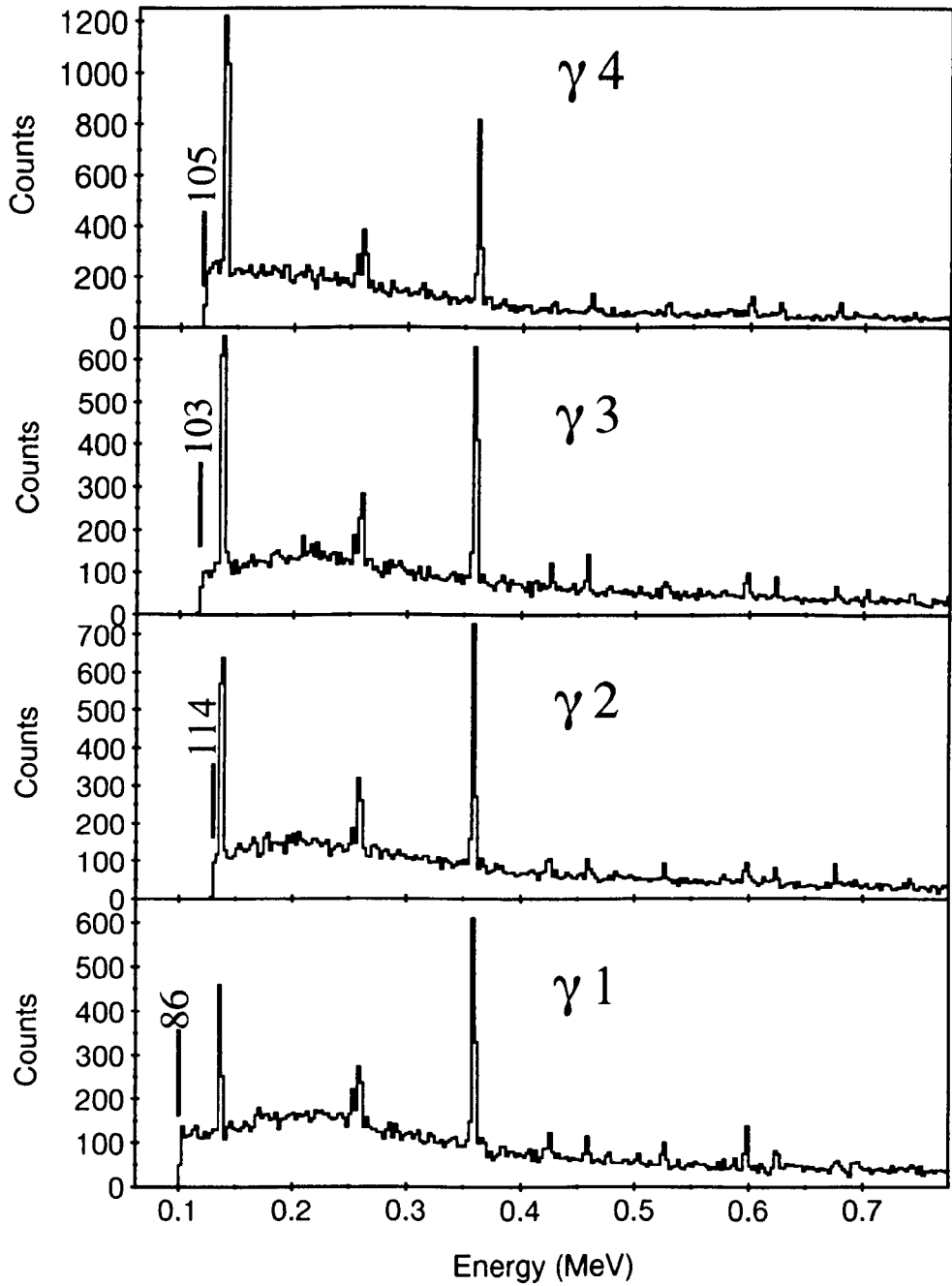
Figure 4.8: The low energy portion of the γ ray spectra for the four germanium detectors with the ^{152}Eu source; indicated on the diagram is the low energy threshold for each detector.

4.2.2 Silicon detectors.

As the ions passed through detector E1D6 (figure 4.1), which was used to identify the fragments, the energy calibration was performed for this element of the telescope. No energy requirements were set on elements two, three or four and element five was used as an implantation detector. Element six was a veto detector for element five.

A three nuclide α-source was used, with energies at 5.155 MeV, 5.487 MeV and 5.806 MeV, for the low energy calibration. To prevent inconsistencies from the extrapolation of the energy calibration to higher energies the energy losses are calculated [Lewi 96, Bazi 93] for a nucleus that has already been measured using the LISE3 spectrometer for the energy deposited in the E1D6 detector. This calculated energy loss was then compared with experimental results. The energy deposited by a ^{31}Na nucleus, for example, was calculated for a specific setting and then compared with experimental results. This can be performed as there have been previous studies on ^{31}Na [Lewi 96] using similar settings of the LISE3 spectrometer.

^{31}Na was also used for the determination of the efficiency of the β-detectors. The yield of ^{31}Na is known and a weighted average of the previous half-life measurements gives a value of 17.3 ± 0.3 ms. From this the expected fraction of ^{31}Na to decay between two time limits (t_1 and t_2) can be determined from

$$F = \frac{\int_{t_2}^{t_1} e^{-\lambda t} dt}{\int_{0}^{+\infty} e^{-\lambda t} dt}, \qquad (4.1)$$

where F is the expected number of ^{31}Na decaying between time limits and λ is $ln2/t_{1/2}$. F can be related to the observed number of β-particles (N_β) by

$$N_\beta = N_{^{31}Na}\epsilon_\beta F, \qquad (4.2)$$

where $N_{^{31}Na}$ is the yield of ^{31}Na and ϵ_β is the β-efficiency. By taking various time windows a weighted average gives a value for ϵ_β to be 62.6 ± 0.4 %.

4.3   Methods of Data Analysis.

Each event that was recorded was written out as a group of data words and these words contain the energy of the radiation, the detector that detected that radiation and the time

at which the radiation was detected. Also recorded for the heavy ion detectors was the time of detection relative to the RF pulse

As previously described, the projectile fragments are identified by plotting the energy-loss in the first element versus the TOF for the nuclei produced, see section 3.6.

Sections of a 2-D matrix can be selected by setting software gates in off line analysis, these gates can be set round the nucleus or nuclei of interest.Time conditions can then be set on coincident β-γ events to occur within a certain interval after the detection of a selected ion. All β-γ coincident events that occur within this specified time interval are incremented into a one-dimensional (1D) spectrum. Although this ensures that β-delayed γ-ray events from the implanted nucleus are measured, it does mean that other events originating from other nuclei can also detected. If a β-γ coincident event does occur, the energy of the β-particle can be incremented into an β-particle energy spectrum and the energy of the γ ray can be incremented into a γ-ray energy spectrum if required. The time difference between the initial ion and the subsequent coincident β-γ event can be incremented into a time spectrum. The setting of different time windows aids in the identification of the γ-ray transitions from the daughter nucleus, as the intensity of the γ rays will increase as the time window increases but after a few half-lives the peak intensity will not increase so dramatically whereas the intensity of the background lines, having a random rate, will constantly increase. The implantation rate in the detectors was reasonably low, (see section 5.1) hence, it is possible to set time gates of a reasonable time period, four or five half-lives for example for some nuclei.

Chapter 5

Results.

5.1 The Data.

Due to the selection processes made by the LISE3 spectrometer it is necessary to vary the settings of LISE3 to optimise for nuclei which have different magnetic rigidities. This was achieved by varying the value of $B\rho_1$, and if necessary the target and degrader thicknesses as well, and by keeping $B\rho_2$ constant. Essentially the spectrometer is set for the observation of one nucleus, which is called the setting nucleus, and due to the acceptance of the spectrometer and the high energies involved a region of isotopes around the setting nucleus are collected which have similar A/Z values. A list of the setting nuclei and the relevant $B\rho$ values, targets and energy degraders required to observe them as well as the implantation rate for each setting are listed in table 5.1.

The identification plots for each of these settings are shown in figures. 5.1, 5.2 and 5.3, and the nuclei that were produced in the region of study are shown in figure 5.4.

The yields of the different nuclei in the region of interest at each of the settings are shown in table 5.2.

5.1.1 Beta-Particle Spectrum.

The β-particles from the decay of the exotic nuclei are detected in the fourth-, fifth- and sixth elements of the silicon telescope, and the corresponding energy spectra are shown in figure 5.5. To ensure clean gating, 2-D matrices of β-β coincident events are produced for the adjacent β-detectors and these are shown in figure 5.6. The lower energy region is
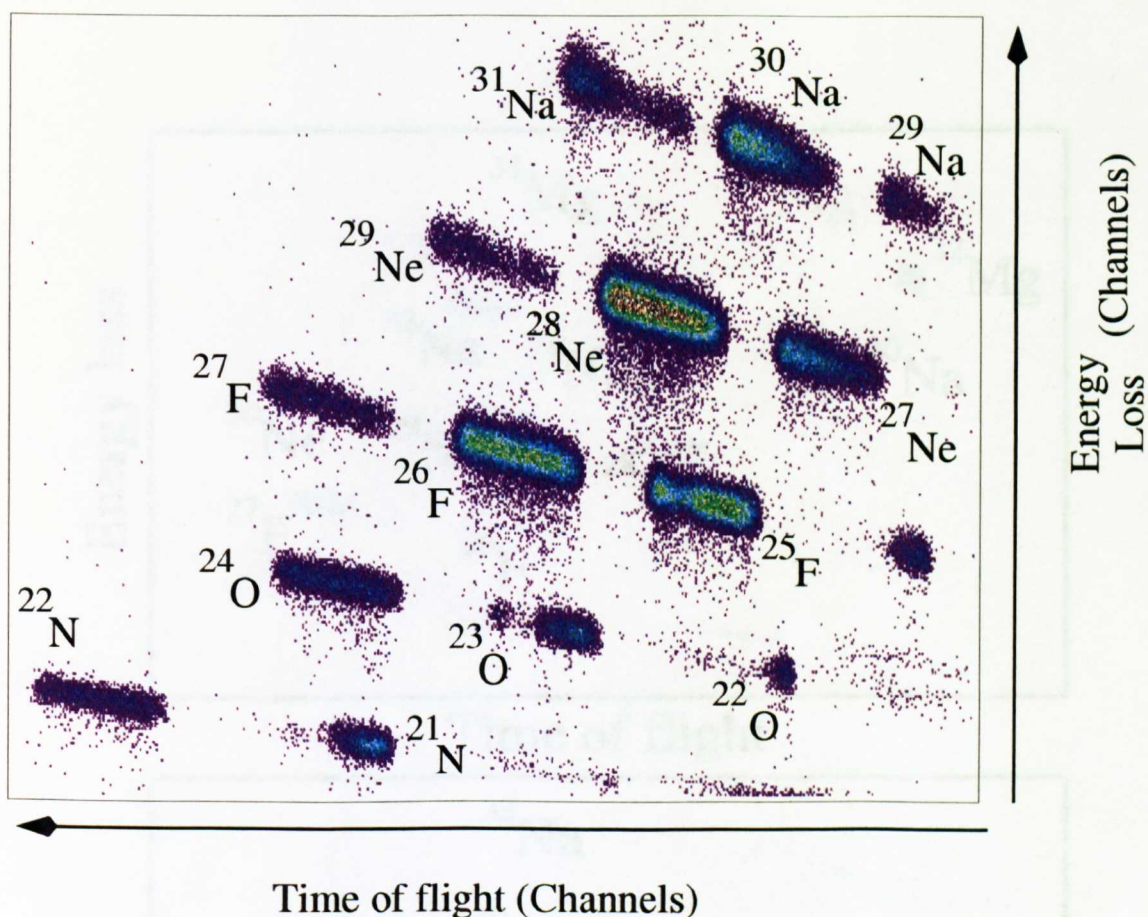
Figure 5.1: Two Dimensional spectrum of the energy loss versus TOF for the ^{26}F setting.

dominated by electronic noise and the higher energy region contains low energy protons as well as incomplete charge collection of protons in EB5. Two-dimensional β-β coincident gates are set so as to only take clean events.

The background rate in the β-detectors is measured as the time difference between a β-event and the next ion implant. It is measured this way because if an ion is measured followed by a subsequent β-particle, there is a strong possibility that the detected β-particle is associated with the decay of the implanted ion.

The random background half-life for the ^{31}Na setting using this method was fitted to be 104.57 $\pm$ 2.75 ms, as will be seen this is longer than the half-lives of the nuclei studied in this work. For the other settings, ^{26}F has a random background half-life of 410 $\pm$ 5 ms; ^{29}F has a random background half-life of 4110 $\pm$ 850 ms; ^{19}B has a random background

Figure 5.2: Identification plots of time of flight (increasing from right to left) (equivalent to A/Z) against energy loss (equivalent to Z) for the setting nuclei ^{31}Na (top) and ^{29}F (bottom).
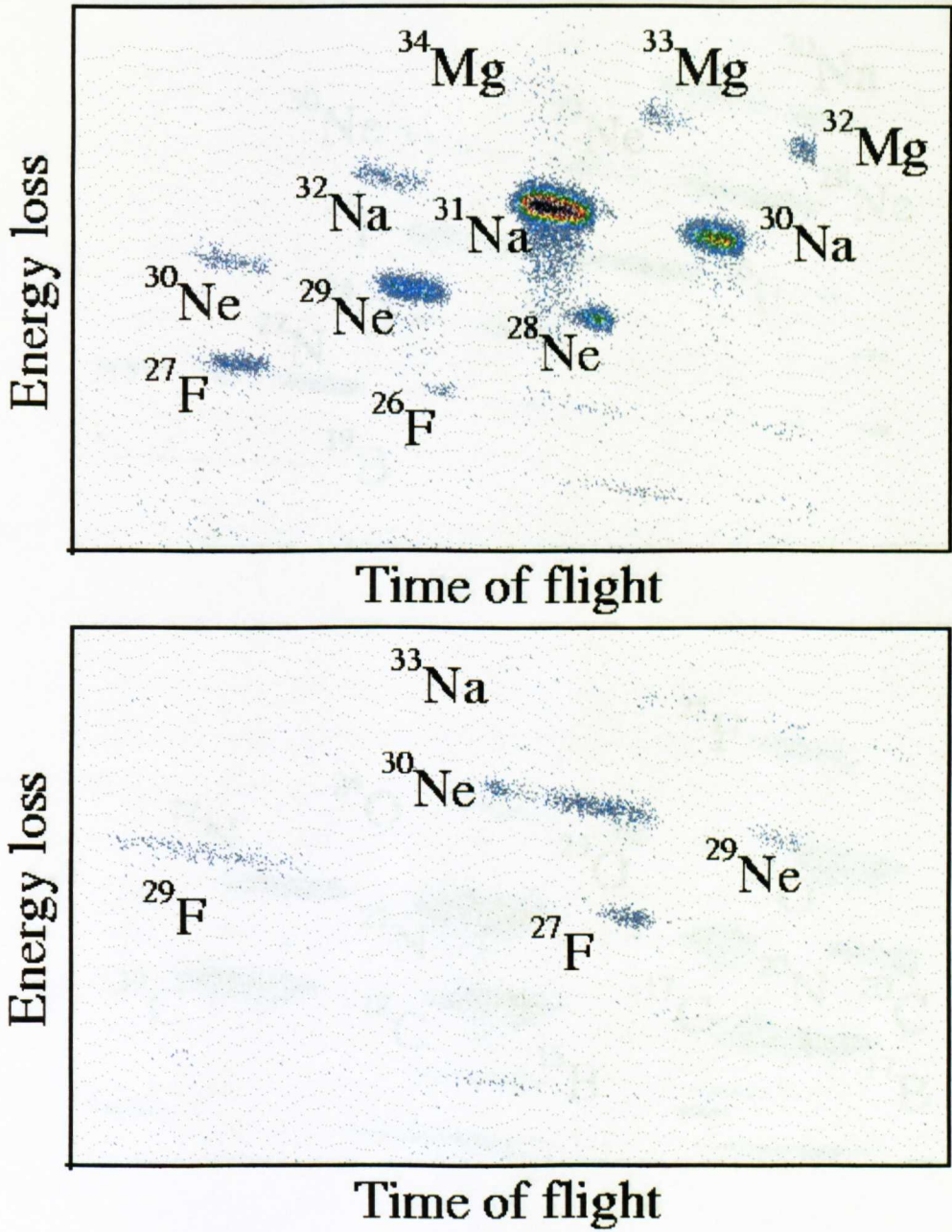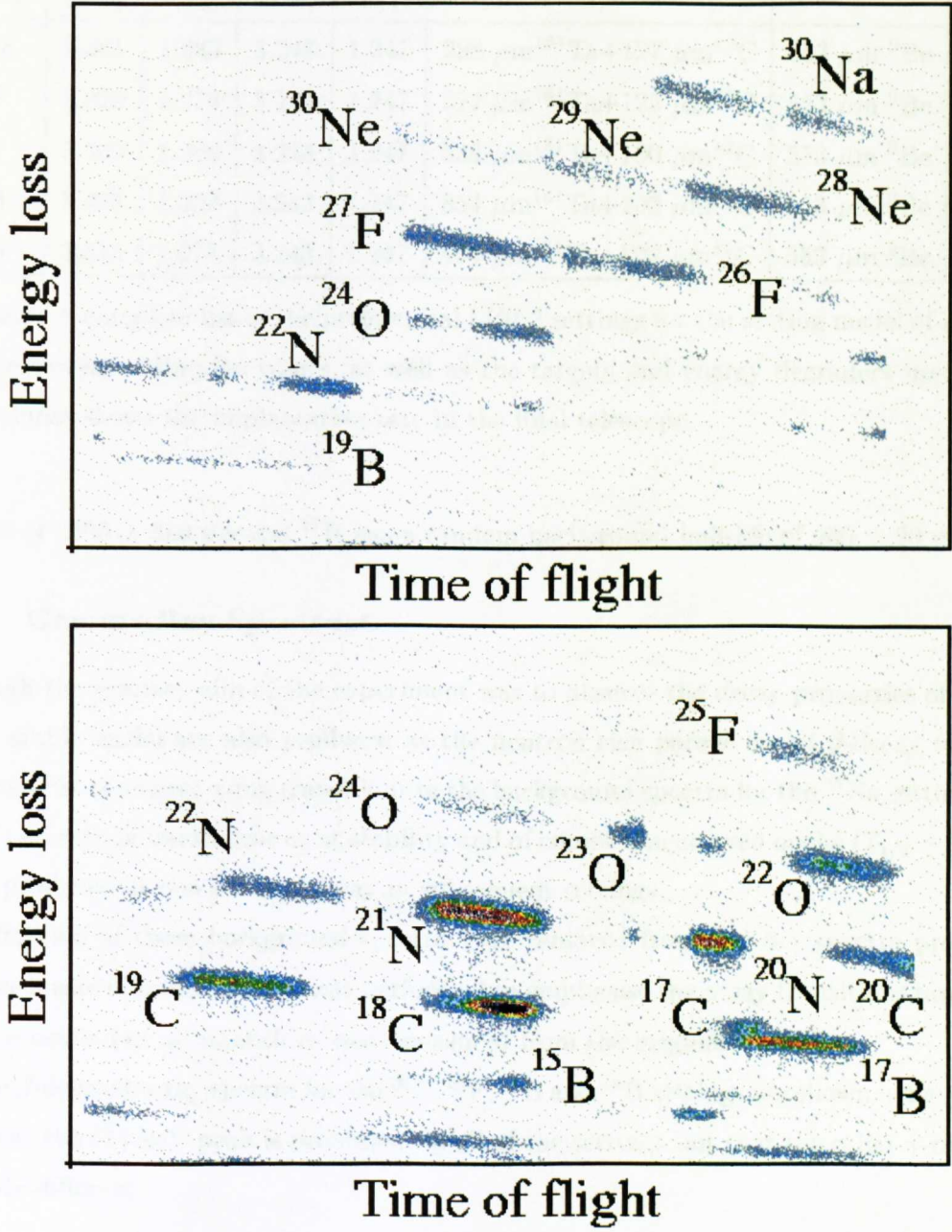
Figure 5.3: Identification plots of time of flight (increasing from right to left) (equivalent to A/Z) against energy loss (equivalent to Z) for the setting nuclei ^{19}B (top) and ^{17}B (bottom).

Setting nucleus	$B\rho_1$ (Tm)	B_1 (T)	$B\rho_2$ (Tm)	B_2 (T)	Target	Degrader	Rate s^{-1}
^{31}Na	3.341	1.285	3.243	1.247	288 μm^{181}Ta+127 μm^{12}C	553 μm ^{9}Be	4.98
^{26}F	3.328	1.279	3.243	1.247	377 μm^{181}Ta+125 μm^{12}C	553 μm ^{9}Be	3.61
^{29}F	3.350	1.288	3.243	1.247	539 μm^{181}Ta+100 μm^{12}C	553 μm ^{9}Be	0.08
^{19}B	3.335	1.282	3.243	1.247	854 μm^{181}Ta+100 μm^{12}C	553 μm ^{9}Be	3.62
^{17}B	3.315	1.275	3.243	1.247	854 μm^{181}Ta+100 μm^{12}C	553 μm ^{9}Be	5.44

Table 5.1: A complete list of the preferential LISE3 settings for the setting nuclei of interest and the corresponding Bρ values, as well as the targets and energy degraders used. The final column shows the implantation rate in the final telescope.

half-life of 2900 ± 360 ms and ^{17}B has a random background half-life of 960 ± 20 ms.

5.1.2 Gamma-Ray Spectrum.

Although the primary aim of the experiment was to observe the decay properties of exotic nuclei, stable nuclei are also produced as the neutron rich parent nuclei β-decay towards stability. The strongest γ-ray transitions in the background spectra for the ^{31}Na setting (figure 5.7) arise from nuclei near or at stability and of course longer-lived nuclei ($T_{1/2} \sim$ hours) can, if produced at one setting, decay in subsequent settings.

A fraction of these background spectra were removed from the β-γ spectra produced from the nuclei of interest. This was performed to emphasise the γ-ray transitions produced by those nuclei but all intensities were measured from the original spectra.

The β-delayed γ-ray spectra for the ^{26}F, ^{29}F, ^{17}B and ^{19}B settings are shown in figure 5.8. Note that the 511 keV peak is prominent in all of the settings but that the other γ-rays are generally different.

5.2 ^{31}Na.

The N = 20 isotone $^{31}_{11}$Na$_{20}$ has been studied in detail before in two previous experiments [Guil 84, Klot 93] and was used in this analysis as a reference nucleus due to its well known

Z	N	Nucleus	A/Z	^{31}Na	^{26}F	^{29}F	^{19}B	^{17}B	Total
5	12	^{17}B	3.40					32359	32359
	14	^{19}B	3.80				337		337
6	12	^{18}C	3.00					73800	73800
	13	^{19}C	3.17					24257	24257
7	12	^{19}N	2.71		1370				1370
	13	^{20}N	2.86					25655	25655
	14	^{21}N	3.00		5186			81549	86735
	15	^{22}N	3.14		3901		3476	3346	10723
8	14	^{22}O	2.75					10210	10210
	15	^{23}O	2.88		4427			1989	6416
	16	^{24}O	3.00		7189		1561	604	9354
9	16	^{25}F	2.78		37669			1022	38691
	17	^{26}F	2.89	202	44693		2602		47497
	18	^{27}F	3.00	1426	3606	626	4608		10266
	20	^{29}F	3.22			651			651
10	17	^{27}Ne	2.70		13275				13275
	18	^{28}Ne	2.80	4742	97896		2380		105018
	19	^{29}Ne	2.90	4319	2546	215	543		7623
	20	^{30}Ne	3.00	740		2086	174		3000
	21	^{31}Ne	3.10			23			23
11	18	^{29}Na	2.64		1581				1581
	19	^{30}Na	2.73	16230	23424		1950		41604
	20	^{31}Na	2.82	93771	6446				100217
	21	^{32}Na	2.91	814					814
	22	^{33}Na	3.00			155			155
12	20	^{32}Mg	2.67	662					662
	21	^{33}Mg	2.75	420					420
	22	^{34}Mg	2.83	164					164

Table 5.2: A list of the yields of the nuclei produced in the region of study. The settings are listed at the top as a function of the setting nuclei.
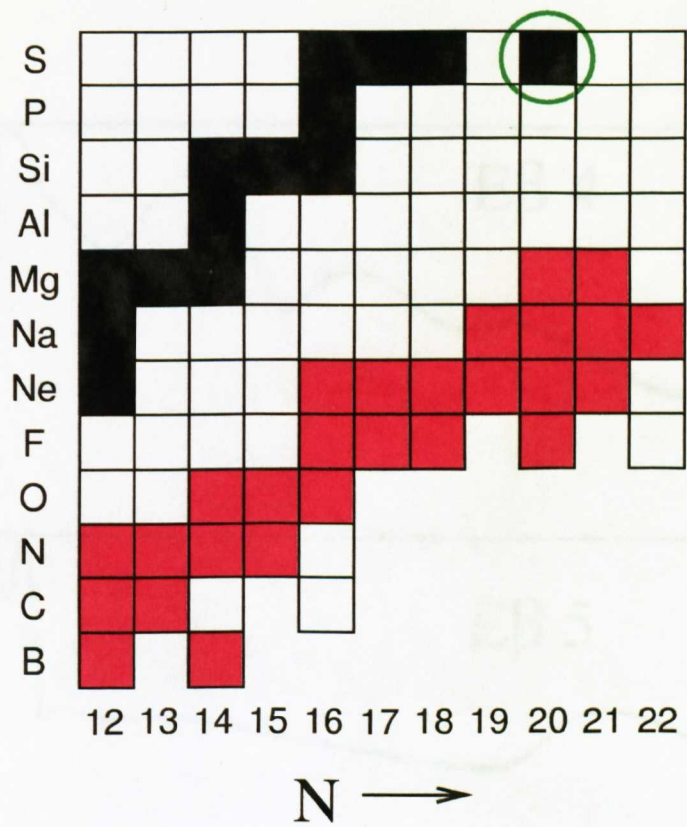
Figure 5.4: A section of the Segré chart showing the nuclei produced in the experiment. The nucleus with the green circle around it is the beam nucleus: ^{36}S. The nuclei shown in red were the ones produced in this experiment.

half-life, 17.7 ± 0.5 ms, and β-delayed γ-decay and neutron emission properties.

During the experiment a total of 100217 ^{31}Na nuclei were produced from two settings of the LISE3 spectrometer, see table 5.3.

LISE3 Setting	Yield	Rate s^{-1}
^{31}Na	93771	2.17
^{26}F	6446	0.07
Total	100217	

Table 5.3: The LISE3 settings with the yield of ^{31}Na produced at those settings and the implantation rate.

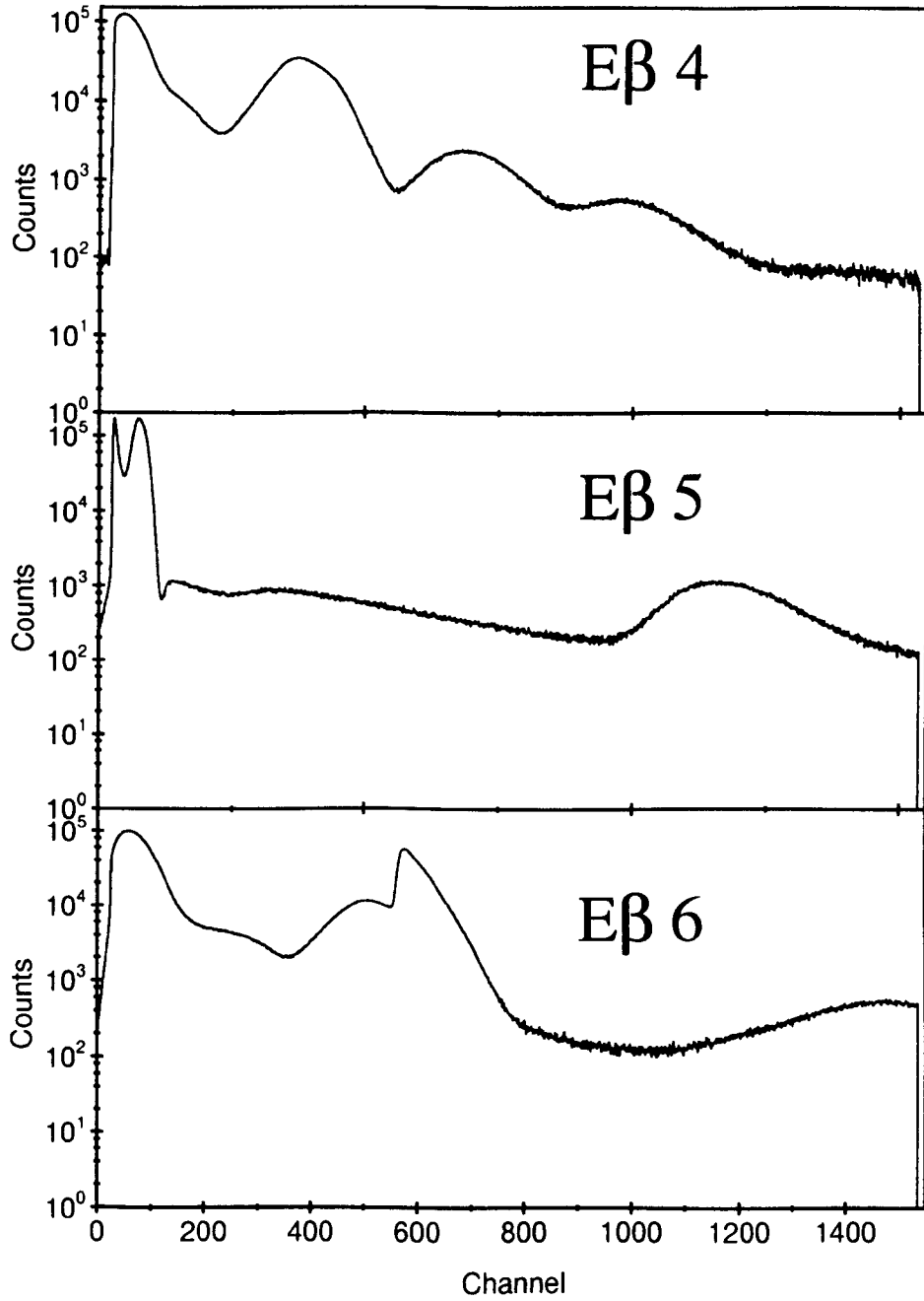Figure 5.5: The β-particle spectra associated with the final three elements of the silicon telescope, Eβ4, Eβ5 and Eβ6.

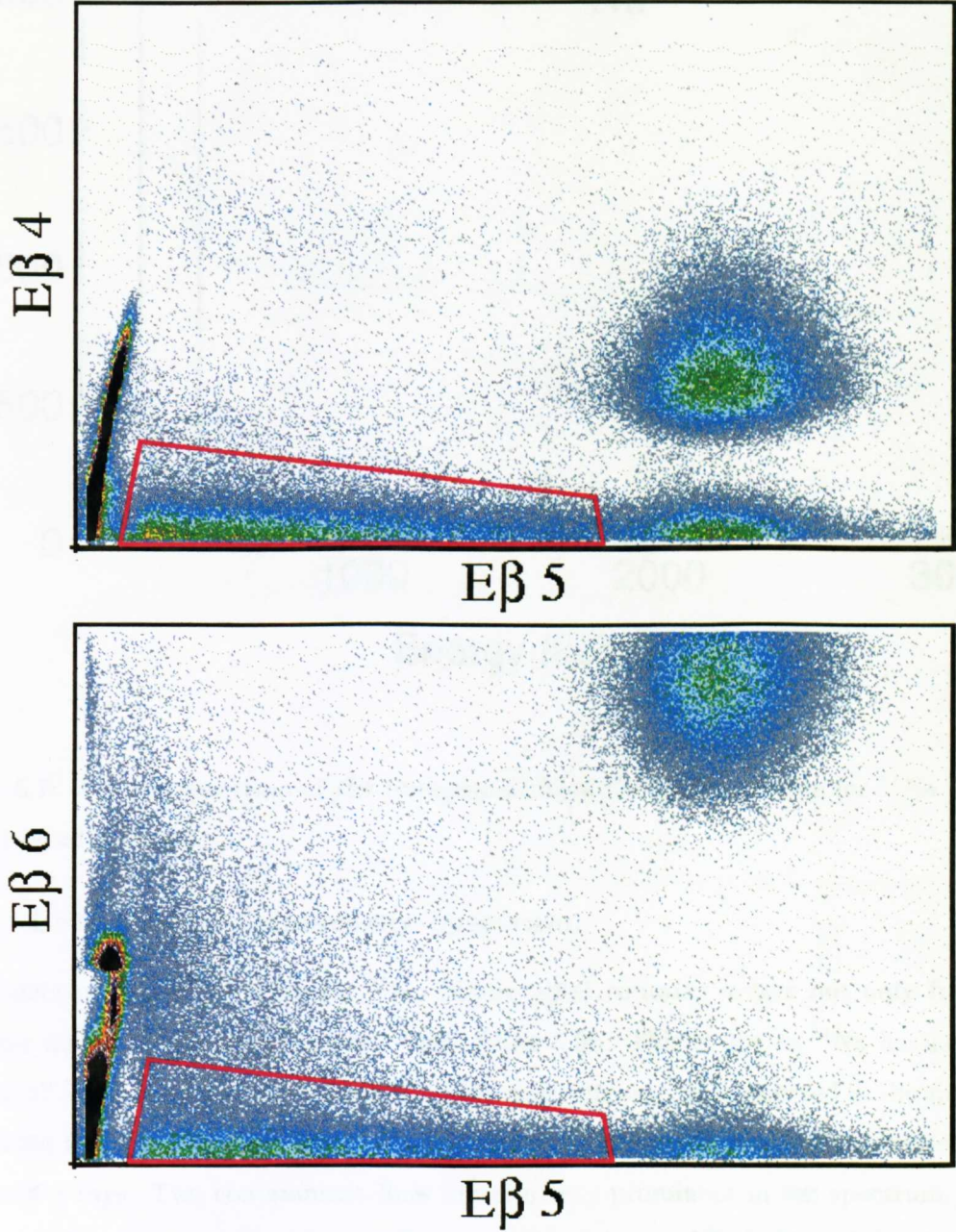Figure 5.6: 2-D matrices of β-β coincident events. The top matrix shows events that occur in β-detectors 4 and 5, and the bottom matrix shows events that occur in β-detectors 5 and 6. The gates used are shown in red on each matrix.
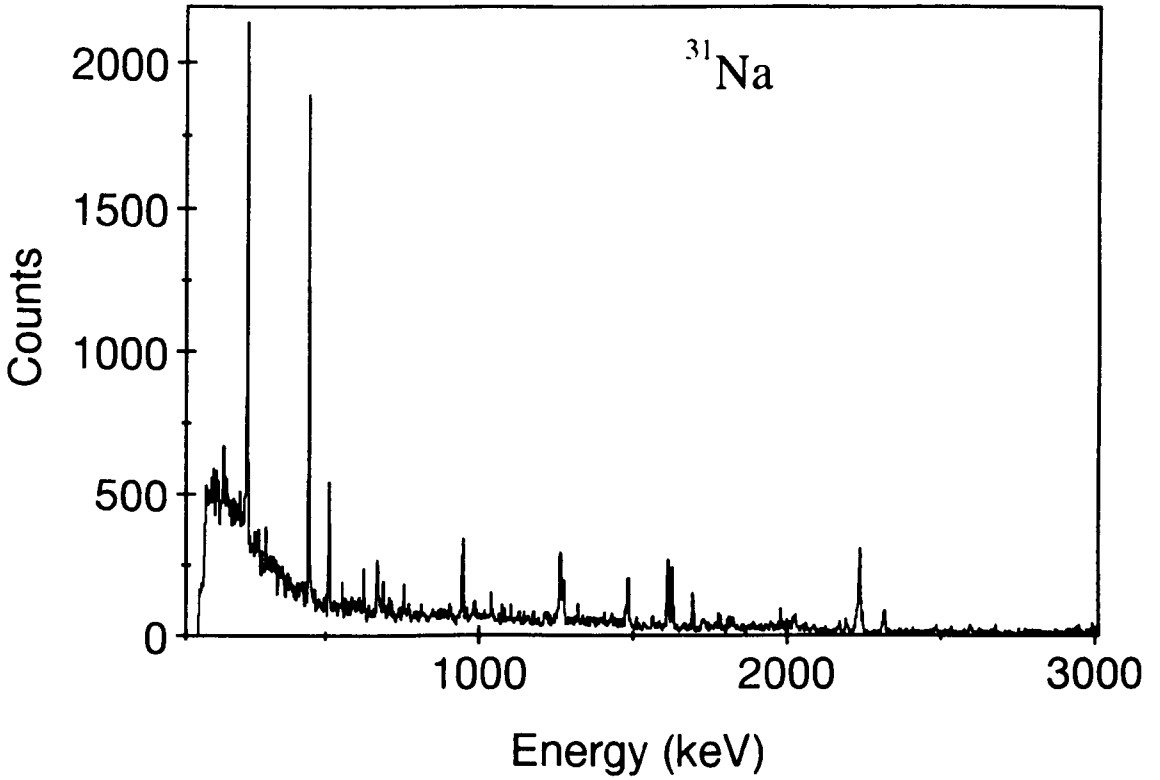
Figure 5.7: A γ-ray spectrum of the background from the LISE3 setting for ^{31}Na looking for β-delayed γ events.

5.2.1 Beta-delayed Gamma-ray Spectrum.

The β-delayed γ-ray spectrum for ^{31}Na (figure 5.9a) contains γ-rays not only from the daughter nucleus ^{31}Mg but also from ^{30}Mg, figure 5.9b. This is due to ^{31}Na having a P_{1n} value of 37.5 ± 5.5 % [Guil 84], and indeed, the most intense γ ray observed in the spectrum is the 1483 keV transition in ^{30}Mg. Table 5.4 summarises the energies and intensities of the measured γ rays. Two contaminant lines are also very prominent in the spectrum. These are the two known γ-ray transitions in ^{30}Al from the β-decay of ^{30}Mg [Detr 79]. The reason for the intense nature of these lines is the large amount of A = 30 nuclei that are produced in some of the LISE3 settings used, and since these nuclei decay through ^{30}Al there is a high probability that the 244 keV and 444 keV transitions in ^{30}Al are detected instead of the β-γ in coincidence from the nuclei of interest. Some A = 31 nuclei can also decay via
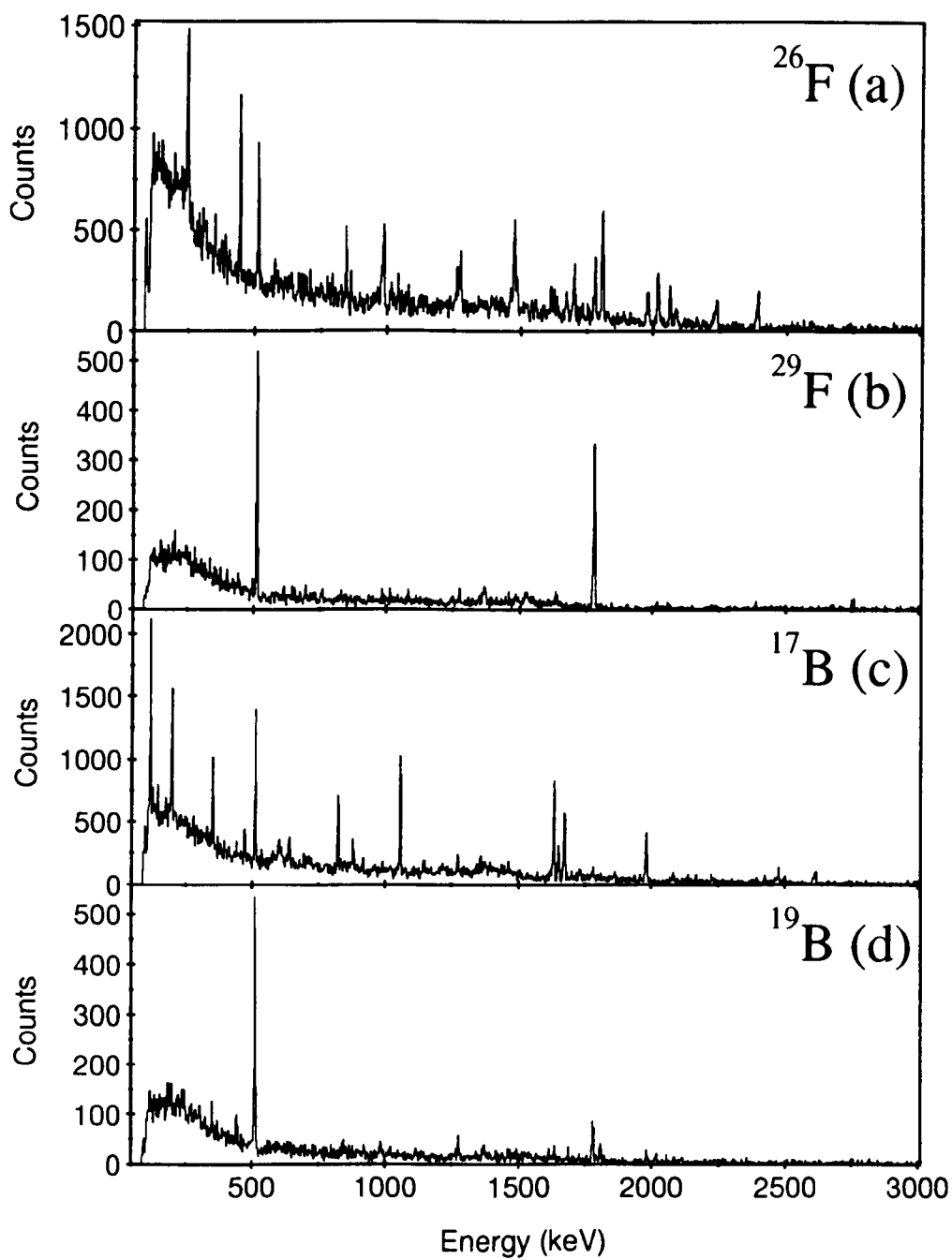
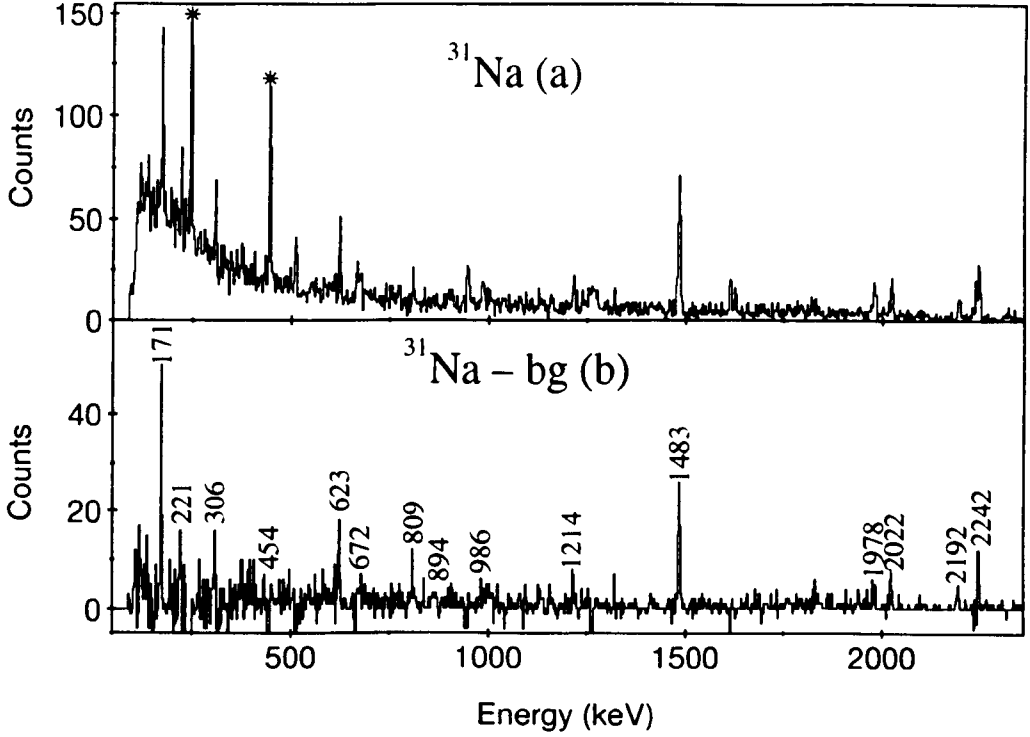Figure 5.8: The γ-ray spectra of the backgrounds from the LISE3 settings for ^{26}F, ^{29}F, ^{17}B and ^{19}B.

Figure 5.9: Spectrum (a) shows the β-delayed γ-events within 50 ms of the detection of a ^{31}Na. Spectrum (b) shows the corresponding background subtracted spectrum. The peaks labelled with a star in spectrum (a) are known to be transitions in ^{30}Al and the energies in b) represent known γ rays in ^{30,31}Mg.

the β-n channel which leads to the production of ^{30}Al.

Although β-delayed two-neutron emission is a possibility for ^{31}Na, it is a weak decay channel, with a probability of 0.9 $\pm$ 0.2 % [Klot 93], and there are no γ rays observed in the de-excitation of excited states in ^{29}Mg in the present work. Not all of the γ rays from the P_{0n} channel reported in [Klot 93] are observed here either, probably because some of them have weak branching ratios. A comparison of the relative intensities for the β-delayed γ-ray transitions from ^{31}Na from this experiment with the work performed by Klotz el al. [Klot 93] shows that they are consistent (fig 5.10).

$E_\gamma{}^1$ (keV)	Transition Number[3]	I_γ (relative)	I_γ (per 100 decays)	$I_\gamma{}^4$ (per 100 decays)
171.1 ± 0.5	1	35 ± 2	5.0 ± 0.5	5.4 ± 0.9
220.5 ± 0.6	2	14 ± 2	1.0 ± 1.0	2.2 ± 1.4
306.2 ± 0.5[2]	3	14 ± 2	2.0 ± 0.5	2.0 ± 0.7
453.5 ± 1.5	4	3.0 ± 1.0	0.5 ± 0.5	0.4 ± 0.1
623.1 ± 0.5	5	23 ± 2	3.0 ± 0.5	3.6 ± 0.6
671.8 ± 1.1	6	12 ± 1	1.0 ± 0.5	1.8 ± 0.3
808.5 ± 0.5	7	9.5 ± 1.5	1.0 ± 0.5	1.5 ± 0.3
893.8 ± 0.8	8	5.0 ± 1.0	1.0 ± 1.0	0.9 ± 0.2
985.5 ± 0.6[2]	9	13 ± 3	2.0 ± 0.5	1.8 ± 0.7
1213.5 ± 0.8	10	10 ± 1	2.0 ± 0.5	1.6 ± 0.3
1482.6 ± 0.4[2]	11	100	14 ± 1	15.0 ± 5.0
1978.2 ± 0.7[2]	12	29 ± 3	4.5 ± 1.0	4.4 ± 1.5
2022.0 ± 0.7	13	29 ± 3	5.0 ± 1.0	4.5 ± 0.9
2192.4 ± 0.8	14	26 ± 3	3.5 ± 1.0	4.0 ± 0.8
2244.3 ± 0.7	15	86 ± 5	11 ± 1	13.5 ± 2.5

Table 5.4: Energy and intensity of γ-rays observed in the β-decay of ^{31}Na corrected for $\epsilon_{\beta-\gamma}$. [1] in ^{31}Mg unless otherwise stated. [2] in ^{30}Mg subsequent to β-delayed one-neutron emission. [3] relates to fig 5.10. [4] taken from [Klot 93], ^{31}Na decays to the ^{31}Mg ground state with a probability of 26 ± 9 %.
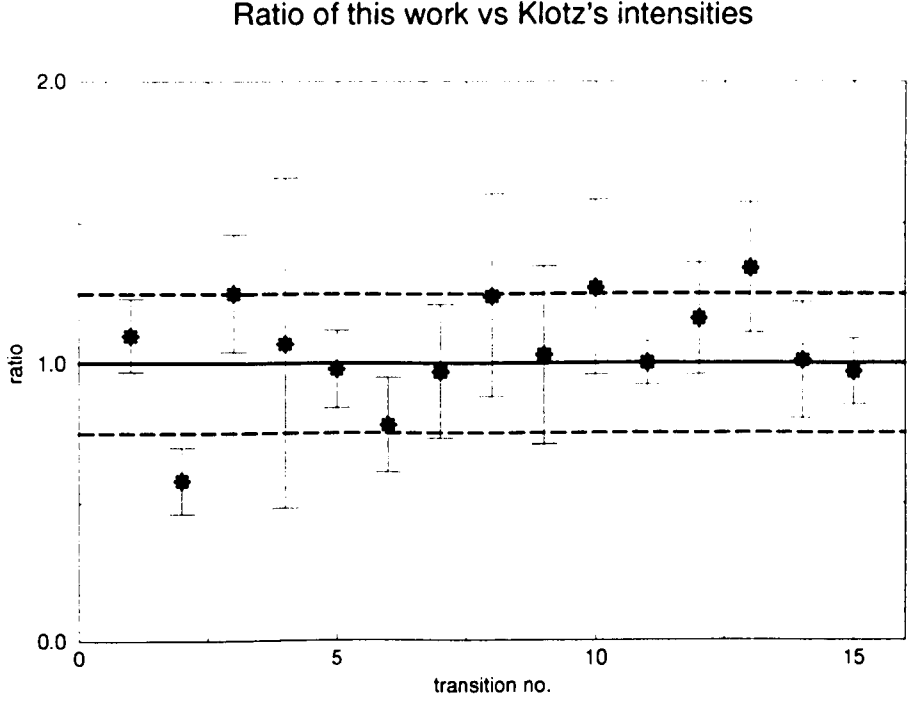
Ratio of this work vs Klotz's intensities

Figure 5.10: Graph to show the ratio of the relative intensities of the γ-rays measured from this experiment and those obtained by Klotz *et al.* [Klot 93]. The transition numbers are displayed in table 5.4. The solid line represents the average ratio value of 1.01 while the dotted lines refer to one standard deviation $\pm$ 0.25 from the average value.

5.2.2 Half-life Analysis and Results.

The half-life analysis was performed by measuring the time difference between an ion implant and a subsequent β-delayed γ ray. Taking any β-γ coincident event produced the half-life curve in figure 5.11. This decay curve was fitted using the method of least squares [Bevi 69]. The range over which the fit was performed was varied and an average value of 17 $\pm$ 1 ms was obtained.

In the ^{31}Na γ-ray spectrum (figure 5.9) there is quite a large background at low energies, as well as large contaminant lines and transitions observed in nuclei that are from different nuclei, rather than ^{31}Na, which can lead to variations in the measured half-life of the nucleus. A method of removing these contaminants is to set gates on the known β-delayed γ rays in regions of low background. The result of setting these gates is to produce a series of
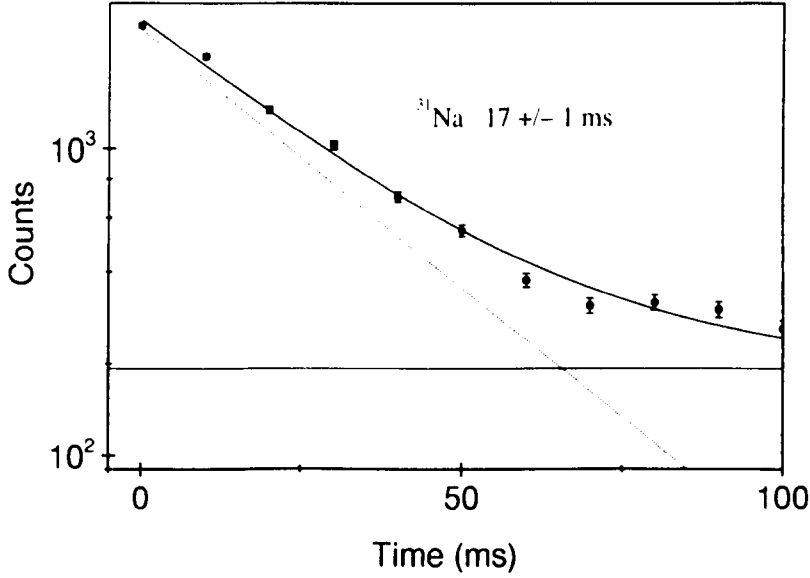
Figure 5.11: Half-life decay curve associated with the β-decay of ^{31}Na. This curve was produced by taking all β-delayed γ-rays emitted within 100 ms after a ^{31}Na ion is detected.

decay curves as shown in figure 5.12. This has a two-fold effect: not only does it reduce the contaminants in the half-life curve but also vastly reduces the statistics so it is not possible to perform a least-squares fit to the data. An alternative method to find the half-life is to do a maximum likelihood fit to the data [Schm 84] [Meye 75].

For this analysis the starting point was kept constant and the end point of the fit was varied. Maximum likelihood lifetimes were measured and an average value of the half-life was obtained. The fractional number of the total counts at each end point value used was calculated and compared to the experimental results, and those contributions to the average half-life from end points which gave anomalous half-life measurements were ignored. This process was repeated until the points used gave consistent life-time results with the experimental results and an average was taken of these values. The error on this average value was calculated by adding in quadrature the standard deviation on the average value and an average value from the errors given from the maximum likelihood fit. The measured half-life is: 18 ± 1 ms from gates set on the 1483 keV, 1978 keV, 2022 keV and 2244 keV transitions and this result is consistent with previous measurements of ^{31}Na
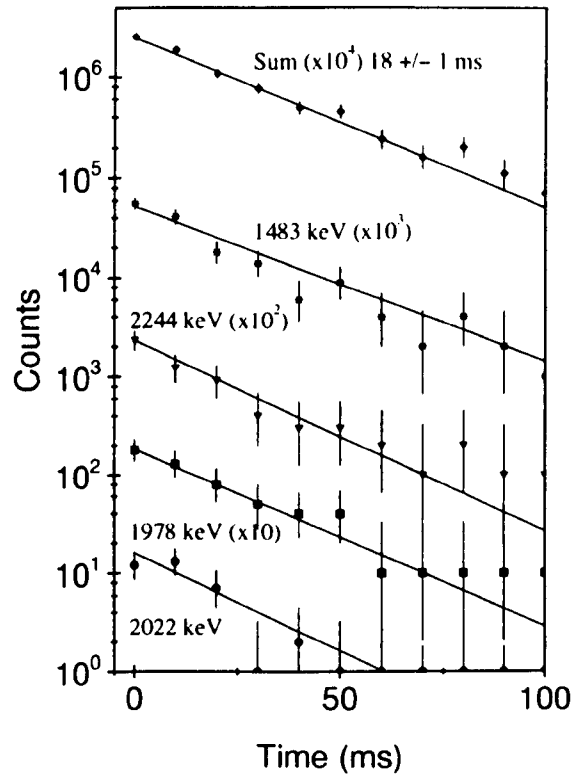
Figure 5.12: Half-life decay curves associated with the β-decay of ^{31}Na. These curves were produced by setting gates on four of the known β-delayed γ-rays from the decay of ^{31}Na and performing a maximum likelihood fit to the curves.

[Guil 84, Klot 93].

5.3 ^{17}B.

Bowman *et al.* [Bowm 74] confirmed the particle stability of $^{17}_{5}$B$_{12}$ in 1974 using a 4.8 GeV proton beam impinging on a uranium metal target. The matter radius of ^{17}B, determined by Tanihata [Tani 88], was found to be anomalously larger than expected compared to lighter boron isotopes and has been interpreted as being due to two neutrons orbiting a stable N = 2Z core [Hans 93] and forming a Borromean system.

^{17}B undergoes β-decay to ^{17}C with a previously determined half-life of 5.08 $\pm$ 0.05 ms

[Dufo 88]. ^{17}C has a measured S_n value of 729 ± 18 keV [Audi 95] and there are three bound states predicted in ^{17}C [Warb 89]. Nolen et al. [Nole 77] using the reaction ^{48}Ca(^{18}O,^{17}C) at 102 MeV found evidence for a doublet at 292 ± 20 keV, while a further experiment by Fifield et al. [Fifi 82] at a higher beam energy of 112 MeV observed an excited state at 295 ± 10 keV.

^{17}B is also unusual as it has a large range of β-delayed neutron emission multiplicities as measured by Dufour et al. [Dufo 88] by fragmenting a ^{22}Ne beam at 60 MeV/A. They measured values of P_{0n} to be 21 ± 2 %; P_{1n} to be 63 ± 1 %; P_{2n} to be 11 ± 7 %; P_{3n} to be 3.5 ± 0.7 % and P_{4n} to be (4 ± 3) × 10^{-3} %.

During the present experiment a total of 32359 ^{17}B nuclei were produced at one setting of the spectrometer with an implantation rate of 0.47 nuclei s^{-1}.

5.3.1 Beta-delayed Gamma-ray Spectrum.

The γ-ray spectrum associated with the decay of ^{17}B is shown in figure 5.13a. Figure 5.13b shows the corresponding background subtracted spectrum. The transition at 741 keV has been previously assigned to a transition in ^{15}C [Ajze 91] via the P_{2n} decay channel (see tables 5.5 and 5.6) and has a measured full width half maximum (FWHM) of 9.5 ± 1.0 keV which is wider than expected from a comparison with the ^{152}Eu source, figure 5.14. This

E_γ (keV)	I_γ	I_γ (per 100 decays)
741.1 ± 0.6	1180 ± 210	3.6 ± 0.6

Table 5.5: Energy and intensities of the γ-ray observed in the β-decay of ^{17}B to ^{15}C.

extra width is attributed to the Doppler broadening of the 741 keV state from the recoil of the daughter nucleus after the double neutron emission. The typical energies for β-delayed neutrons are ∼ 1 → 3 MeV in this region [Raim 96] for states being populated in ^{16}C and the measured width can be reproduced with neutrons of energies in the region of 2.5 → 3.5 MeV. A possible source of one of the neutrons is the known unbound level in ^{16}C at ≈ 6.11 MeV [Till 93] which lies higher in energy than the 741 keV state in ^{15}C, there are no known states in ^{17}C higher in energy than this level. No other γ rays are observed which
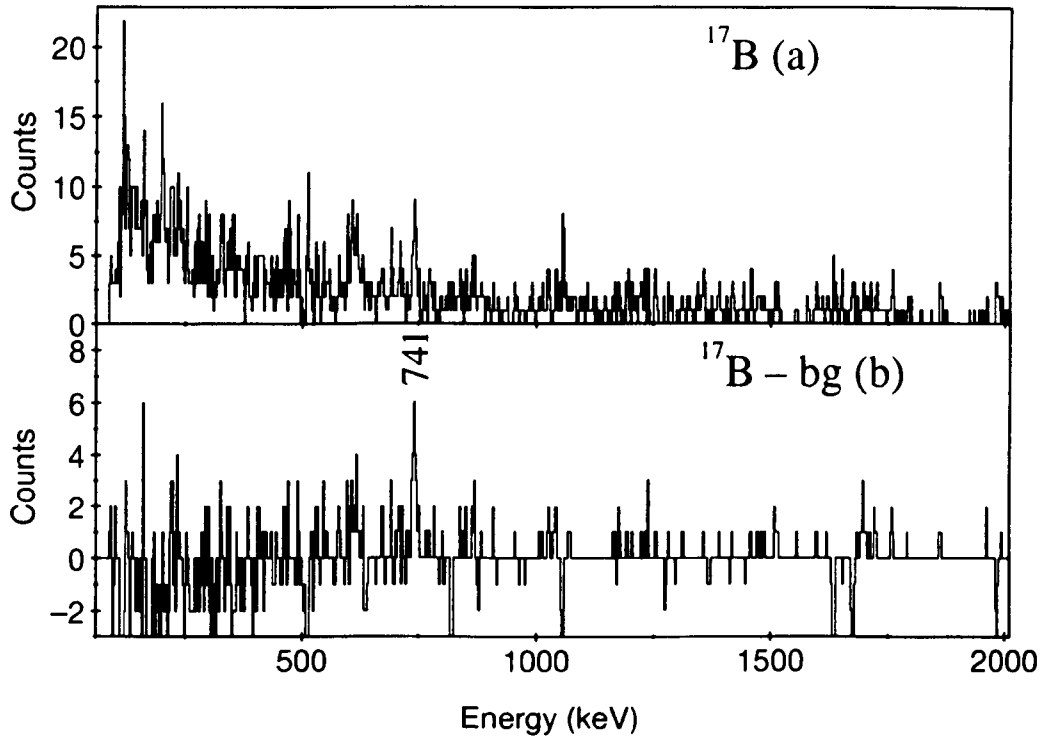
Figure 5.13: Gamma-ray spectra from the study of ^{17}B looking for β-delayed γ-events. Spectrum a shows the total number of β-delayed γ-events collected 30 ms after a ^{17}B ion is detected. Spectrum b shows the background subtracted spectrum.

could arise from bound states in ^{16}C [Bala 77] or ^{17}C, figure 5.15. Although the observation of decays from bound states in ^{16}C would not be expected as Raimann et al. account for

E_{level} (keV)	J^π	% fed Normalised to 100	% fed Normalised to P_{2n}
741.1 ± 0.6	5/2$^+$	3.6 ± 0.6	33 ± 22

Table 5.6: The feeding intensity of the state in ^{15}C via the β-2n decay channel of ^{17}B normalised to the value of Dufour et al. [Dufo 88].

FWHM vs Energy

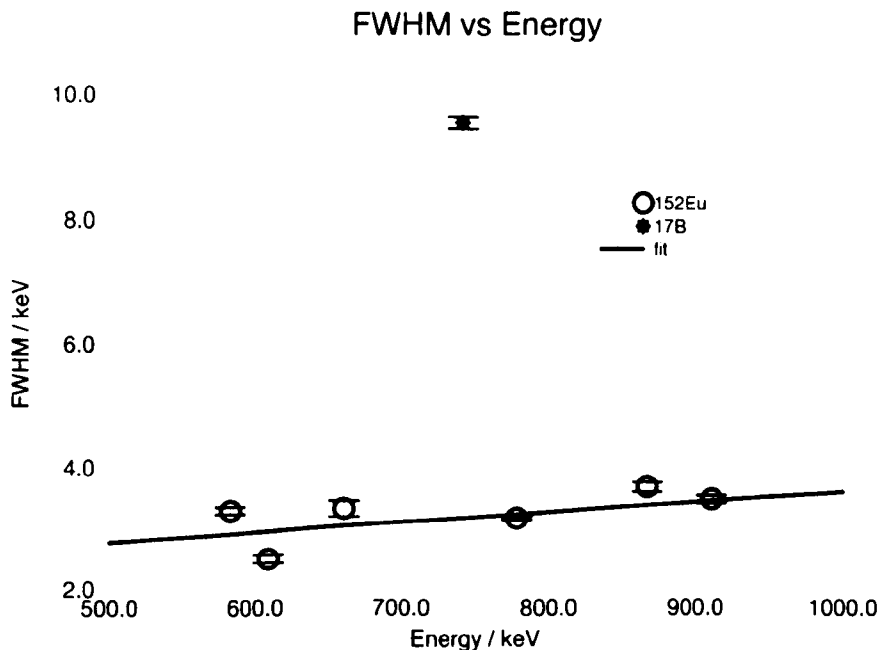Figure 5.14: A comparison of the FWHM values of the transitions of the ^{152}Eu source used for calibration and that for the 741 keV transition. The solid line represents a least squares linear fit to the ^{152}Eu data.

all the β-n decay channel feeding the ^{16}C ground state.

The three predicted bound states in ^{17}C are assigned as being of positive parity [Warb 89] whereas the ground state spin and parity of ^{17}B is predicted to be 3/2$^-$ [Desc 95]. This would, therefore, require a first forbidden β-decay transition to populate one of the bound states directly which would generally be expected to be hindered. Candidate γ rays at 224 keV and 611 keV are observed in the background subtracted spectrum which are not known to be in any of the daughter nuclei and could arise from bound states in ^{17}C. However, due to the limited statistics it is not possible to assign these as arising from bound states in ^{17}C. Assuming, therefore, that the P_{0n} channel decays to the ^{17}C ground state, a $\log_{10} ft$ value of 5.8 $\pm$ 0.5 is obtained, (see table 5.7). The deduced value appears to be consistent with an allowed transition as well as a first forbidden transition which would be consistent with the proposed spins and parities of the states involved.

Due to the limited statistics it is not possible to verify whether or not bound states of ^{17}C are populated from the β-decay of ^{17}B, although feeding, if any, would be very weak.
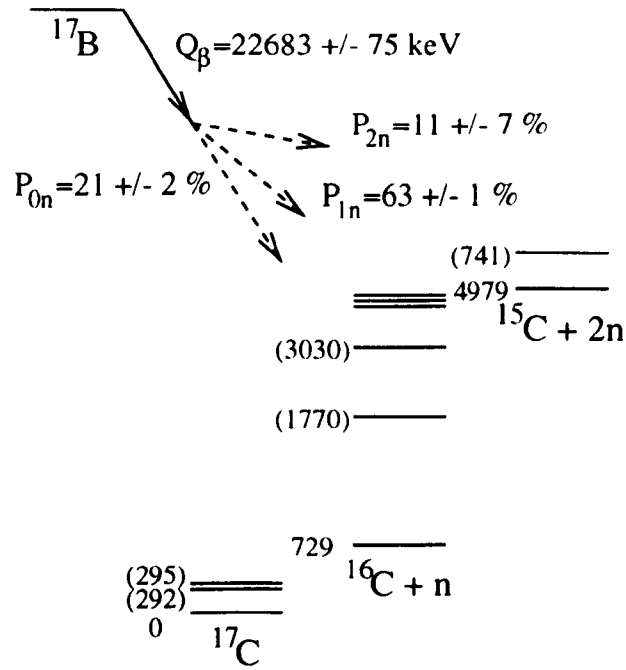
Figure 5.15: Level and decay scheme of ^{17}B. The energies of the ground states of ^{16}C and ^{15}C are shown relative to the S_{1n} and S_{2n} values for ^{17}C respectively. The bracketed values are the excitation energy values of the bound states of each of the isotopes relative to the ground state.

Raimann et al. observed unbound states in ^{17}C which if of negative parity and of possible spin values 1/2, 3/2 and 5/2 would be preferentially populated by allowed β-decay.

E_{level} (keV)	% fed	Q_β (keV)	$\log_{10} ft$
0	21 ± 2^1	22680 ± 80	5.8 ± 0.5

Table 5.7: The $\log_{10} ft$ value of the feeding of the ground state of ^{17}C from the β-decay of ^{17}B assuming no feeding of other bound states. ^{1} Value taken from [Dufo 88].

5.3.2 Half-life Calculation and Results.

The half-life of ^{17}B was measured to be 6.7 $\pm$ 0.9 ms, figure 5.16. This value is consistent with previous values of 5.08 $\pm$ 0.05 ms measured by Dufour *et al.* [Dufo 88] and 6 $\pm$ 2 ms measured by Lewitowicz *et al.* [Lewi 89]. Owing to the lower yield of this nucleus, and of
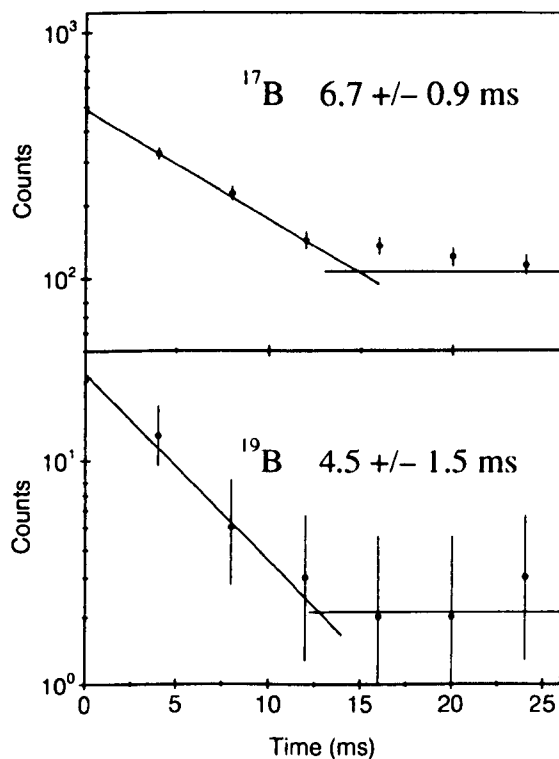

Figure 5.16: Top spectrum shows the half-life curve associated with the decay of ^{17}B, the bottom one show that corresponding to ^{19}B.

the weak γ-ray transition, no gate was set on the γ-ray spectrum but rather a maximum likelihood fit was applied to the time difference between an implant and the detection of a β-γ coincidence.

5.4 ^{19}B.

The particle stability of $^{19}_5$B$_{14}$ was confirmed by Musser and Stevenson [Muss 84] by fragmenting a 670 MeV/A beam of ^{56}Fe on a 7.9 g cm^{-2} Be target. ^{19}B is the heaviest bound isotope of boron, with ^{18}B known to be unbound and heavier isotopes predicted to be unbound [Muss 84]. No half-life or particle emission probabilities measurements have previously been performed on this nucleus.

A total yield of 337 ^{19}B nuclei were produced during the experiment at one setting of the LISE3 spectrometer with a count rate of 0.002 nuclei s^{-1}. Due to such a low yield of this nucleus it was not possible to perform any β-delayed γ-ray analysis of this nucleus and it was only possible to obtain a measurement of the half-life using the maximum likelihood method. The value obtained is 4.5 $\pm$ 1.5 ms, which is the first measurement of this value, figure 5.16.

5.5 ^{18}C.

The particle stability of $^{18}_6$C$_{12}$ was confirmed by Artukh et al. [Artu 69] by bombarding a ^{232}Th target with ^{18}O at 122 MeV. Values of the half-life and neutron emission probabilities have been measured by various authors [Muel 88, Lewi 89, Reed 91, Prav 91] and a study of the β-delayed γ-rays was undertaken by Pravikoff et al. [Prav 91].

During the present experiment a yield of 73800 ^{18}C nuclei were produced from one setting of the spectrometer which corresponded to a production rate of 1.08 nuclei s^{-1}.

5.5.1 Beta-delayed Gamma-ray Spectrum.

The β-γ coincident spectrum associated with the decay of ^{18}C 400 ms after a ^{18}C ion is detected is shown in figure 5.17a and the background subtracted spectrum is shown in figure 5.17b. The peaks that are marked are known from Pravikoff et al. to be in ^{18}N. and summarised in table 5.8, with a comparison of the values obtained by Pravikoff et al..

Various time gate durations were set for the detection of the β-γ events after the initial ^{18}C ion and the intensities of the γ rays were measured at each of these different time gates. An average value was obtained for each of the γ rays: these values are shown in table 5.8. The reason for this is the production of ^{19}C at the same setting as ^{18}C and, as will be seen
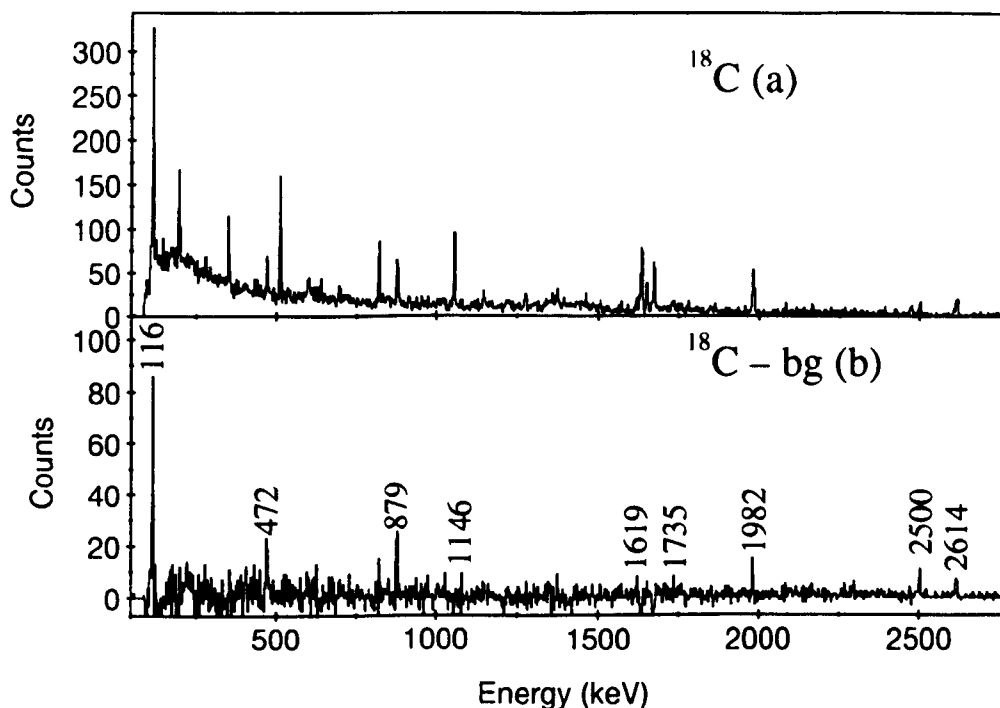
Figure 5.17: Gamma-ray spectra from the study of ^{18}C looking for β-delayed γ-events. Spectrum (a) shows the total number of β-delayed γ-events collected within 400 ms after a ^{18}C ion is detected. Spectrum (b) shows the background subtracted spectrum with the peaks marked known to be due to the decay of excited levels in ^{18}N. The contaminant peak at 1982 keV is known to be in ^{18}O [Till 95].

in section 5.6.1, ^{19}C has a relatively large P_{1n} value and populates the two lowest excited states in ^{18}N. By measuring the intensity of the γ rays as the time gate is made longer, any variation in the intensity due to γ rays from ^{19}C can be determined and corrected for.

One γ-ray observed by Pravikoff *et al.* was not observed in this experiment; the 2025.3 ± 0.8 keV transition, although a limit of the expected intensity can be deduced as being 600 ± 400 counts after correction for the β-γ detection efficiency, by using the intensity deduced by Pravikoff *et al.* Also the transition at 1734.5 ± 0.9 keV was not observed at time intervals of more than 200 ms. This transition is relatively strongly populated in the experiment performed by Pravikoff *et al.* with an intensity similar to that of the 1619 keV

E_γ (keV)	I_γ	I_γ (per 100 decays)	I_γ (relative)	I_γ (relative)[1]
116.0 ± 0.3	21300 ± 500	29 ± 1	100 ± 3	24.3 ± 0.8
471.9 ± 0.3	3450 ± 170	5.0 ± 0.5	16 ± 1	11.4 ± 1.5
879.3 ± 0.3	6590 ± 250	9.0 ± 0.5	31 ± 2	33.4 ± 3.0
1146.2 ± 0.6	2470 ± 210	3.5 ± 0.5	12 ± 1	12.9 ± 3.8
1619.0 ± 0.6	3100 ± 250	4.5 ± 0.5	15 ± 1	19.0 ± 3.8
1734.5 ± 0.9	1530 ± 310	2.0 ± 0.5	7.5 ± 1.5	19.0 ± 3.8
2025.3 ± 0.8				5.3 ± 3.8
2499.9 ± 0.6	7550 ± 490	11 ± 1	36 ± 3	31.2 ± 6.8
2614.3 ± 0.7	16200 ± 800	22 ± 1	76 ± 4	76 ± 8

Table 5.8: Energy and intensities of γ-rays observed in the β-decay of ^{18}C. [1] taken from Pravikoff et al. [Prav 91], the intensities have been corrected so that the relative value for the 2614 keV is 76 %

transition whereas in this experiment it is observed with half this intensity.

A comparison of the feeding intensities for states in ^{18}N from this experiment and Pravikoff et al. is shown in figure 5.18. The level at 2614 keV has a feeding intensity of 42 ± 2 % from this experiment which is almost half the value observed by Pravikoff. The level at 1735 keV is assigned as not being fed directly at all which is consistent with the previous measurements as is the feeding of the 587 keV level. The level at 116 keV has been assigned as being fed directly whereas previously no direct feeding was observed. Pravikoff et al. point out though that they only observe part of the flux out of the 115 keV state and have hypothesised that this level is isomeric. From the β-γ coincident time window of 12.4 μs it is possible to place an upper limit on the lifetime of this state to be this value and the lower limit to be 600 ns [Prav 91]. Such a delayed transition has been observed in the neighbouring nucleus ^{16}N [Till 93] between its first excited state ($E_x = 120$ keV, $J^\pi = 0^-$) and its ground state ($J^\pi = 2^-$) with a lifetime of 5.25 μs.

Log_{10} ft values for the levels in ^{18}N are summarised in table 5.9 and compared with those previously measured. The half-life value taken for the $\log_{10} ft$ was that measured
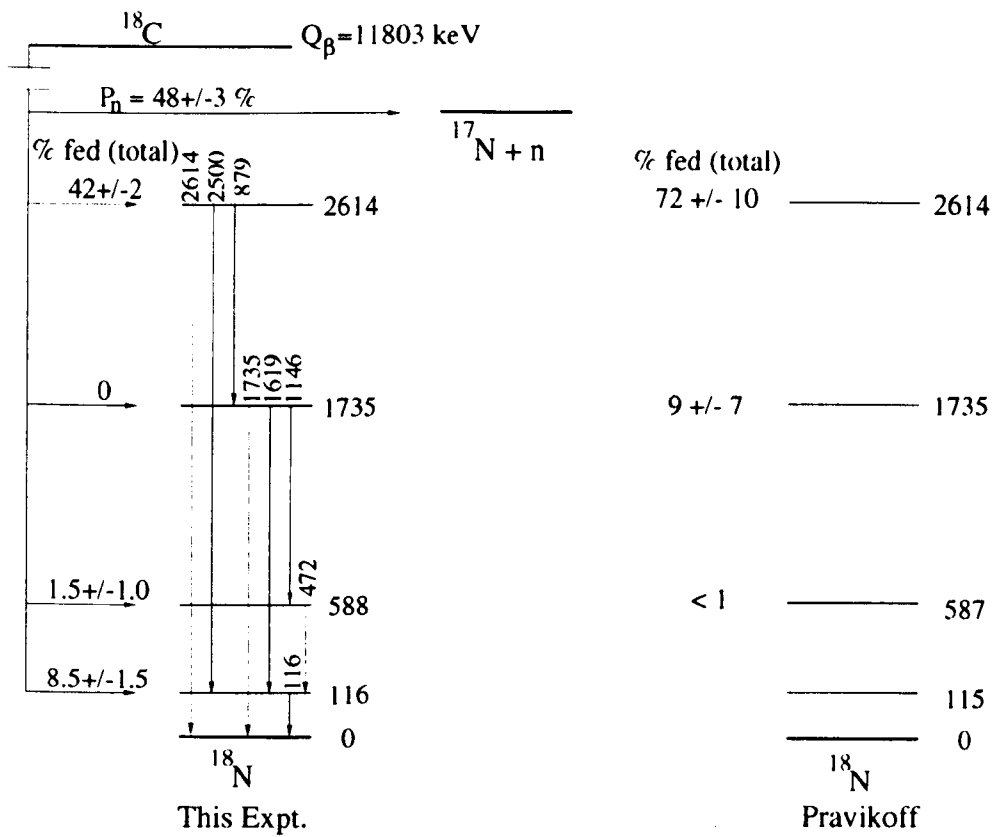
Figure 5.18: A comparison of the feeding intensities of the levels produced in ^{18}N from the β-decay of ^{18}C from this experiment (left) and from [Prav 91].

during this analysis, see section 5.5.2.

E_{level} (keV)	% fed	Q_β (keV)	$\log_{10} ft$	$\log_{10} ft$ Pravikoff et al. [Prav 91]
2614.3 ± 0.7	42 ± 2	9190 ± 40	4.33 ± 0.04	4.11 ± 0.22
1734.5 ± 0.9		10070 ± 40		5.18 ± 0.78
587.9 ± 0.4	1.5 ± 0.5	11220 ± 40	6.3 ± 0.2	≥ 6.36
116.0 ± 0.3	8.5 ± 1.5	11690 ± 40	5.48 ± 0.07	

Table 5.9: The states produced in the decay of ^{18}C to ^{18}N and their corresponding $\log_{10} ft$ values. The $\log_{10} ft$ values for the same levels that are found to be fed previously are compared with previous results.

The $\log_{10} ft$ value for the 2614 keV state is consistent with that reported by Pravikoff *et al.* [Prav 91] and would indicate that this level has a spin and parity assignment of 1^+. Calculations from Pravikoff *et al.* and Curtin *et al.* [Curt 86] based on the Millener-Kurath (MK) interaction [Mill 75] for the population of the first excited 1^+ state in ^{18}N were quoted and energies of 2614 keV and 1735 keV were obtained from calculated half-life values of 197 ms and 117 ms respectively for the ^{18}C β-decay [Prav 91]. However Pravikoff pointed out that there are difficulties reproducing the experimental features of the β-decay.

The β-decay to the 1735 keV level previously reported indicated that this level had values of J = 1 or 2 but no feeding of this state is observed in this experiment.

The $\log_{10} ft$ value of the 588 keV state is also consistent with that previously measured and would indicate a first forbidden transition. Pravikoff *et al.* tentatively predict that this state has an assignment of 2^-.

The state at 116 keV which was previously assigned as not been fed directly by β-decay has a measured $\log_{10} ft$ value of 5.48 ± 0.07 in this experiment and would indicate an allowed transition. Shell-model calculations predict a low-lying triplet of states in ^{18}N of $J^\pi = 1^-$, 2^- and 3^- [Olne 82] although with an incorrect ground state of $J^\pi = 2^-$. Direct feeding of these states would not be expected due to arising from a first forbidden decay hence it is not possible to assign a spin or parity to this state.

The ground state spin and parity of ^{18}N has been determined experimentally to be 1^- [Olne 82] and would therefore not be expected to be fed directly due to the requirement of a first forbidden transition from the 0^+ ground state of ^{18}C. From the measured γ-ray intensities a value of $P_{0n} = 52 \pm 3$ % can be obtained, assuming only γ-emitting states are populated, indicating that $P_n = 48 \pm 3$ % which is consistent with those values measured by Lewitowicz *et al.* (50 $\pm$ 10 %) [Lewi 89] and Reeder *et al.* (43.3 $\pm$ 5.5 %) [Reed 91], but inconsistent with those values measured by Mueller *et al.* (25 $\pm$ 4.5 %) [Muel 88] and Pravikoff *et al.* (19 $\pm$ 5 %) [Prav 91]. The value obtained in the latter experiment though would depend on the lifetime of the 116 keV state.

5.5.2 Half-life Calculation and Results.

The half-life of ^{18}C was found to be 95 ± 5 ms, figure 5.19. Gates were set on the 116 keV, 472 keV and 879 keV transitions and a maximum likelihood fit was applied to the data

(see section 5.2.2). This value is consistent with the measurements made by Mueller *et al.* (66 $^{+25}_{-15}$ ms), Lewitowicz *et al.* (78 $^{+20}_{-15}$ ms), Reeder *et al.* (94 ± 27 ms) and Pravikoff *et al.* (95 ± 10 ms).
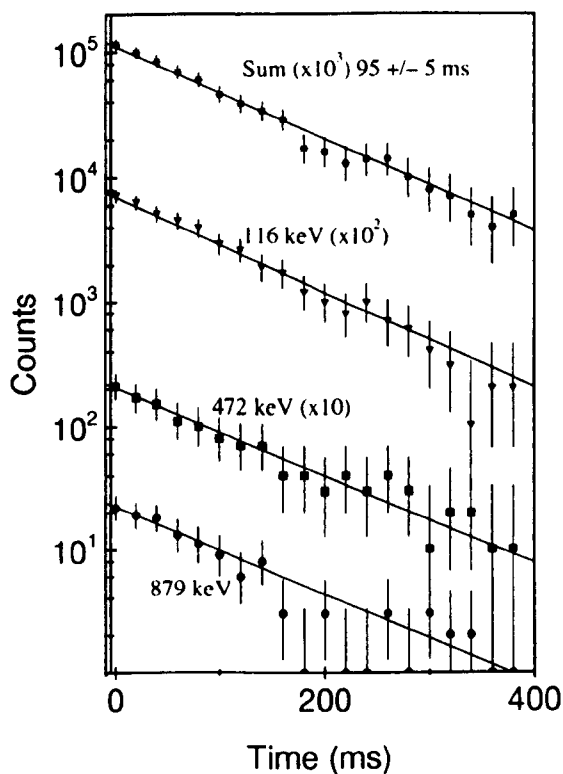
Figure 5.19: Half-life decay curves associated with the β-decay of ^{18}C. These curves were produced by setting gates on three of the known β-delayed γ rays from the decay of ^{18}C and performing a maximum likelihood fit to the curves.

5.6 ^{19}C.

$^{19}_{6}$C$_{13}$ was confirmed to be particle stable by Bowman *et al.* [Bowm 74] by impinging a 4.8 GeV proton beam on a uranium metal target. Dufour *et al.* [Dufo 88] measured the β-delayed multi-nucleon emission decay branches from the fragmentation of a ^{22}Ne beam at 60 MeV/A. They observed values of P$_{0n}$ to be 46 ± 3 %; P$_{1n}$ to be 47 ± 3 % and P$_{2n}$

to be 7 ± 3 %; the half-life was also measured to be 49 ± 4 ms. The mass excess of ^{19}C is 32830 ± 110 keV [Audi 95]. ^{19}C is then stable with respect to decay to ^{18}C + n by 161 keV and into ^{17}C + 2n by 4350 keV. Such a low S_n value led to the proposal that ^{19}C has a halo structure of a neutron orbiting a ^{18}C core, as has been observed from a breakup reaction of ^{19}C [Bazi 95].

During the experiment a total yield of 24257 ^{19}C nuclei were produced, all at one setting of the spectrometer with a production rate of 0.35 nuclei s^{-1}.

5.6.1 Beta-delayed Gamma-ray Spectrum.

Figure 5.20a shows the β-γ spectrum from the decay of ^{19}C within 200 ms after an ^{19}C ion is detected. Figure 5.20b shows the background subtracted spectrum. Two peaks are prominent which are known to be in ^{18}N, see section 5.5: these are produced via the β-n channel and are summarised in table 5.10. The width of the 116 keV line indicates some Doppler broadening with respect to the ^{152}Eu source with a measured FWHM of 3.4 ± 0.1 keV, this indicates a neutron energy of $1.5 \rightarrow 2.5$ MeV which compares favourably with the energies measured by Ozawa et al. As for ^{18}C, various time gates were used in the γ-ray analysis and an average value was obtained of the intensities.

E_γ (keV)	I_γ	I_γ (relative)	I_γ (per 100 decays)	% fed Normalised to P_{1n}
116.1 ± 0.3	9060 ± 300	100 ± 5	37 ± 2	80 ± 7
471.4 ± 0.5	1200 ± 80	13 ± 2	4.9 ± 0.7	11 ± 2

Table 5.10: Energy and intensities of γ rays observed in the β-decay of ^{19}C, the intensity is normalised to the P_{1n} value [Dufo 88].

No other γ rays are prominent, and γ rays which would be associated with the decay of excited states in ^{19}N are not observed (excited states in ^{19}N were measured by Catford et al. [Catf 89]); an experiment to study the β-delayed neutron emission of ^{19}C by Ozawa et al. [Ozaw 95] also did not observe γ-rays from excited states in ^{19}N. A compilation of the excitation scheme deduced from Ozawa et al. and Catford et al. is shown in figure 5.21. From the feeding of the bound states in ^{18}N from the β-delayed neutron emission it is only
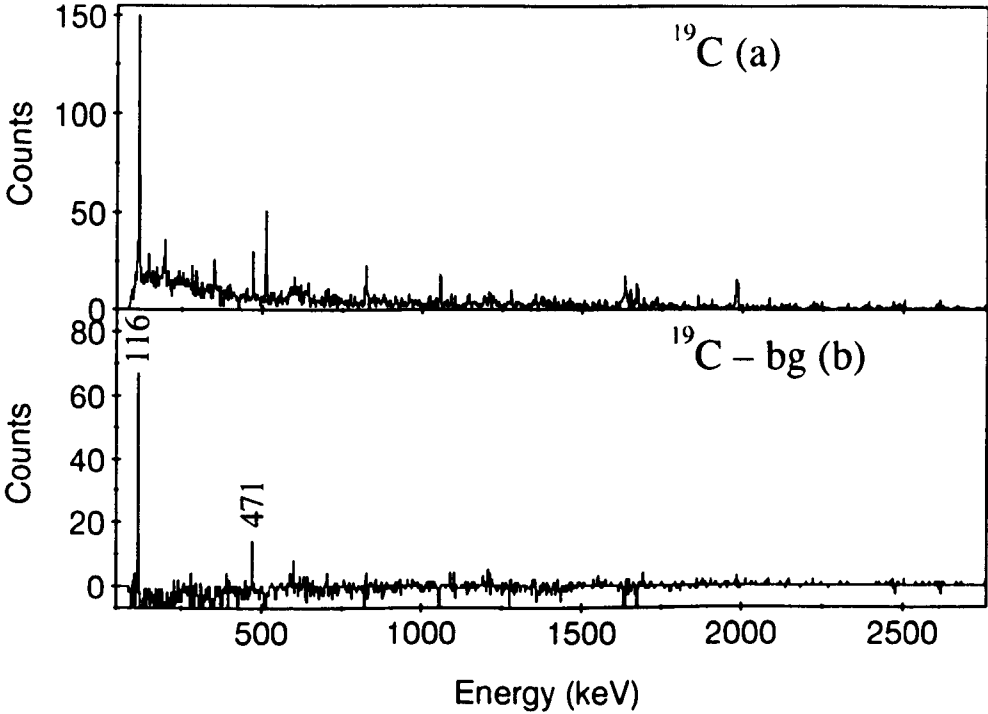
Figure 5.20: Gamma-ray spectra from the study of ^{19}C looking for β-delayed γ-events. Spectrum (a) shows the total number of β-delayed γ-events collected within 200 ms after a ^{19}C ion is detected. Spectrum (b) shows the background subtracted spectrum with the peaks marked known to be due to the decay of excited levels in ^{18}N via the β-n channel.

possible to determine the $\log_{10} ft$ value for the known 6.39 MeV state in ^{19}N which neutron decays to the 588 keV state in ^{18}N [Ozaw 95], as the 116 keV state is fed from two unbound states in ^{19}N and by the 471 keV γ-ray arising from the 588 keV state, and is summarised in table 5.11. This value is compared to that measured by Ozawa *et al.* and the half-life value used was that measured during this experiment, see section 5.6.2.

The measured $\log_{10} ft$ value would correspond to an allowed transition which is the same conclusion previously derived by Ozawa *et al.*, although the feeding of this state is not as strong as that measured previously. The total absolute feeding of the 116 keV level from the two states at 7020 keV and 6500 keV from the previous work is 32.7 $\pm$ 2.2 % which compares favourably with a value of 33 $\pm$ 2 % deduced from this work.
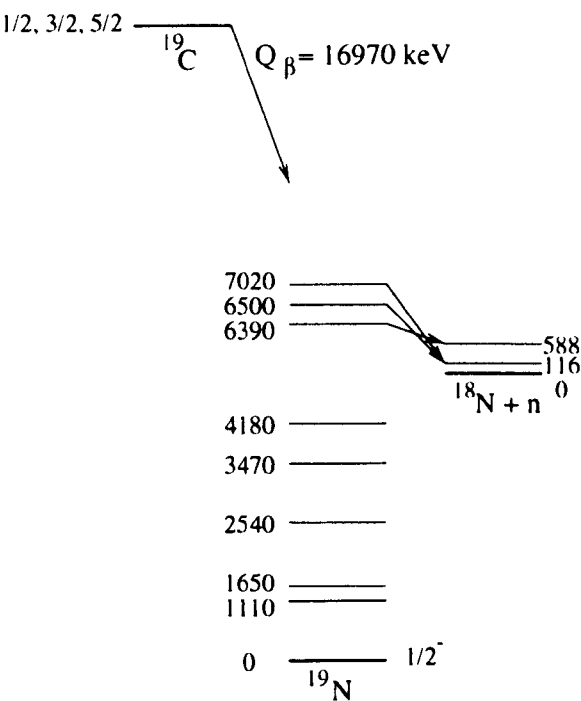
Figure 5.21: A compilation of the ^{19}N level scheme and the feeding of the bound states in ^{18}N from the β-n channel.

From shell model calculations, Ozawa *et al.* predicted the ground state spin and parity of ^{19}C to be $1/2^+$, but pointed out that the $3/2^+$ and $5/2^+$ levels are predicted to lie within 200 keV of this level and the ground state could in fact take any of these values. The state at 6.39 MeV would therefore take any spin/parity assignment of $1/2^+$, $3/2^+$, $5/2^+$ or $7/2^+$. The known bound states of ^{19}N are of negative parity [Catf 89] and the direct feeding of such states from the β-decay of ^{19}C would be expected to be hindered.

E_{level} (MeV)	% fed	Q_β (keV)	$\log_{10} ft$	$\log_{10} ft$ Ozawa [Ozaw 95]
6.39 ± 0.01	5.0 ± 0.5	10580 ± 111	5.27 ± 0.13	4.77 ± 0.13

Table 5.11: The states produced in the decay of ^{19}C to ^{19}N and their corresponding $\log_{10} ft$ values. The energy of the excited state are taken from [Ozaw 95] but with the feeding intensities deduced from this experiment.

5.6.2 Half-life Calculation and Results.

The half-life of ^{19}C was found to be 49 ± 6 ms, figure 5.22. A gate was set on the 116 keV transition and a maximum likelihood fit was applied to the data (see section 5.2.2). This value is consistent with the measurement made by Dufour *et al.* [Dufo 88].
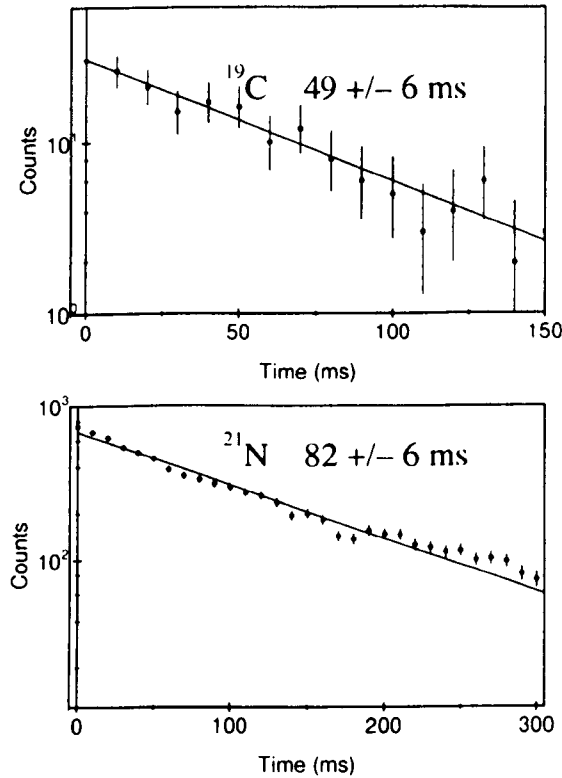
Figure 5.22: Top spectrum shows the half-life curve associated with the decay of ^{19}C, the bottom one shows that corresponding to ^{21}N.

5.7 ^{20}N.

By impinging an ^{18}O beam at 122 MeV onto a 5 mg cm^{-2} thick ^{232}Th target Artukh *et al.* [Artu 69] demonstrated the particle stability of $^{20}_{7}$N$_{13}$. Half-life and neutron emission probabilities measurements have been performed by Mueller *et al.* [Muel 88] and Reeder *et*

al. [Reed 91].

A yield of 25655 ^{20}N nuclei were produced during the experiment at only one setting which resulted in an implantation rate of 0.38 nuclei s^{-1}.

5.7.1 Beta-delayed Gamma-ray Spectrum.

The β-delayed γ-ray spectrum observed 400 ms after the detection of a ^{20}N ion is shown in figure 5.23a, with the resultant background subtracted spectrum in figure 5.23b. One peak is marked in figure 5.23b - the 96 keV transition is known to be in ^{19}O [Ajze 87]. figure 5.24.
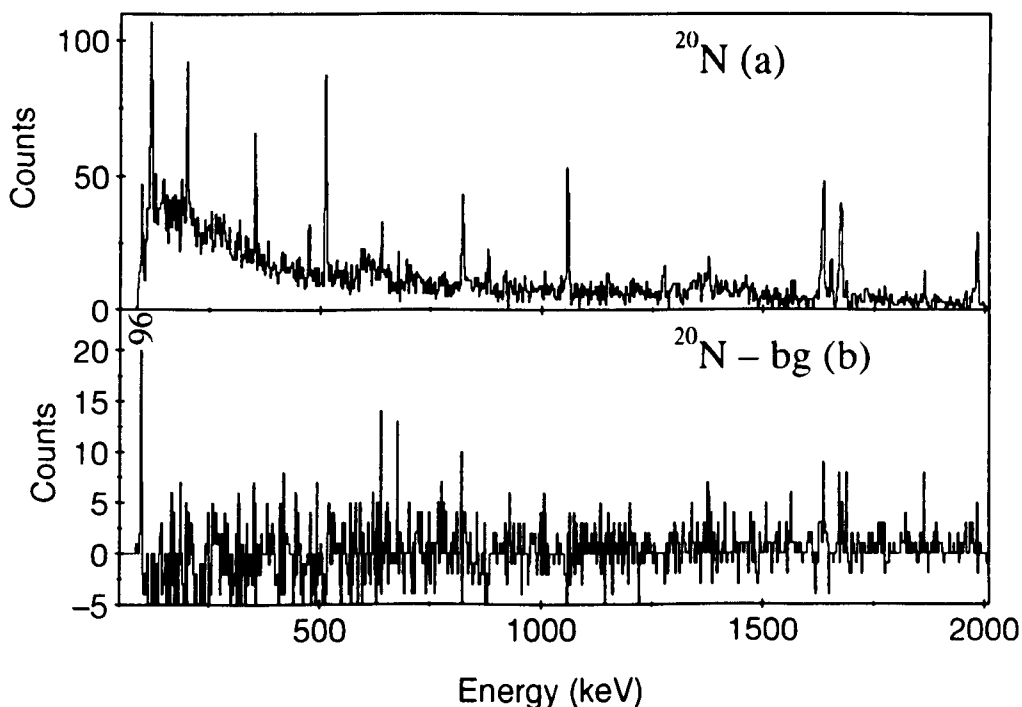
Figure 5.23: Gamma-ray spectra from the study of ^{20}N looking for β-delayed γ-events. Spectrum (a) shows the total number of β-delayed γ-events collected within 400 ms after a ^{20}N ion is detected. One peak is marked in spectrum (b) which is still prominent after background subtraction.

As was previously mentioned the low energy thresholds of the γ-ray detectors indicate that the 96 keV transition can only be measured by one of the detectors. This reduced
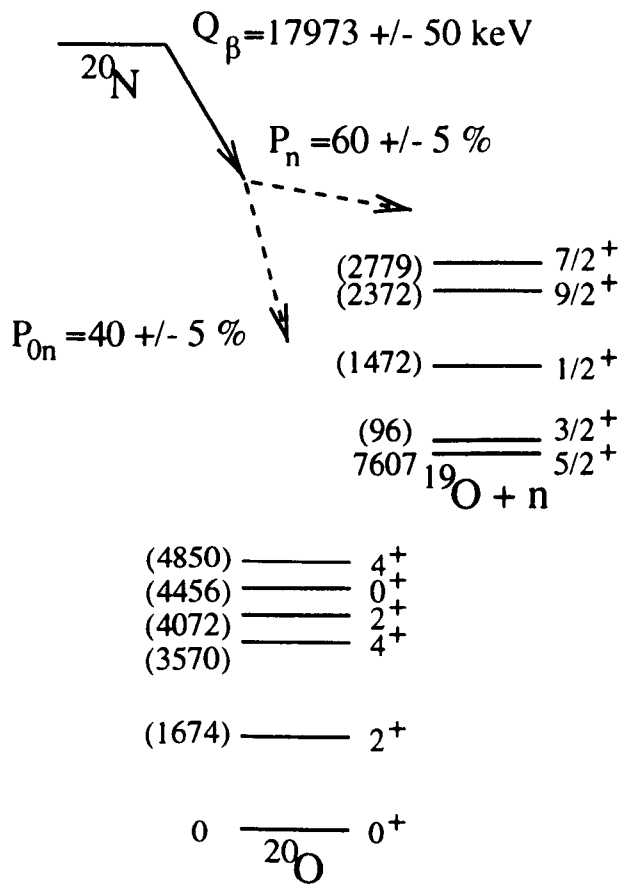
Figure 5.24: Level and decay scheme of ^{20}N. The energy of the ground state of ^{19}O is shown relative to the S_{1n} value for ^{20}O. The bracketed values are the excitation energy values of the bound states of each of the isotopes relative to the ground state.

efficiency has been used when calculating the intensity of the γ ray and is summarised in table 5.12. The intensity of the γ ray and the non-observation of any other γ ray in the spectrum leads to the proposal that the β-n decay channel populates the lowest two states of ^{19}O with equal intensity, table 5.13. The FWHM of the 96 keV transition was slightly

E_γ (keV)	I_γ	I_γ (per 100 decays)
96.4 ± 0.4	7750 ± 1220	30 ± 5

Table 5.12: Energy and intensity of γ-ray observed in the β-decay of ^{20}N.

E_{level} (keV)	J^π	% fed Normalised to 100	% fed Normalised to P_n
96.4 ± 0.4	$3/2^+$	30 ± 5	51 ± 9
0	$5/2^+$	29 ± 5	49 ± 9

Table 5.13: The feeding intensities of the states in ^{19}O via the β-n decay channel of ^{20}N. The P_n value taken was a weighted average of the previous measurements which is 60 ± 5 %.

broadened compared with the ^{152}Eu source data although due to the resolution of the one germanium detector that could detect this transition this is a tentative assignment of the Doppler broadening.

There is no evidence of direct population of known excited states in ^{20}O [Ajze 87], and from shell model considerations, the ground state of ^{20}N would be either 2 or 3 and would not favourably populate the known states in ^{20}O.

5.8 ^{21}N.

The particle stability of $^{21}_7$N$_{14}$ was confirmed by Artukh et al. [Artu 70b] by bombarding a ^{232}Th target with a ^{22}Ne beam at 174 MeV. Half-life and neutron emission probabilities measurements have been performed by Mueller et al. [Muel 88] and Reeder et al. [Reed 91].

A total yield of 86735 ^{21}N nuclei were produced during the experiment at two different settings of the spectrometer as shown in table 5.14.

LISE3 Setting	Yield	Rate s^{-1}
^{26}F	5186	0.06
^{17}B	81549	1.19
Total	86735	

Table 5.14: The LISE3 settings and the yield of ^{21}N produced at each setting with the implantation rate.

5.8.1 Beta-delayed Gamma-ray Spectrum.

The β-delayed γ-ray spectrum produced for the the decay of ^{21}N is shown in figure 5.25a, with the condition that only γ rays emitted within 300 ms of the detection of a ^{21}N ion are
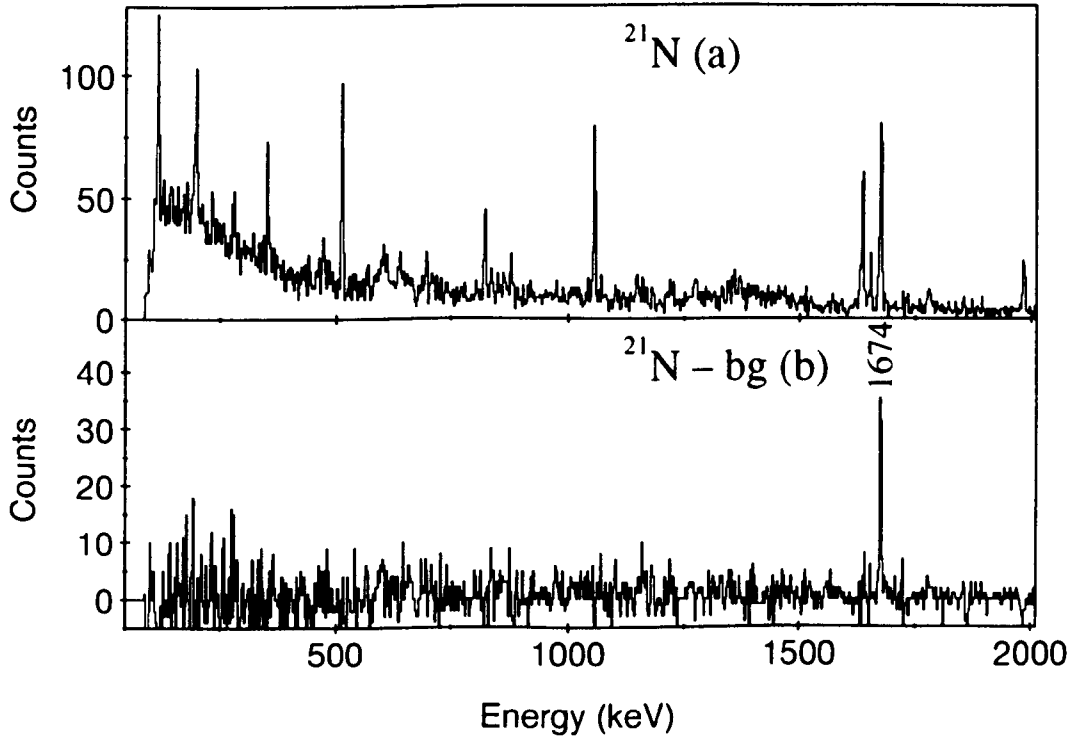
Figure 5.25: Gamma-ray spectra from the study of ^{21}N looking for β-delayed γ-events. Spectrum (a) shows the total number of β-delayed γ-events collected within 300 ms after a ^{20}N ion is detected. One peak is marked in spectrum (b) which is prominent after background subtraction.

incremented. The resultant background-subtracted spectrum is shown in figure 5.25b. The peak marked at 1674 keV (table 5.15) is known to be in ^{20}O [Ajze 87] which is populated via the β-n decay channel which has a weighted average probability of 80 $\pm$ 8 %, and the feeding of the excited and the assumed feeding of the ground state is summarised in table 5.16. No γ rays arising from excited states in ^{21}O [Catf 89] are observed in the spectrum.

The parities of the bound states of ^{21}O are predicted to be all positive [Catf 89] and
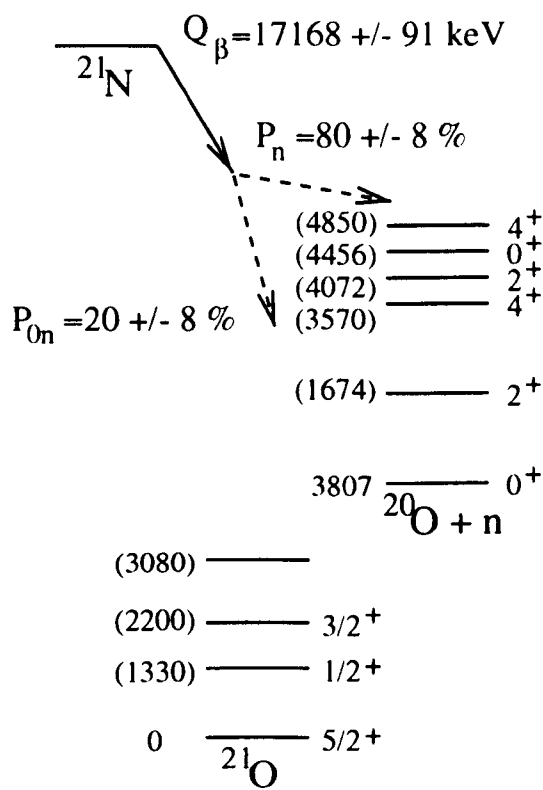
Figure 5.26: Level and decay scheme of ^{21}N. The energy of the ground state of ^{20}O is shown relative to the S_{1n} value for ^{21}O. The bracketed values are the excitation energy values of the bound states of each of the isotopes relative to the ground state.

the β-decay to these states would thus be expected to be hindered. This would explain the high P_n value of ^{21}N as there could be high lying negative parity states which would be preferentially populated.

E_γ (keV)	I_γ	I_γ (per 100 decays)
1673.5 ± 0.3	25860 ± 1180	30 ± 1

Table 5.15: Energy and intensities of the γ-ray observed in the β-decay of ^{21}N.

E_{level} (keV)	J^π	% fed Normalised to 100	% fed Normalised to P_n
1673.5 ± 0.3	2^+	30 ± 1	37 ± 4
0	0^+	70 ± 7	63 ± 7

Table 5.16: The feeding intensities of the states in ^{20}O via the β-n decay channel of ^{21}N normalised to the average P_n value.

5.8.2 Half-life Calculation and Results.

The half-life of ^{21}N was determined to be 82 ± 6 ms, figure 5.22. A gate was placed on the 1674 keV transition and a maximum likelihood fit was applied to the data. This value is consistent with the measurement preformed by Mueller *et al.* [Muel 90] (95 $^{+15}_{-11}$ ms) but not consistent with that performed by Reeder *et al.* [Reed 91] (61 ± 3 ms).

5.9 ^{24}O.

$^{24}_{8}$O$_{16}$ is the heaviest bound isotope of oxygen observed [Tara 97a]. In an earlier experiment using the LISE3 spectrometer with a 44 MeV/A ^{48}Ca beam, Mueller *et al.* [Muel 90] measured the half-life of ^{24}O to be 61^{+32}_{-19} ms and the P_n value to be 58 ± 12 %. This present work represents the first β-γ study of this nucleus and in the parallel analysis of the data the P_n value was measured as 11 ± 4 % [Tara 97b].

During the present experiment a total of 9354 ^{24}O nuclei were produced at three separate settings as shown in table 5.17.

5.9.1 Beta-delayed Gamma-ray Spectrum.

Figure 5.27a shows all the β-delayed γ rays collected 200 ms after an ^{24}O ion is detected. Figure 5.27b shows the background subtracted spectrum. Four peaks are labelled but the 1982 keV peak is assigned as the known $2^+ \rightarrow 0^+$ transition energy in ^{24}Ne from the β-decay of ^{24}F ($t_{1/2} = 340 \pm 80$ ms [Dufo 86]). The energies and intensities of these transitions are summarised in table 5.18. The previous measurement of the P_n value of ^{24}O raises the question of whether the three identified γ rays are emitted from levels in ^{24}F or from ^{23}F

LISE3 Setting	Yield	Rate s^{-1}
^{26}F	7189	0.08
^{17}B	604	0.009
^{19}B	1561	0.009
Total	9354	

Table 5.17: The LISE3 settings and the yield of ^{24}O produced at those settings with the implantation rate.

E_γ (keV)	I_γ	I_γ (relative)	I_γ (per 100 decays)
521.5 ± 0.3	1350 ± 190	51 ± 9	15 ± 2
1309.5 ± 0.5	1130 ± 250	42.0 ± 11	12 ± 3
1831.6 ± 0.5	2700 ± 300	100 ± 11	29 ± 3

Table 5.18: Energy and intensities of γ rays observed in the β-decay of ^{24}O to ^{24}F.

after neutron emission. The energy level spectrum of ^{23}F was previously studied by Orr et $al.$ [Orr 89] and a comparison of the γ rays with these known levels indicates no correspondence between the two. This conclusion is also supported by the lower P_n value measured in the parallel analysis.

The 1982 keV transition is the only observed γ ray from the β-decay of ^{24}F with 100 % emission probability. By using a long time gate after the detection of an ^{24}O ion it is possible to measure the P_{0n} channel of ^{24}O via the decay of its daughter nucleus. From Krane [Kran 88] the production and decay of a daughter nucleus can be calculated by

$$\frac{dN_2}{dt} = \frac{N_0\lambda_1\lambda_2}{\lambda_2 - \lambda_1}P_{0n}\left(e^{-\lambda_1 t} - P_d e^{-\lambda_2 t}\right), \tag{5.1}$$

where dN_2/dt is the rate of decay of the daughter nucleus, N_0 is the number of parent nuclei at $t = 0$, λ_1 and λ_2 are the decay constants of the parent and daughter nuclei respectively, P_{0n} is the percentage of parent nuclei decaying via the β-γ channel and P_d is the percentage of daughter nuclei decaying via the β-γ channel which in this instance is 100 %. Integrating
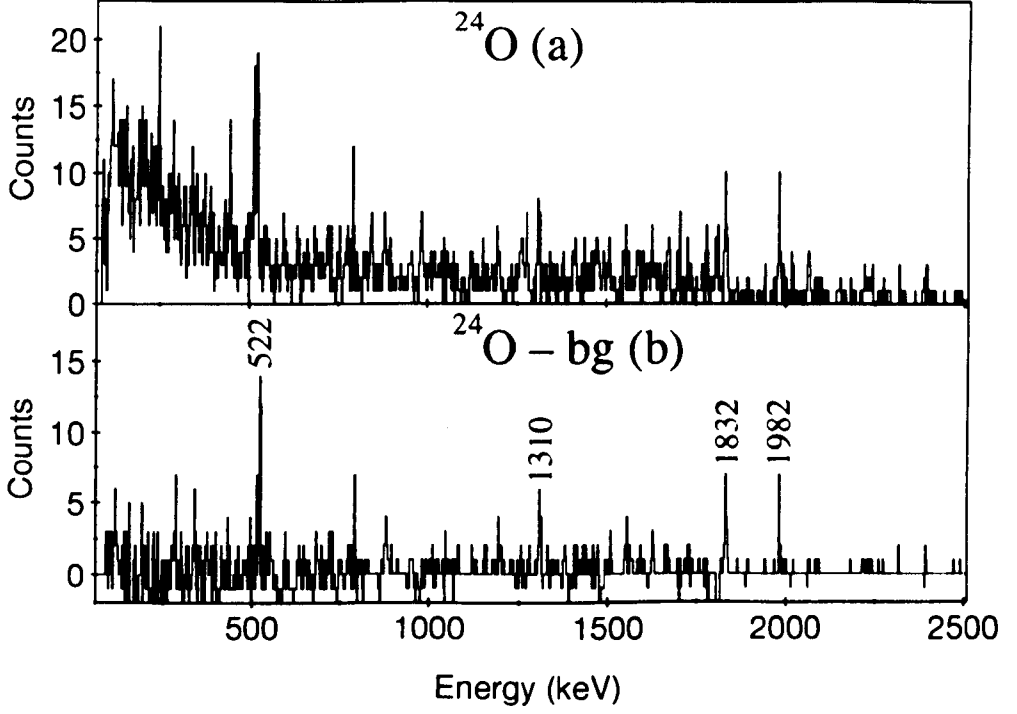
Figure 5.27: Gamma-ray spectra from the study of ^{24}O looking for β-delayed γ-events. Spectrum (a) shows the total number of β-delayed γ-events collected within 200 ms after a ^{24}O ion is detected; three peaks are marked on which are still visible after background subtraction (b). Also marked on is the 1982 keV γ-ray, observed from the β-decay of ^{24}F to ^{24}Ne.

this equation over the time range gives the expected number of the daughter nuclei having decayed in this time. Only ^{24}O ions produced during the ^{26}F setting are analysed this way.

The 1982 keV γ-ray background can be accounted for by considering:

• The random rate of 1982 keV events which can be calculated by using the equation:

$$I_{random} = \frac{I_\gamma \times t \times N_1}{t_0},\tag{5.2}$$

where I_{random} is the random rate in the time difference used (t). I_γ is the total number of the 1982 keV γ-rays produced in the ^{26}F setting, N_1 is the total number of ^{24}O ions produced at the ^{26}F setting and t_0 is the length of time of the ^{26}F setting.

- from ^{24}F ions. There was a yield of 1985 ^{24}F ions detected during the ^{26}F setting at an implantation rate of 0.02 s^{-1}, and it is necessary to account for the possibility of a ^{24}F decay using

$$I_{24_F} = \frac{N_1 \times N_F \times t}{t_0}.$$

(5.3)

where N_F is the number of ^{24}F ions detected during the ^{26}F setting.

Different time gates were set and the expected intensity of the 1982 keV γ-ray in the time range used was calculated as were the background rates. From the measured intensity of the 1982 keV, I_γ^{1982}, the P_{0n} value could be determined using equation 5.1 and the equation:

$$\left(I_\gamma^{1982} - I_{random} - I_{24_F}\right) = \frac{dN_2}{dt}.$$

(5.4)

An average of the P_{0n} value was determined as 76 $\pm$ 8 %, implying the P_n value to be 24 $\pm$ 8 % which is consistent with that obtained by Mueller et al. and from the parallel analysis of the data set.

5.9.2 Half-life Calculation and Results.

The half-life of ^{24}O was found to be 65 $\pm$ 5 ms, figure 5.28. The value obtained is consistent with that measured by Mueller et al. [Muel 90]. Gates were set on the 522 keV, 1310 keV and 1832 keV transitions and a maximum likelihood fit applied.

5.9.3 Comparisons with Single Particle Shell Model Calculations.

Shell model calculations have been performed by Suhonen [Suho 98] using the shell model code OXBASH [Brow 86] using three different interactions proposed for sd shell nuclei [Wild 84, Brow 88, Chun 76] to determine the energy spectrum of excited states in ^{24}F. The results of the calculations are shown in figure 5.29 and it is evident that all three interactions predict the same sequence of lowest lying states although the precise energies differ.

A possible partial level scheme for ^{24}F is shown in figure 5.29d for the γ rays identified in figure 5.27. The level scheme in figure 5.29d is derived from the fact that the two lowest energy γ rays sum up to the exact energy of the third strongly suggesting that the two γ rays are in a cascade from the same state as the higher energy γ ray. In this level
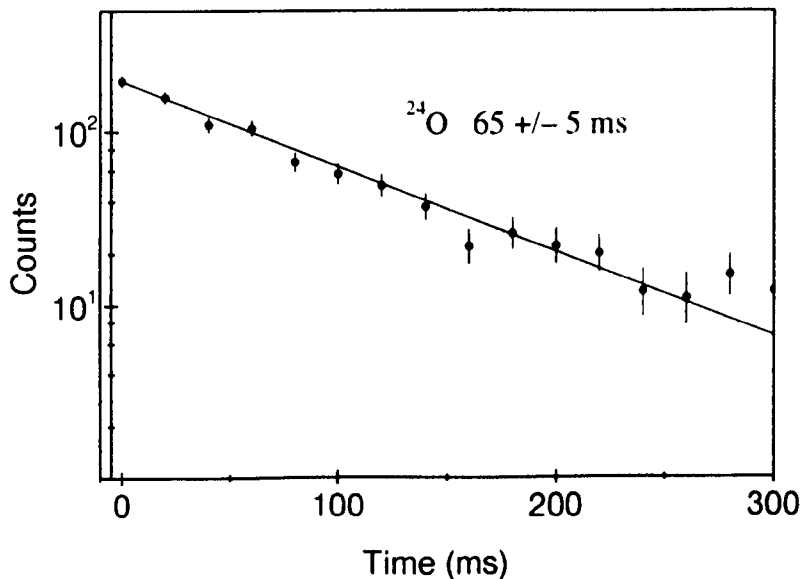
Figure 5.28: Half-life decay curve associated with the β-decay of ^{24}O.

scheme a 1^+ level at 1832 keV is fed directly in the β-decay of ^{24}O and γ-decays directly to the 3^+ ground state and to a state at 522 keV. The ordering of the 1320 keV and 522 keV transitions are tentative but it does provide better agreement with the shell model calculations. The level at 522 keV would not be expected to be fed due to spin restrictions and the experimental deduced feeding is consistent with this. The feeding of the 1832 keV state and the corresponding $\log_{10} ft$ value is given in table 5.19. The value of 4.3 for the

E_{level} (keV)	J^{π}	% fed	Q_{β} (keV)	$\log_{10} ft$
1831.6 ± 0.5	1^+	41 ± 4	9600 ± 300	4.3 ± 0.1

Table 5.19: The state fed in the decay of ^{24}O to ^{24}F and the corresponding $\log_{10} ft$ value.

$\log_{10} ft$ value is consistent with an allowed transition indicating a 1^+ assignment for the fed state.

Combining the observed β-decay strength with the average of the measured P_n values implies that 41 % of the total β-decay of ^{24}O is not accounted for. The shell model level
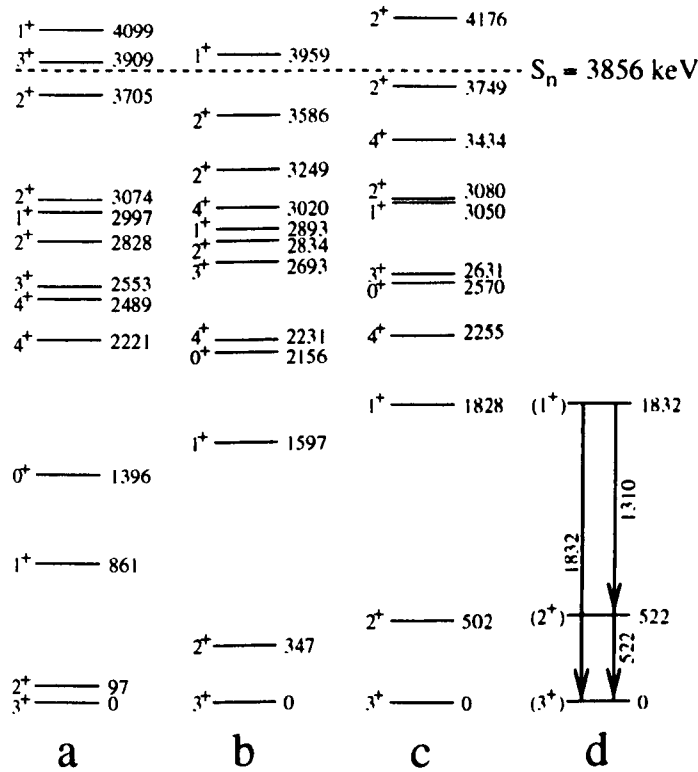
Figure 5.29: Energy levels of ^{24}F up to $\sim$4 MeV calculated using the shell model code OXBASH [Brow 86] with a) the USD interaction [Wild 84]; b) the SDPOTA interaction [Brow 88] and c) the interaction of Chung and Wildenthal [Chun 76], compared with the tentative partial decay scheme deduced in the present work. The energies of the levels are given in keV and the tentative spin and parity assignments for the deduced levels are in parentheses. The S_n value [Audi 95] is indicted by the dashed line.

schemes of figure 5.29 suggests that there is another 1^+ level that could be expected below the S_n level (3900 $\pm$ 100 keV [Audi 95]). If this level was to be populated directly then the efficiency of detecting γ rays from the decay of this state to the ground state would be very low (0.2-0.4 %). There is weak evidence in the ^{24}O spectrum of other γ rays but due to the weakness of their intensities it was not possible to place them as arising from excited states in ^{24}F.

5.10 ^{25}F.

Values of the half-life and neutron emission probability for $^{25}_{9}$F$_{16}$ were previously measured to be 59 ± 40 ms and 15 ± 10% respectively in an experiment performed by Reeder *et al.* [Reed 91] impinging 800 MeV protons on ^{232}Th and using the TOFI (Time Of Flight Isochronous) spectrometer [Viei 86] to separate out the nuclei. In the parallel analysis of the data a value of 14 ± 5 % was measured for the P_n value [Tara 97b].

The first experimental study of ^{25}Ne by Wilcox *et al.* [Wilc 73] was performed by using the reaction ^{26}Mg(^{7}Li,^{8}B)^{25}Ne with a beam energy of 79 MeV. This experiment suffered from poor statistics, although they observed possible excited states at 1.65 ± 0.05 MeV, 2.03 ± 0.05 MeV, 3.25 ± 0.08 MeV, 4.05 ± 0.08 MeV and 4.7 ± 0.1 MeV (figure 5.30). A second experiment performed by Woods *et al.* [Wood 85] with a ^{13}C beam at 96 MeV on a ^{26}Mg target provided more information on the level scheme and a value of the one-neutron separation energy was obtained as being 4.13 MeV. The deduced level schemes from the two experiments are shown in figure 5.30. The measured widths of the 1.74 MeV and 3.33 MeV peaks were 255 ± 21 keV and 305 ± 44 keV respectively, Woods concluded that the shapes of these peaks suggested that they are unresolved doublets, and that the peaks at 1.74 MeV are separated by 110 ± 100 keV and those at 3.33 MeV by 200 ± 100 keV.

During the present experiment a total of 38691 ^{25}F nuclei were identified and these were distributed among the runs as shown in table 5.20.

LISE3 Setting	Yield	Rate s^{-1}
^{26}F	37669	0.44
^{17}B	1022	0.02
Total	38691	

Table 5.20: The LISE3 settings and the yield of ^{25}F nuclei produced at each setting with the corresponding implantation rate.
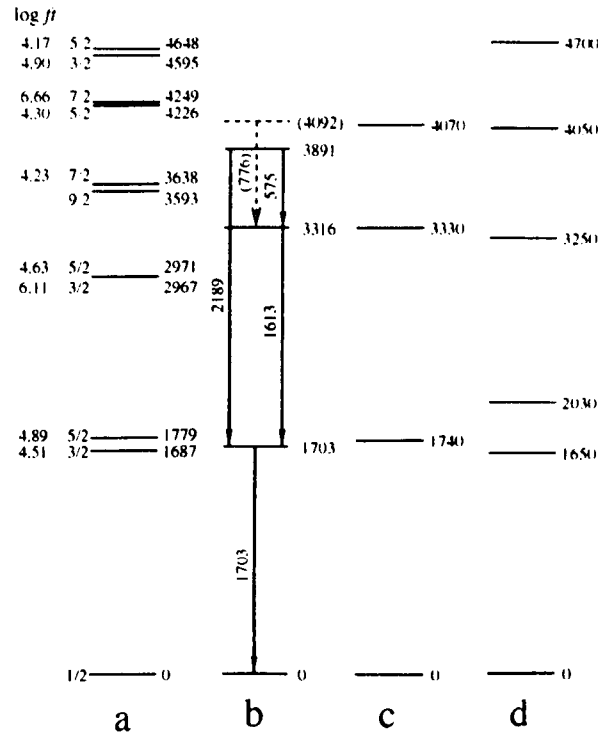
Figure 5.30: Comparison of a) shell model calculations with the USD interaction [Wild 84]. including calculated $\log_{10} ft$ values; b) the partial level scheme deduced in the present work; c) the energy levels identified by Woods *et al.* [Wood 85]; and d) the energy levels identified by Wilcox *et al.* [Wilc 73]. The dashed lines and values in parentheses indicate tentative levels and transitions. The excitation energies of the levels and γ-ray transition energies are given to the nearest keV. See text for explanation of the widths of the levels measured in the transfer reactions.

5.10.1 Beta-delayed Gamma-ray Spectrum.

Figure 5.31a shows all the β-delayed γ rays collected 200 ms after a ^{25}F ion is detected and figure 5.31b shows the same spectrum after a normalised fraction of the γ-ray background is removed. Four peaks have been labelled in addition to the 1982 keV $2^+ \rightarrow 0^+$ transition in ^{24}Ne from the β-decay of ^{24}F populated in this case via the P_{1n} decay channel. The 1982 keV γ-ray line in this spectrum is significantly broader than other lines in this region (9 ± 1 keV FWHM compared with 4 $\pm$ 1 keV FWHM), which is compatible with the Doppler broadening expected for γ-rays emitted following the emission of a neutron with an energy of around 1.4 MeV. From measuring the intensity of the 1982 keV γ-ray and correcting
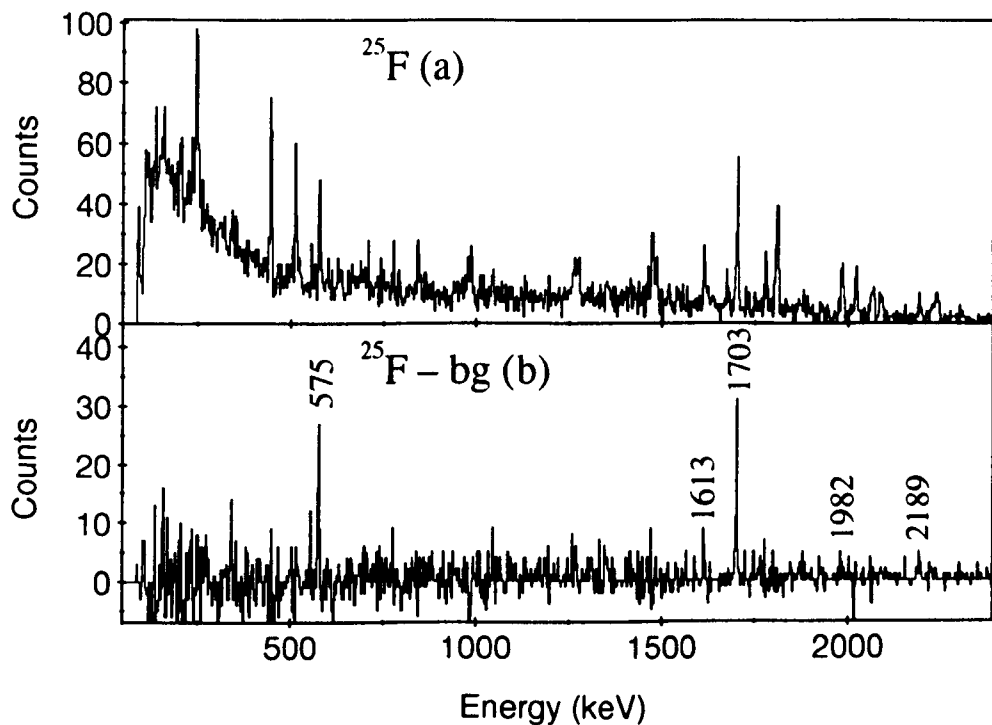
Figure 5.31: Gamma-ray spectra from the study of ^{25}F looking for β-delayed γ-events. Spectrum (a) shows the total number of β-delayed γ events collected within 200 ms after a ^{25}F ion is detected. Five peaks are marked which are still visible after background subtraction (b).

for the random background component a value of $P_{1n} = 11 \pm 3$ % can be obtained. This value is consistent with that measured by Reeder *et al.* and in the parallel analysis of the data [Tara 97b]. The value measured by γ-ray emission can therefore be regarded as a lower limit of the P_n value. None of these γ-ray energies correspond to transitions in the grand-daughter nucleus ^{25}Na, so they are attributed to γ-rays emitted from levels in ^{25}Ne which are populated in the β-decay of ^{25}F. The energies and relative intensities of these lines are summarised in table 5.21.

E_γ (keV)	I_γ	I_γ (relative)	I_γ (per 100 decays)
574.7 ± 0.5	3580 ± 340	24 ± 3	9.5 ± 0.9
1613.4 ± 1.2	4390 ± 670	30 ± 5	12 ± 2
1702.7 ± 0.7	14700 ± 1000	100 ± 7	39 ± 3
2188.6 ± 1.3	2720 ± 610	19 ± 5	7.2 ± 1.6

Table 5.21: Energy and intensities of γ-rays observed in the β-decay of ^{25}F.

5.10.2 Half-life Calculation and Results.

Gates were set on the 1703 keV, 1613 keV and 575 keV γ-rays and the decay spectra were fitted using the method of maximum likelihood.

The value obtained was: $T_{1/2} = 50 \pm 6$ ms, figure 5.32, which is consistent with the previous measurement [Reed 91].

5.10.3 Comparisons with Single Particle Shell Model Calculations.

The level scheme deduced for ^{25}Ne from the experimental results and the shell model calculations performed by Suhonen [Suho 98] using the USD interaction [Wild 84] are shown in figure 5.30 along with the results from the previous experiments. The ground state of ^{25}F is predicted to have a spin and parity of $5/2^+$ and that of ^{25}Ne to have $1/2^+$, so β-decays from ground state to ground state could not proceed by an allowed transition.

The lowest identified level from the results of Woods et al. has been interpreted as being a doublet separated by 100 keV at 1.7 MeV which is entirely consistent with the shell model calculations and both are predicted to be populated directly by allowed β-decays. Woods et al. argue that, from reaction mechanism considerations and calculated spectroscopic factors, the peak observed at 1.74 MeV was most probably the $3/2^+$ level predicted at 1687 keV. The calculated $\log_{10} ft$ value for this state predicts that this level should be populated more strongly in the β-decay than the predicted 1779 keV $5/2^+$ level suggesting that the 1703 keV γ-ray observed in this work arises from the $3/2^+$ level as it decays to the ground state; the energy of this level would be consistent with those observed in both
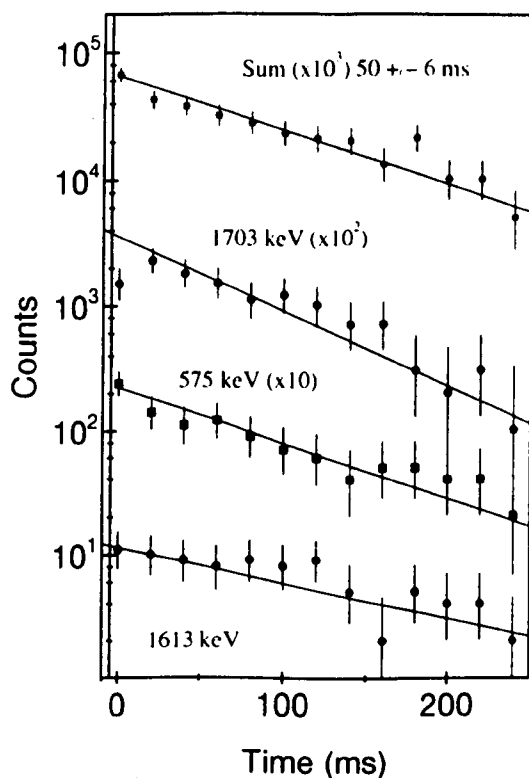
Figure 5.32: Half-life decay curves associated with the β-decay of ^{25}F. These curves were produced by setting gates on three of the β-delayed γ-rays from the decay of ^{25}F and performing a maximum likelihood fit to the curves.

transfer reaction studies. The determined $\log_{10} ft$ value for this level is consistent with an allowed transition for the β-decay to this state (see table 5.22).

The 1613 keV γ-ray transition has been assigned as feeding the 1703 keV state arising from a level at 3316 keV. In principle this γ ray could also represent the decay of the second level predicted near 1.7 MeV to the ground state of ^{25}Ne. However, the 1613 keV and 575 keV transitions sum to 2188 keV, suggesting that these three γ rays form two different decay paths between common states. No states are predicted near 2.2 MeV by the shell model calculations. The energy of the level at 3316 keV would be entirely consistent with the energies observed in the transfer measurements. The calculated $\log_{10} ft$ values indicate

E_{level} (keV)	% fed	Q_β (MeV)	$\log_{10} ft$
3890.8 ± 1.5	17 ± 2	9440 ± 90	4.54 ± 0.11
3316.1 ± 1.4	2.5 ± 2.0	10010 ± 90	5.6 ± 1.2
1702.7 ± 0.7	21 ± 4	11630 ± 90	4.92 ± 0.13
0	46 ± 9	13330 ± 90	4.86 ± 0.13

Table 5.22: The states produced in the decay of ^{25}F to ^{25}Ne and their corresponding $\log_{10} ft$ values.

that the $5/2^+$ level at 2971 keV would be more strongly populated in the β-decay of ^{25}F than the $3/2^+$ level predicted at 2967 keV. Woods et al. argue that the level they observe is more likely to correspond to the $3/2^+$ level than the $5/2^+$ level.

The 575 keV γ ray has been assigned to feed the 3316 keV state from a level at an excitation energy of 3891 keV which would be inconsistent with the energy of 4.07 ± 0.03 MeV measured by Woods et al.. The shell model predicts a $7/2^+$ level at 3638 keV to be strongly populated in the β-decay as would the $5/2^+$ level at 4226 keV although this latter level would lie above the neutron emission threshold of 4183 ± 46 keV [Audi 95]. The 2188 keV γ ray would fit with this sequence as representing the decay of the 3891 keV level directly to the 1703 keV level. The level energies and feeding intensities are summarised in table 5.22 along with the $\log_{10} ft$ values which are all consistent with allowed transitions.

A fifth γ-ray line at 776.3 ± 0.7 keV could only be tentatively assigned to a transition in ^{25}Ne with an intensity of 2..0 ± 1.0 γ-rays per 100 ^{25}F β-decays. If this γ-ray were to feed the 3316 keV level it would imply a state at 4092 keV which would be consistent with both of the transfer measurements and the shell model predictions. However, this suggests that there would be little or no direct feeding of the 3316 keV level. One possible explanation for this apparent discrepancy could be that there is another γ-decay path from the 3316 keV state direct to the ground state which would have a very low detection efficiency ($\approx$ 0.3 %) in this experiment.

The observed γ-ray intensity from the tentative level scheme and an average value of the β-delayed neutron emission accounts for 54 ± 9 % of the total strength. There are several

different possibilities that could account for some of the missing strength. The previously mentioned direct feeding of the 3316 keV state to the ground state could account for the intensity, as could the direct decay from the tentative state at 4092 keV (efficiency ≈ 0.2 %).

5.11 ^{26}F.

The particle stability of $^{26}_9$F$_{17}$ was established by Westfall [West 79] from the fragmentation of a 212 MeV/A ^{48}Ca beam on a Be target. Although there are mass measurements of ^{26}F, [Wout 88, Orr 91], there are no half-life or β-delayed γ-ray emission measurements.

A total of 47497 ^{26}F nuclei were produced during the experiment from three different settings: ^{26}F, ^{31}Na and ^{19}B, this is summarised in table 5.23

LISE3 Setting	Yield	Rate s^{-1}
^{26}F	44693	0.52
^{31}Na	202	0.005
^{19}B	2602	0.015
Total	47497	

Table 5.23: The LISE3 settings and the yield of ^{26}F nuclei produced at each setting with the corresponding implantation rate.

^{26}F β-decays to ^{26}Ne with a Q-value = 17860 ± 130 keV [Audi 95]. ^{26}Ne is a nucleus of special interest, not only because of its neutron richness, but because it is predicted to be a member of the exotic class of what has been called the doubly-magic deformed nuclei. Bohr and Mottelson [Bohr 75] pointed out that for major to minor axis ratio of 2:1, or a β_2 deformation of 0.6, large gaps between single particle levels develop at certain nucleon numbers. These new shell gaps occur at different positions than for spherical nuclei. The new magic numbers are 2, 4, 10, 16, ... Therefore the doubly-magic deformed nuclei would be $^6_2$He$_4$, $^{14}_4$Be$_{10}$, $^{26}_{10}$Ne$_{16}$,etc. as predicted by Sheline [Shel 76]. Although the initial calculations were performed using a harmonic oscillator potential, a more realistic potential indicated essentially the same result [Ragn 81].

^{26}Ne was first observed by Artukh [Artu 70a] by bombarding 174 MeV ^{22}Ne ions on a

^{232}Th target. Nann *et al.* [Nann 80] using a pion double charge exchange reaction on ^{26}Mg: ^{26}Mg(π^-, π^+)^{26}Ne observed an excited state at ≈ 3.75 MeV. This state was assigned to be 0^+ due to the kinematic restriction of the transmission of only L = 0 transitions from their experimental technique.

5.11.1 Beta-delayed Gamma-ray Spectrum.

The spectrum produced from the β-delayed γ ray emission of ^{26}F is shown in figure 5.33 with a time condition that only β-delayed γ rays occurring within 50 ms of an implantation of a ^{26}F ion are taken. Two lines have been identified which are still prominent after

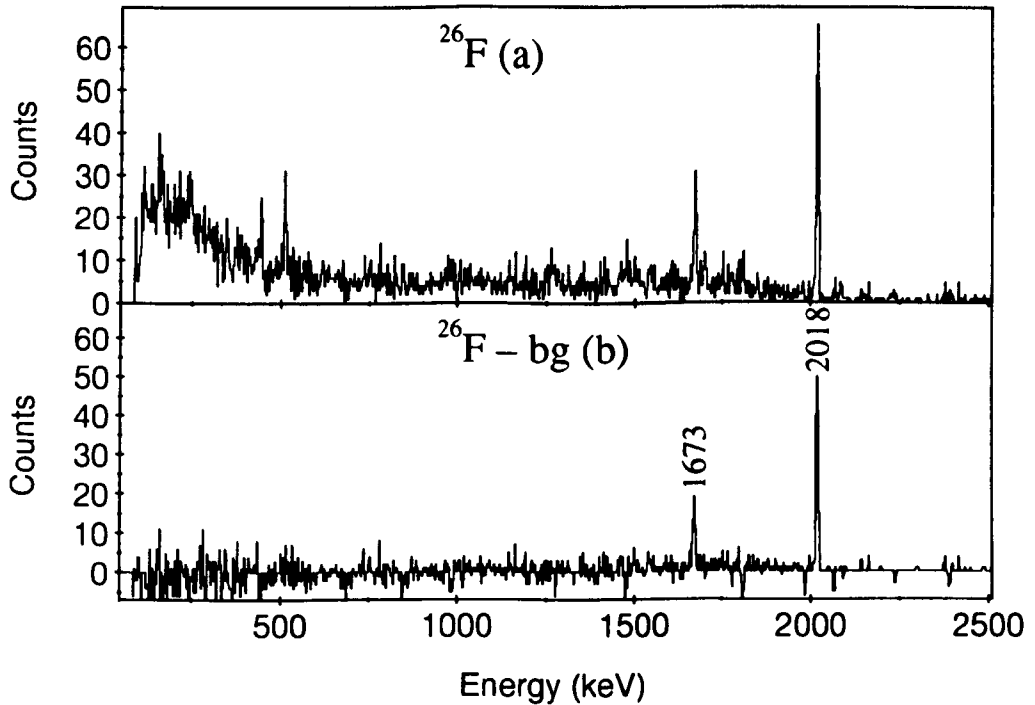Figure 5.33: The β-delayed γ ray spectrum produced for ^{26}F (a) and the corresponding background subtracted (b).

a normalised fraction of the background has been removed and these are summarised in table 5.24.

E_γ (keV)	I_γ	I_γ (relative)	I_γ (per 100 decays)
1673.0 ± 0.3	8880 ± 1040	28 ± 4	19 ± 2
2018.2 ± 0.1	31970 ± 2950	100 ± 10	67 ± 6

Table 5.24: Energy and intensity of γ-rays observed in the β-decay of ^{26}F.

The P_n value for ^{26}F was also measured for the first time from this experiment in the parallel analysis of the data, and a value of 11 ± 4 % was obtained. No γ rays are observed which are associated with the decay of ^{25}Ne (see section 5.10).

5.11.2 Half-life Calculation and Results.

Gates were set on the 1673 keV and 2018 keV transitions and a maximum likelihood fit was applied on the individual lifetime spectra. The values obtained were consistent and an average value of the measured lifetimes was taken. The value obtained was 10 ± 1 ms (see figure 5.34).

5.11.3 Comparisons with Single Particle Shell Model Calculations.

Based on the measured intensities of the γ rays, the more intense line at 2018 keV is assigned to represent the $2^+ \rightarrow 0^+$ transition in ^{26}Ne, while the 1673 keV line is assumed to represent a γ-decay to this 2^+ level (see figure 5.35). The relative intensities of these two lines and the non-observation of any other γ-ray lines indicate that both levels are populated directly in the β-decay of ^{26}F. This interpretation is consistent with the level scheme calculated in the spherical shell model using the USD interaction [Wild 84] which is compared with the experimental level scheme in figure 5.35. The ground state of ^{26}F is predicted to have a spin and parity assignment of $J^\pi = 1^+$ and would restrict the 3691 keV level to have $J^\pi = 0^+$ or 2^+ assuming an allowed β-decay.

The energy of this state is consistent with that measured by Nann et al. and is shown in figure 5.35 for comparison. Since we would expect to observe this level in our measurements, assuming $J^\pi = 1^+$ for the ^{26}F ground state, the 3691 keV level is tentatively assigned as the 0^+ level observed by Nann et al. This observation is consistent with the level scheme of
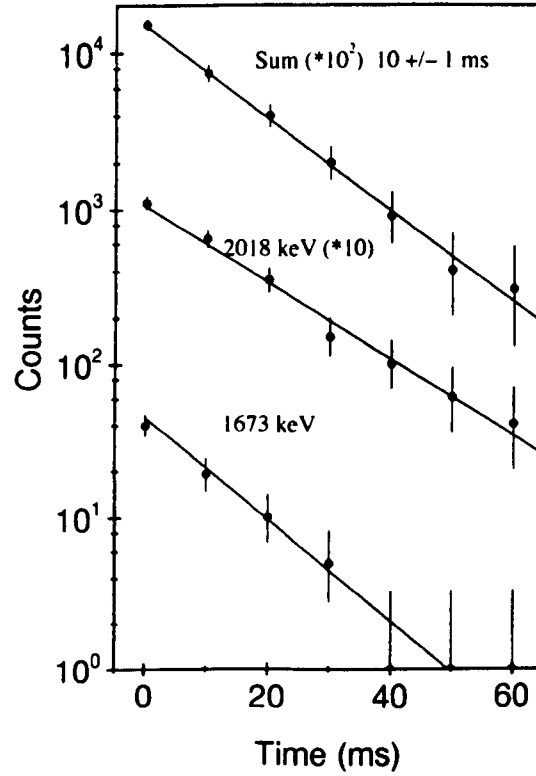
Figure 5.34: Half-life decay curves associated with the β-decay of ^{26}F. These curves were produced by setting gates on the two known β-delayed γ-rays from the decay of ^{26}F and performing a maximum likelihood fit to the curves.

^{28}Mg [Guil 84], deduced from the β-decay of the $J^\pi = 1^+$ ground state of ^{28}Na [Hube 78] in which the two most strongly populated excited states are the first and second excited states with $J^\pi = 2^+$ and 0^+ respectively. If the relative feeding strength of the second excited 2^+ level in the decay of ^{26}F were similar to that in the decay of the isotone ^{28}Na the γ-ray intensity from this level to the ground state of ^{26}Ne would be below the sensitivity limits of the present experiment. The feeding intensities and $\log_{10} ft$ value deduced for each level are represented in table 5.25, from which it can be seen that all of the values are consistent with allowed β-decay transitions. The feeding intensity of the ground state of 21 $\pm$ 7 % arises from the combination of the absolute feeding intensities of the levels deduced in the
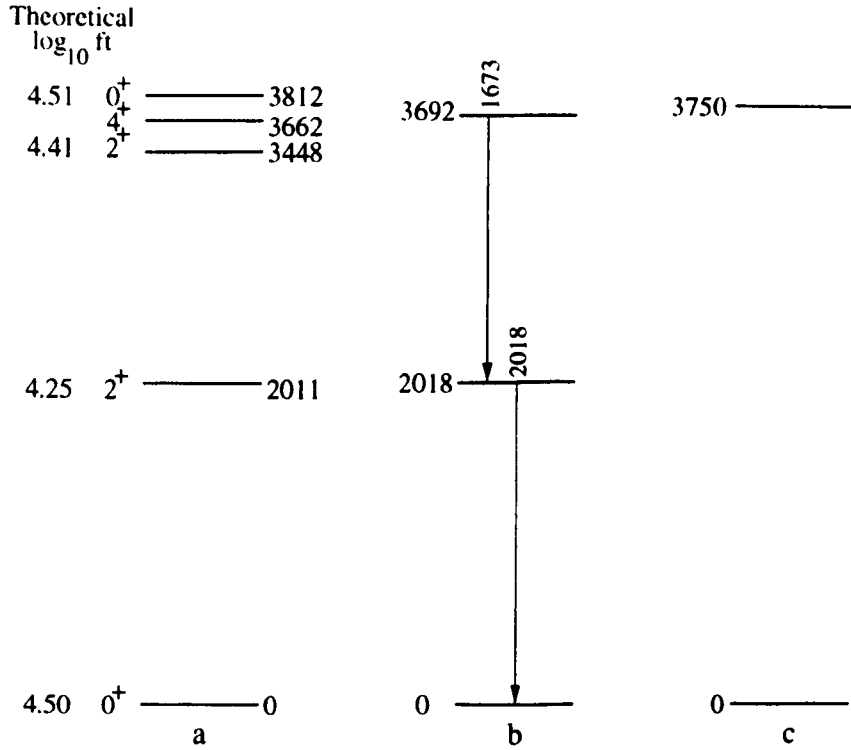
Figure 5.35: Comparison of a) the shell model calculations with the USD interaction [Wild 84]; b) the partial decay scheme deduced in the present work; and c) the energy levels identified by Nann *et al.* The excitation energies of the levels and the γ-ray transition energies are given to the nearest keV.

above interpretation and the P_n value.

Figure 5.36 shows the excitation energies of the even-even nuclei in this region including the present measurement for ^{26}Ne. The excitation energy of the lowest-lying 2^+ level is significantly lower in ^{32}Mg than in neighbouring nuclei and is known to arise due to ^{32}Mg having a deformed ground state [Fuku 92]. It is evident that the excitation energy measured for the 2^+ level in ^{26}Ne is compatible with the known value of 1982 keV for ^{24}Ne [Dufo 86].

5.12 ^{27}F.

Gillibert *et al.* [Gill 86] first observed $^{27}_{9}$F$_{18}$ by fragmenting a 44 MeV/A beam of ^{40}Ar on a thick Ta target. There have been no previous β-delayed γ ray or neutron emission mea-

E_{level} (keV)	J^π	% fed	Q_β (keV)	$\log_{10} ft$
3691.2 ± 0.3	0^+	19 ± 2	14169 ± 130	4.69 ± 0.11
2018.2 ± 0.1	2^+	49 ± 7	15842 ± 130	4.53 ± 0.13
0	0^+	22 ± 10	17860 ± 130	5.2 ± 0.4

Table 5.25: The states produced in the decay of ^{26}F to ^{26}Ne and their corresponding $\log_{10} ft$ values. The total number of ^{26}F nuclei produced decaying to the ^{26}Ne ground state is corrected for the β-n channel to ^{25}Ne, which has a measured probability of 11 ± 4 % [Tara 97b]

surements performed but the half-life was previously measured by Tarasov *et al.* [Tara 97a] to be 5.3 ± 0.9 ms.

A total of 10266 ^{27}F nuclei were produced during the experiment from four different settings: ^{31}Na, ^{26}F, ^{19}B and ^{29}F, this is summarised in table 5.26.

LISE3 Setting	Yield	Rate s^{-1}
^{31}Na	1426	0.03
^{26}F	3606	0.04
^{19}B	4608	0.03
^{29}F	626	0.004
Total	10266	

Table 5.26: The LISE3 settings and the yield of ^{27}F nuclei produced at each setting with the implantation rate.

5.12.1 Beta-delayed Gamma-ray Spectrum.

The energy spectrum of β-delayed γ-rays occurring within 30 ms of the detection of a ^{27}F ion is shown in figure 5.37b. Only a single γ-ray line is evident in this spectrum, at an energy of 2018 keV, the energy of the $2^+ \rightarrow 0^+$ transition in ^{26}Ne identified above. Figure 5.37a
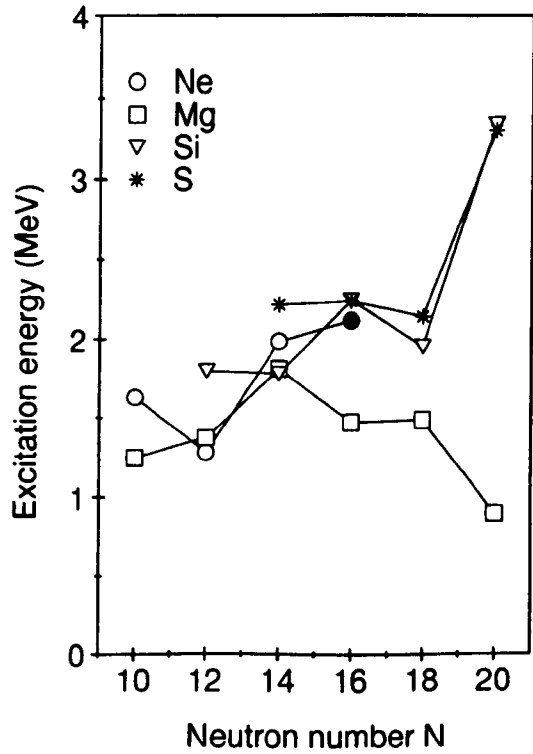
Figure 5.36: Excitation energies of the lowest lying 2^+ states in even-even isotopes of neon (circles), magnesium (squares), silicon (triangles) and sulphur (stars). The energy of the 2^+ state in ^{26}Ne measured for the first time in the present work is indicated by the filled circle. The lines are drawn to guide the eye.

shows the energy spectrum taken for ^{26}F for the same time range for comparison. This is compatible with the P_n value measurement of $90 \, {}^{+10}_{-30} \, \%$ in the parallel analysis of this data [Tara 97b]. The energy and intensity of this γ ray are summarised in table 5.27

E_γ (keV)	I_γ	I_γ (per 100 decays)
2018.1 ± 1.0	1850 ± 350	18 ± 3

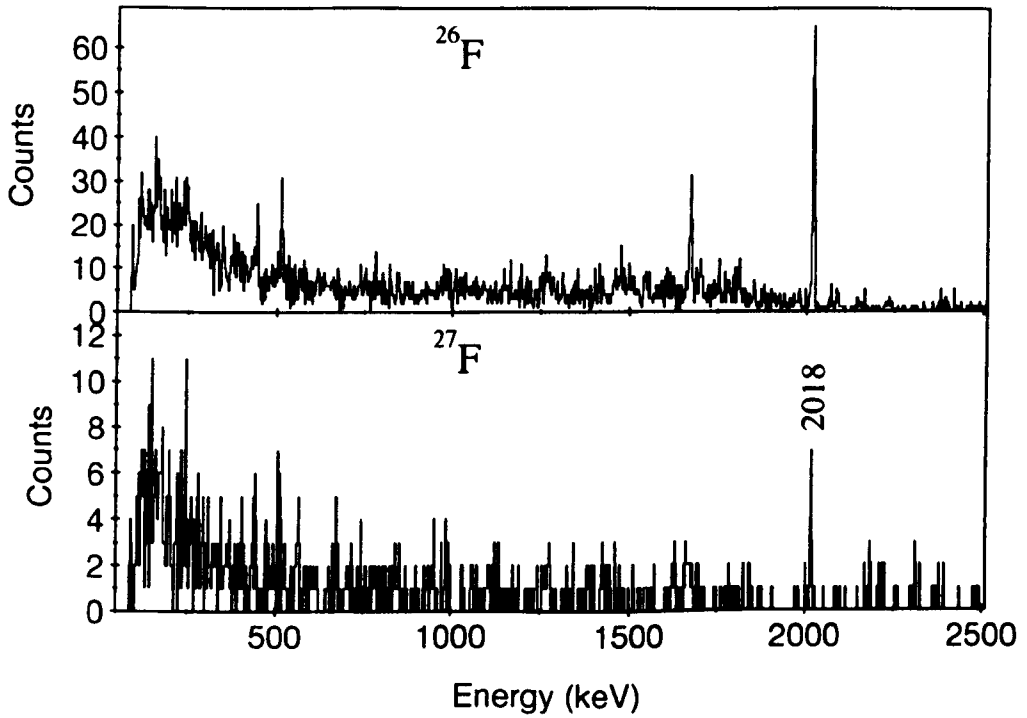Table 5.27: Energy and corrected intensity of the γ ray observed in the β-decay of ^{27}F.

Figure 5.37: Gamma-ray spectra from the study of ^{27}F looking for β-delayed γ-events. Spectrum (a) shows the total number of β-delayed γ events collected 30 ms after a ^{26}F ion is detected. Spectrum (b) shows the total number of β-delayed γ-events collected 30 ms after a ^{27}F ion is detected.

The high P_n value and absolute intensity of the γ ray gives an indication of the relative population of the ground state and excited states in the neutron emission process as given in table 5.28 and figure 5.38. These measurements and the absence of any other γ-ray line in

E_{level} (keV)	J^π	% fed Normalised to 100
2018 ± 1.0	2$^+$	18 ± 3
0	0$^+$	82 ± 3

Table 5.28: The feeding intensities of the states in ^{26}Ne via the β-n decay channel of ^{27}F.
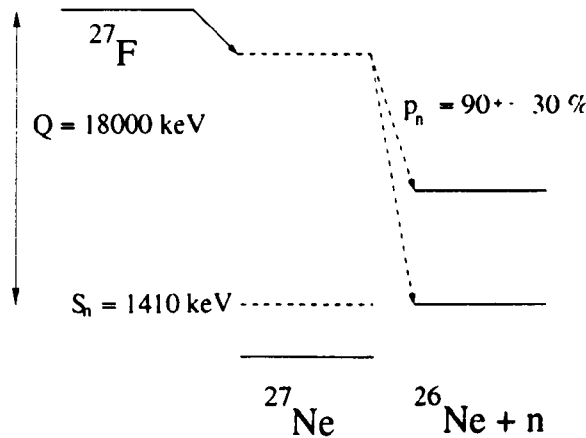
Figure 5.38: Schematic showing the β-decay of ^{27}F.

the spectrum are also consistent with the low neutron separation energy of 1408 ±106 keV for ^{27}Ne [Audi 95] and shell model calculations, which predict that no excited levels below this threshold are strongly populated in the β-decay.

5.12.2 Half-life Calculation and Results.

The half-life measured in the present work for ^{27}F was 6.5 ± 1.1 ms, figure 5.39, from the difference between the implantation of a ^{27}F ion and the detection of any β-γ event. This is consistent with the previous measurement.

5.13 ^{29}F.

The next particle bound isotope of fluorine is $^{29}_{9}$F$_{20}$ as $^{28}_{9}$F$_{19}$ is known to be particle unbound [Guil 89]. ^{29}F was first observed in an experiment by Guillemaud-Mueller et al. by fragmenting ^{48}Ca^{18+} at 55 MeV/A on a Ta target. Tarasov et al. previously measured the half-life [Tara 97a].

A total yield of 651 ^{29}F nuclei were produced during this experiment at one setting of the spectrometer for ^{29}F with a count rate of 0.004 nuclei s^{-1}. From such a small number of nuclei produced it was not possible to obtain any β-delayed γ-ray information for ^{29}F but a measurement of the half-life was viable, yielding a value of 2.9 ± 0.8 ms (see figure 5.39) which is consistent with the previous reported value of 2.4 ± 0.8 ms [Tara 97a].
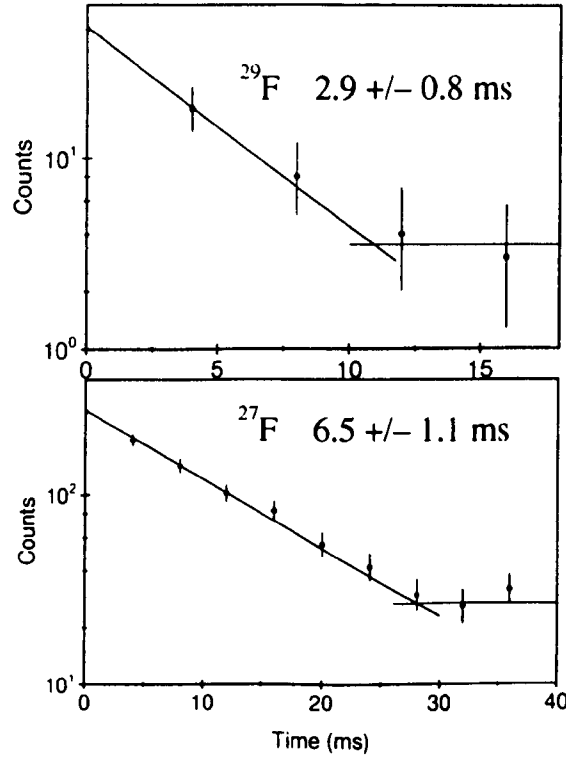
Figure 5.39: Bottom spectrum shows the half-life curve associated with the decay of ^{27}F. The top one shows that corresponding to ^{29}F.

5.14 ^{28}Ne.

Viyogi et al. [Viyo 79] and Symons et al. [Symo 79] confirmed the particle stability of $^{28}_{10}$Ne$_{18}$ during some of the first few experiments involving fragmentation reactions aimed at searching for neutron-rich nuclei. In these experiments a ^{40}Ar beam at 213 MeV/A was fragmented on a C target. A total yield of 105018 ^{28}Ne nuclei was produced during this experiment making it the most prolifically produced nuclide. This yield was produced at three settings and is summarised in table 5.29.

Previous measurements of the half-life of ^{28}Ne (17 $\pm$ 4 ms) and of the P_n value for ^{28}Ne (22 $\pm$ 3 %) [Teng 92] have been performed but no β-γ information has previously been obtained for ^{28}Ne. ^{28}Ne β-decays to ^{28}Na with a $Q_{\beta-}$ of 12310 $\pm$ 136 keV [Audi 95] and the

LISE3 Setting	Yield	Rate s^{-1}
^{31}Na	4742	0.11
^{26}F	97896	1.13
^{19}B	2380	0.01
Total	105018	

Table 5.29: The LISE3 settings and the yield of ^{28}Ne nuclei produced at those settings with the implantation rate.

ground state of the daughter nucleus has been previously measured as being 1^+ [Roek 74]

5.14.1   Beta-delayed Gamma-ray Spectrum.

The energy spectrum of β-delayed γ rays observed within 50 ms of the arrival of a ^{28}Ne ion is shown in figure 5.40a and figure 5.40b shows the corresponding background subtracted spectrum. Of the four prominent peaks that are marked in the latter spectrum, those at 1473 keV and 2389 keV arise from the two most strongly populated excited states in ^{28}Mg [Roek 74] ($t_{1/2}$ = 30.5 ±0.4 ms). The other marked γ ray lines are unknown and have been assigned to the decay from excited states in ^{28}Na. These two γ rays are summarised in table 5.30.

The P$_n$ value for ^{28}Ne was also remeasured in the parallel analysis of the data [Tara 97b] to be 11 ± 3 %, which is consistent with previous measurements [Teng 92, Reed 91]. Also produced in this experiment with a yield of 13275 nuclei was ^{27}Ne at one setting of the spectrometer (^{26}F) with a count rate of 0.15 nuclei s^{-1}. This was insufficient to identify β-delayed γ rays, but the daughter nucleus of the β-decay of this nucleus, ^{27}Na, has some known excited states at 1.72 ± 0.04 MeV, 2.21 ± 0.03 MeV, 3.82 ± 0.04 MeV, 4.98 ± 0.05 MeV and 5.59 ± 0.05 MeV (from Fifield et al. [Fifi 85]) from the reaction ^{26}Mg(^{18}O,^{17}F)^{27}Na with a beam energy of 100 MeV. None of these states would produce γ rays that would coincide with the observed γ rays. Furthermore, the widths of the 865 keV and and 2063 keV γ-ray lines show no sign of Doppler broadening, suggesting that they are not emitted after neutron emission. It is tentatively concluded that the γ-rays are indeed from excited states in ^{28}Na.
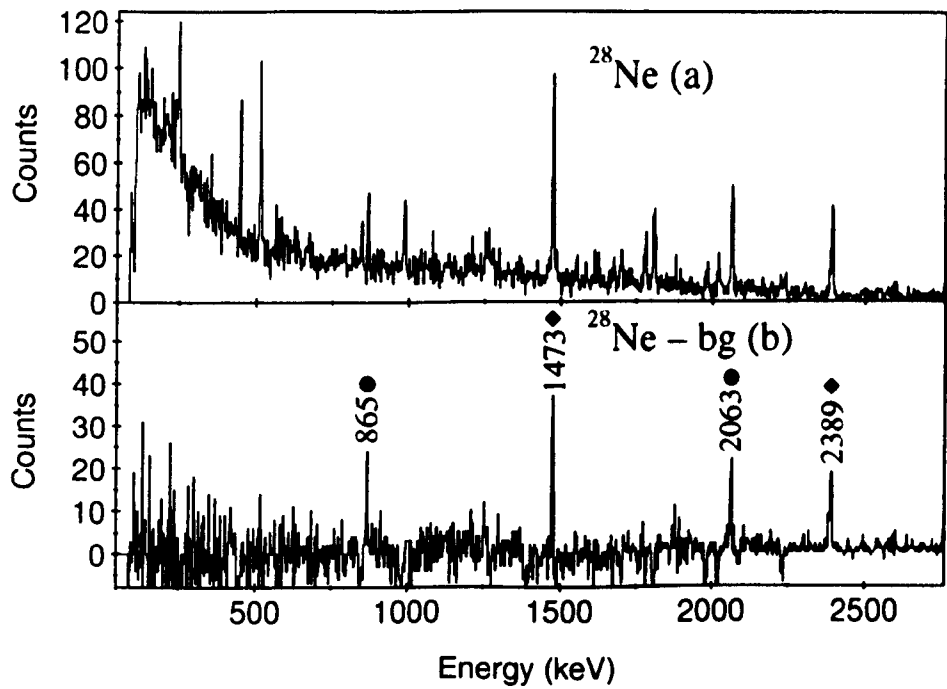
Figure 5.40: Gamma-ray spectra from the study of ^{28}Ne looking for β-delayed γ-events. Spectrum (a) shows the total number of β-delayed γ-events collected within 50 ms after a ^{28}Ne ion is detected. Spectrum (b) shows the corresponding background subtracted β-delayed γ-ray spectra with four peaks labelled; those labelled with a circle have been assigned as to be arising from excited states in ^{28}Na, and those with a diamond are from known excited states in ^{28}Mg.

E_γ (keV)	I_γ	I_γ (relative)	I_γ (per 100 decays)
864.5 ± 0.4	3500 ± 400	18 ± 2	3.3 ± 0.4
2062.9 ± 0.3	20000 ± 1200	100 ± 6	19 ± 2

Table 5.30: Energy and intensity of γ rays observed in the β-decay of ^{28}Ne.

5.14.2 Half-life Calculation and Results.

The half-life for ^{28}Ne was calculated using γ-ray gates set on the 865 keV and 2063 keV transitions and an average half-life was obtained from maximum likelihood fits to the individual time difference spectra. The value obtained was 18 ± 3 ms, figure 5.41, which is consistent with the previous measurement.
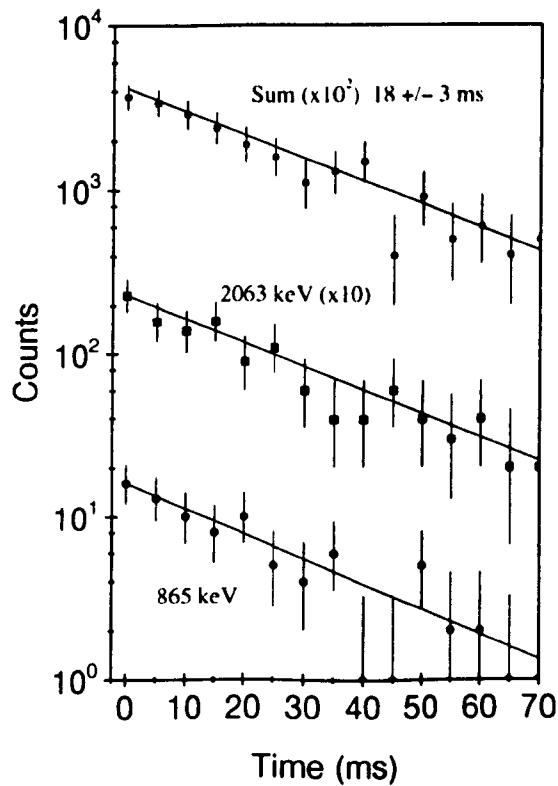
Figure 5.41: Half-life decay curves associated with the β-decay of ^{28}Ne. These curves were produced by setting gates on the two β-delayed γ rays from the decay of ^{28}Ne and applying a maximum likelihood fit to the curves.

5.14.3 Comparisons with Single Particle Shell Model Calculations.

Since ^{27}Na is the heaviest sodium isotope studied using transfer reactions, the γ rays assigned to heavier isotopes can only be compared with shell model calculations. The level

scheme calculated using the USD interaction [Wild 84] is shown in figure 5.42. Note that

Figure 5.42: Level schemes produced for ^{28}Na by Suhonen [Suho 98] (left) with the theoretical $\log_{10} ft$ values, shown together with the level scheme for ^{28}Na deduced from this work (right).

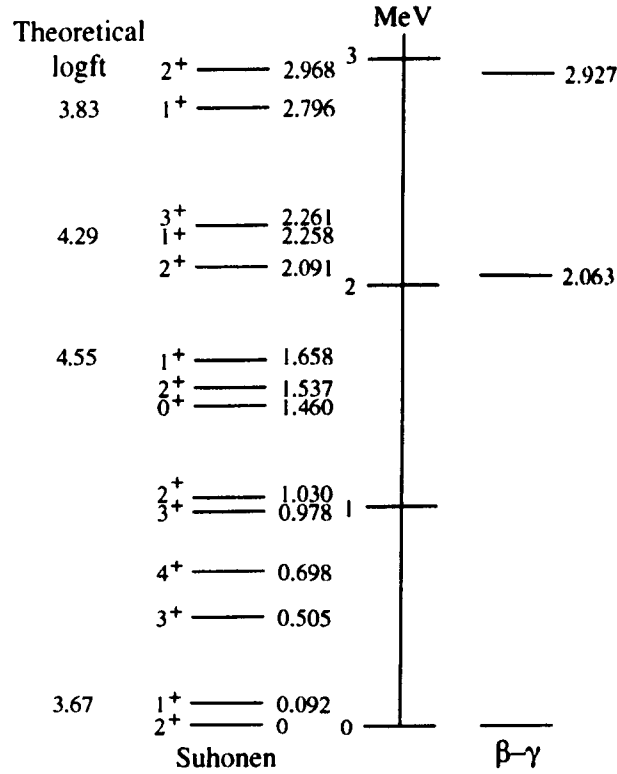the ground state spin and parity of ^{28}Na has been determined as being 1^+ [Rock 74], rather than the 2^+ level which is predicted to lie 92 keV below the lowest 1^+ state.

The shell model calculations predict there to be three excited 1^+ states between the ground state and the one neutron separation energy which could be populated by allowed β-decays from ^{28}Ne. The two higher levels at 2258 keV and 2796 keV are predicted to have lower $\log_{10} ft$ values than the state at 1658 keV. The γ-rays identified in the present work would therefore provide good agreement with the calculations if the 2063 keV transition were to correspond to the γ-ray of the 1^+ level at 2258 keV to the ground state and the 865 keV transition arising from a level at 2927 keV feeding this state and would correspond to the predicted 1^+ level at 2796 keV. In principle, however, the observed γ rays could feed the low-lying 2^+ level and the γ-decay of this level to the ground state would be unobserved,

being below the energy threshold of the germanium detectors. The tentative partial level scheme is proposed in figure 5.42 and compared with the shell model calculations. There is no strong evidence for a γ-ray line at 1.6 MeV which could represent the decay of the predicted level at 1658 keV to the ground state. The deduced $\log_{10} ft$ values for the tentative level scheme are given in table 5.31. The direct feeding of the ground state has been assumed

E_{level} (keV)	J^π	% fed	Q_β (keV)	$\log_{10} ft$
2927.4 ± 0.5	1^+	3.5 ± 0.5	9380 ± 150	4.81 ± 0.19
2062.9 ± 0.3	1^+	16 ± 2	10250 ± 150	4.32 ± 0.11
0	1^+	64 ± 3^1	12300 ± 150	4.07 ± 0.10

Table 5.31: The states produced in the decay of ^{28}Ne to ^{28}Na and their corresponding $\log_{10} ft$ values. [1] The total number of ^{28}Ne nuclei produced decaying to ^{28}Na is corrected for the β-n channel to ^{27}Na, which has an average probability of 16 ± 2 %.

to account for all the unobserved decay strength and results in a reasonable $\log_{10} ft$ value. A highly fragmented decay path of the excited states would reduce the assumed feeding intensity of the ground state and hence increase the $\log_{10} ft$ value.

5.15 ^{29}Ne.

Guillemaud-Mueller et al. [Guil 90] observed $^{29}_{10}$Ne$_{19}$ by fragmenting a 44 MeV/A beam of ^{48}Ca on a tantalum target. The decay half-life of this nucleus was recently measured by Tarasov et al. [Tara 97a] to be 15 ± 3 ms.

A total yield of 8625 ^{29}Ne nuclei were produced during this experiment from four settings: ^{31}Na, ^{26}F, ^{19}B and ^{29}F and the production rates are summarised in table 5.32.

5.15.1 Beta-delayed Gamma-ray Spectrum.

The spectrum of β-delayed γ rays occurring within 50 ms of the arrival of a ^{29}Ne ion is shown in figure 5.43a and the corresponding background subtracted spectrum in figure 5.43b. There are four identified γ rays which do not arise from the decay of the daughter nucleus

LISE3 Setting	Yield	Rate s^{-1}
^{31}Na	5319	0.12
^{26}F	2546	0.03
^{19}B	545	0.003
^{29}F	215	0.001
Total	8625	

Table 5.32: The LISE3 settings and the yield of ^{29}Ne nuclei produced at each setting with the corresponding implantation rate.

[Lang 85, Guil 84]. The P_n value of 27 $\pm$ 9 % was measured in a parallel analysis of the current data [Tara 97b] and the four identified γ rays do not correspond to those γ rays tentatively assigned to transitions in ^{28}Na. They have therefore been tentatively assigned to transitions in ^{29}Na, as summarised in table 5.33. The γ ray at 2822 $\pm$ 3 keV has a

E_γ (keV)	I_γ	I_γ (relative)	I_γ (per 100 decays)
223.8 $\pm$ 0.7	880 $\pm$ 160	19 $\pm$ 6	10 $\pm$ 2
1176.5 $\pm$ 1.0	1550 $\pm$ 260	33 $\pm$ 9	18 $\pm$ 3
2918.2 $\pm$ 1.5	4720 $\pm$ 1110	100 $\pm$ 24	55 $\pm$ 13

Table 5.33: Energy and corrected intensity of γ rays observed in the β-decay of ^{29}Ne.

measured intensity of 13 $\pm$ 10 % and due to the low β-γ efficiency ($\approx$ 0.4 %) and small number of counts in the peak, it has been only tentatively identified as a peak and will not be further discussed in the following section.

5.15.2 Half-life Calculation and Results.

The half-life for ^{29}Ne was measured to be 17 $\pm$ 3 ms from performing a maximum likelihood fit, figure 5.44.

No gates were set on the assigned γ-ray transitions and the ratio of background to peak
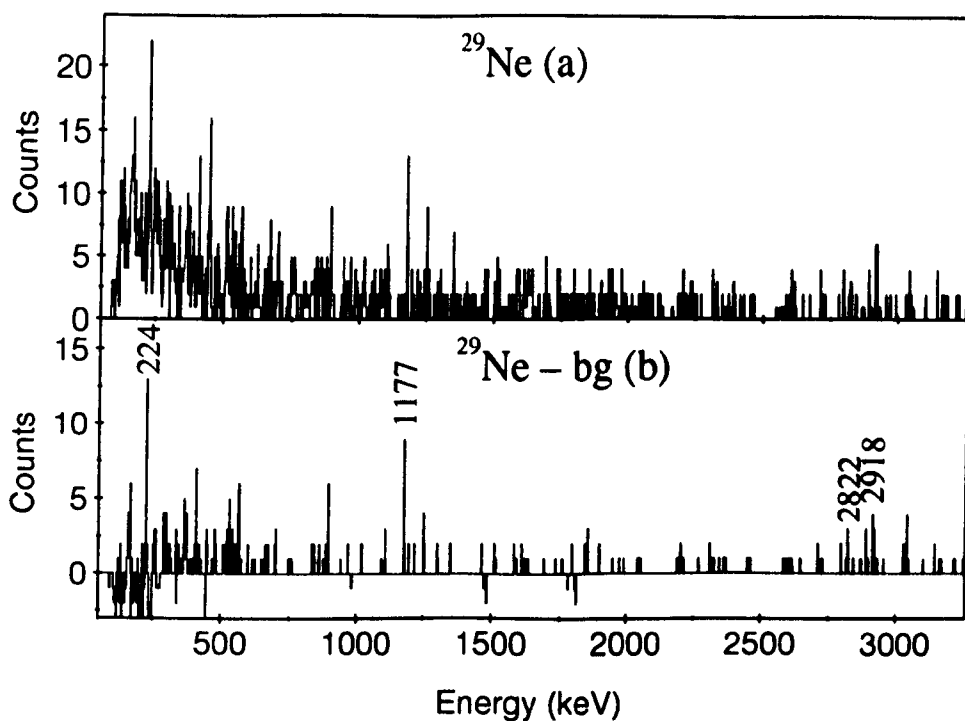
Figure 5.43: Gamma-ray spectra from the study of ^{29}Ne looking for β-delayed γ-events. Spectrum (a) shows the total number of β-delayed γ events collected within 50 ms after a ^{29}Ne ion is detected. There are three peaks labelled in spectrum (b) which shows the corresponding background-subtracted spectrum.

intensity is quite high which could contribute towards the spurious points at the longer time interval after an ion implantation.

5.15.3 Discussion of ^{29}Ne.

As with ^{28}Na, it is only possible to compare the γ-rays assigned to this nucleus with the shell model calculations performed using the USD interaction [Wild 84] as shown in figure 5.45. The ground state spin and parity of ^{29}Na has been previously measured to be $3/2^+$ from laser and β-decay measurements [Hube 78, Guil 84] in contradiction to the $5/2^+$ predicted to lie 137 keV below the $3/2^+$ state in the USD interaction. The spin and parity of the ground state of ^{29}Ne is predicted to be $3/2^+$ from shell model calculations [Suho 98], the
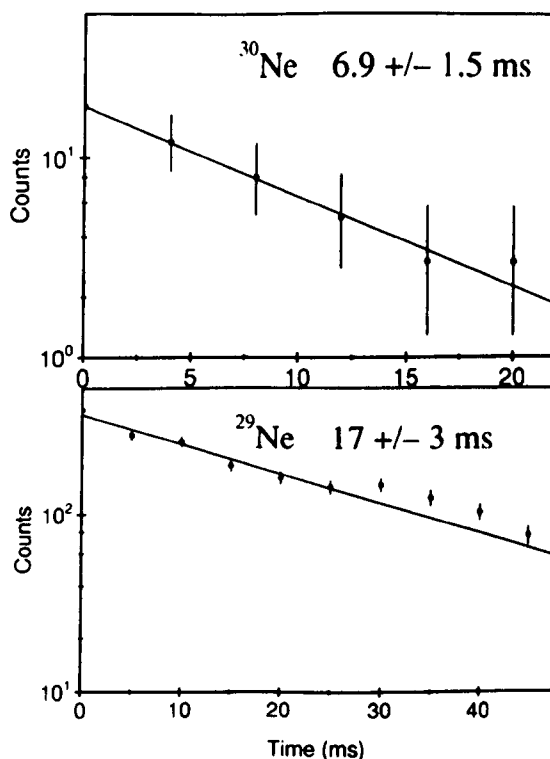
Figure 5.44: Decay half-life spectra associated with ^{29,30}Ne.

theoretical $\log_{10}$ ft values shown in figure 5.45 indicates that ^{29}Ne is expected to β-decay to the ^{29}Na ground state.

The 2918 keV γ-ray accounts for 55 % of the total decay strength and is significantly more intense than the other two γ-ray lines suggesting that it possibly represents the decay of a level at 2918 keV directly to the ground state. The shell model calculations predict a $3/2^+$ level at 2807 keV which has a theoretical $\log_{10}$ ft value of 4.9 indicating an allowed transition. This energy corresponds well to the 2918 keV transition.

The placement of the 224 keV and 1177 keV transitions is not so clear and the low statistics hamper the construction of a level scheme for ^{29}Na in the current work.
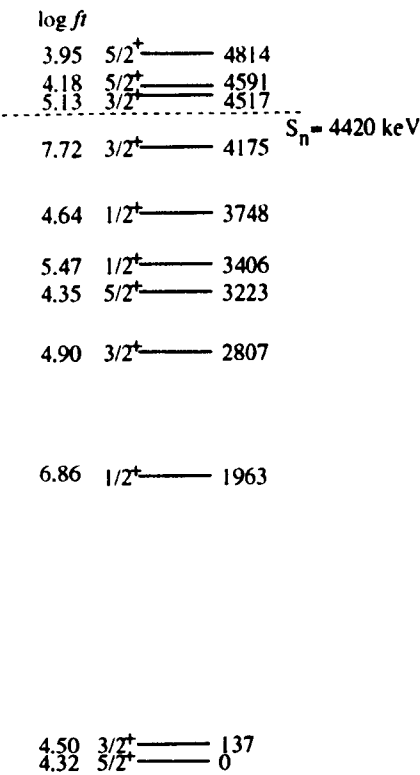
```
log ft
3.95   5/2⁺ ———— 4814
4.18   5/2⁺ ————= 4591
5.13   3/2⁺ ————= 4517
- - - - - - - - - - - - - - - - - - - - - - - - - - - -        Sₙ = 4420 keV
7.72   3/2⁺ ———— 4175

4.64   1/2⁺ ———— 3748

5.47   1/2⁺ ———— 3406
4.35   5/2⁺ ———— 3223

4.90   3/2⁺ ———— 2807


6.86   1/2⁺ ———— 1963




4.50   3/2⁺ ————= 137
4.32   5/2⁺ ————= 0
```

Figure 5.45: Shell model calculations with the USD interaction [Wild 84], including calculated theoretical $\log_{10} ft$ values.

5.16 ^{30}Ne.

Orr *et al.* [Orr 91] have suggested that the N = 20 shell closure for the singly magic nucleus $^{30}_{10}$Ne$_{20}$ may not be valid. This conclusion arose from the measured mass excess differing from the predicted shell model calculations [Warb 90] by approximately -2 MeV, similar to the effect seen in ^{31}Na and ^{32}Mg [Thib 75, Detr 83]. This conclusion is also supported by several large scale shell model calculations [Fuku 92, Pove 94, Warb 90]. The ground state of ^{30}Ne is expected to have a majority intruder ($2\hbar\omega$) character whereas the ground state of ^{30}Na has been calculated to be mostly an sd shell ($0\hbar\omega$) configuration [Pove 87]. Consequently one would expect that the β-decays of the ground state of ^{30}Ne should mainly populate the $2\hbar\omega$ states in ^{30}Na.

A total yield of 3000 ^{30}Ne nuclei were produced during this experiment at three settings: ^{31}Na, ^{19}B and ^{29}F and this is summarised in table 5.34.

LISE3 Setting	Yield	Rate s^{-1}
^{31}Na	740	0.02
^{19}B	174	0.001
^{29}F	2086	0.01
Total	3000	

Table 5.34: The LISE3 settings and the yield of ^{30}Ne nuclei at each setting with the production rate.

5.16.1 Beta-delayed Gamma-ray Spectrum.

The energy spectrum produced from the β-delayed γ rays emitted within 30 ms of the implantation of a ^{30}Ne ion is shown in figure 5.46a. Only one peak is observed which is not known from the decay of ^{30}Na [Baum 89] and the P$_n$ value for ^{30}Ne was measured to be 9 ± 17 % in the parallel analysis [Tara 97b] indicating that this γ-ray line must represent a transition in ^{30}Na. The characteristics of this peak are summarised in table 5.35.

E$_\gamma$ (keV)	I$_\gamma$	I$_\gamma$ (per 100 decays)
150.6 ± 0.2	2850 ± 300	95 ± 10

Table 5.35: Energy and corrected intensity of the γ-ray observed in the β-decay of ^{30}Ne.

5.16.2 Half-life Calculation and Results.

A gate was set on the 151 keV transition and a value of 6.9 ±1.5 ms for the half-life was obtained after applying a maximum likelihood fit to the data, see figure 5.44, which is consistent with the previous measurement [Tara 97a].

5.16.3 Comparisons with Single Particle Shell Model Calculations.

The calculated lowest energy $0\hbar\omega$ and $2\hbar\omega$ levels in ^{30}Na using the WBMB interaction [Warb 90] are shown in figure 5.47. The 1$^+$ level predicted to lie 276 keV above the 2$^+$
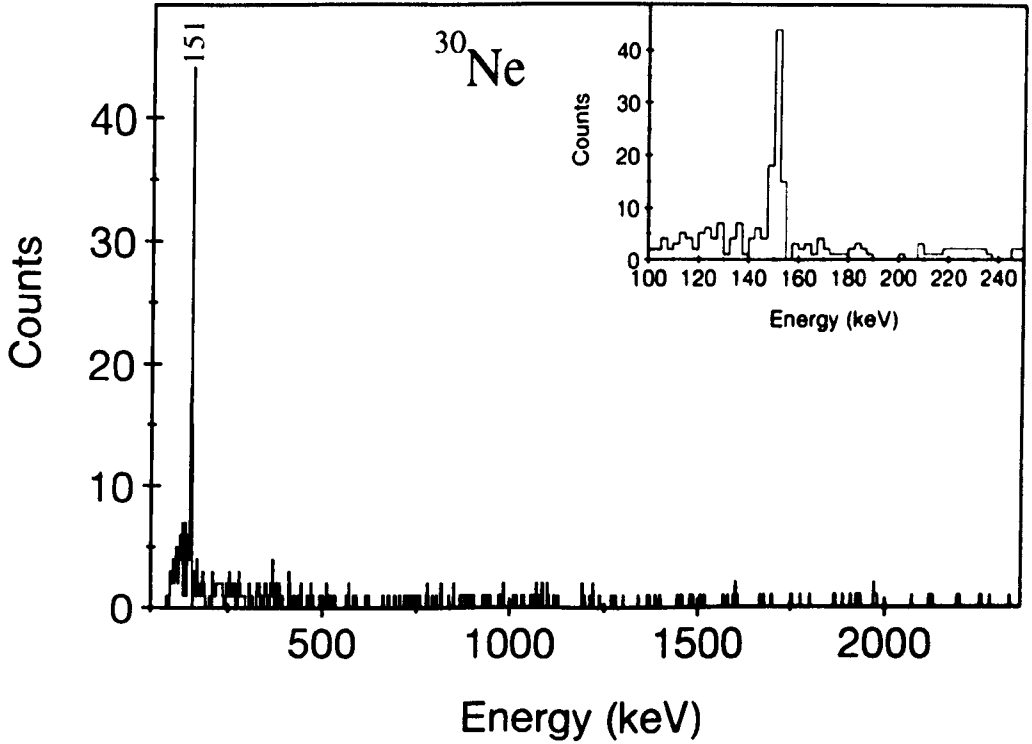
Figure 5.46: Gamma-ray spectrum from the study of ^{30}Ne looking for β-delayed γ-events. Spectrum (a) shows the total number of β-delayed γ-events collected 30 ms after a ^{30}Ne ion is detected, there is one peak labelled. The insert spectrum (b) shows an enlargement of the 100 → 250 keV region.

lowest $2\hbar\omega$ state is expected, from the calculations, to have strong direct feeding by an allowed β-decay from the ground state of ^{30}Ne, so the γ-ray identified in the present work is tentatively assigned to the decay of the 1^+ level to the 2^+ state.

The excitation energy of the lowest-lying $2\hbar\omega$ state above the $0\hbar\omega$ ground state in ^{30}Na is calculated to be 1423 keV in the present work, which compares with the previous estimates of $\approx$ 1.9 MeV [Pove 94] and $\approx$ 0.8 MeV [Warb 90]. The spin of the ground state has been determined to be 2 $\hbar$ [Hube 78] and in principle one would expect the lowest $2\hbar\omega$ state eventually to decay by some path to the $0\hbar\omega$ ground state. However, no evidence could be found in the spectrum of figure 5.46 for any connecting transition, although this may be a reflection of the lower detection efficiency for higher energy γ rays and a possibly fragmented
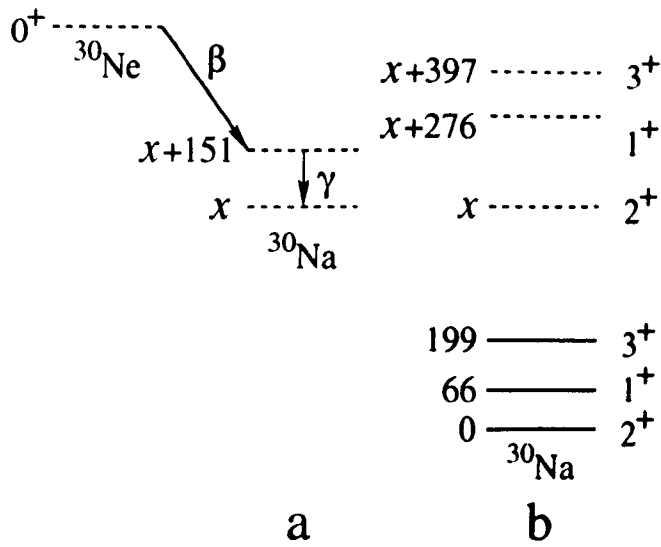
Figure 5.47: Comparison of a) the tentative experimental level scheme for ^{30}Na with b) shell model estimates of the lowest energy $0\hbar\omega$ and $2\hbar\omega$ levels calculated using the WBMB interaction [Warb 90]. The solid lines represent the energies of the $0\hbar\omega$ levels, while the $2\hbar\omega$ levels are indicated by the dashed lines. The relative energies of the lowest-lying $0\hbar\omega$ and $2\hbar\omega$ levels, denoted here by x, is unknown in ^{30}Na. See text for details of theoretical estimates of this quantity.

decay path between the states.

Assuming that all of the observed strength arises as a result of direct β-decay feeding of the level gives the $\log_{10} ft$ value for the population of the 151 keV state to be 3.7 ± 0.2 (see table 5.36) which is consistent with an allowed transition. Given that the one neutron sep-

E_{level} (keV)	% fed	Q_β (keV)	$\log_{10} ft$
150.6 ± 0.2	100 ± 10	13500 ± 150	3.7 ± 0.2

Table 5.36: The state produced in the decay of ^{30}Ne to ^{30}Na and its corresponding $\log_{10} ft$ value.

aration energy of ^{30}Na is 2100 ± 300 keV [Audi 95] and the next $2\hbar\omega$ 1^+ state is calculated to lie around 2 MeV above the $2\hbar\omega$ 'ground state', it does not seem unreasonable that this

strength should represent essentially all of the strength not involving neutron emission and is entirely consistent with shell model predictions.

5.17 Summary.

This work has presented the first β-delayed γ-ray measurements for ten nuclei residing close to or at the neutron drip line. In some cases it has been possible to interpret the measured γ-ray spectra through comparison with shell model calculations and transfer reaction measurements. The results from the parallel analysis of this work looking at just the β-delayed neutron emission have shown good agreement with the results shown here looking at the β-delayed γ-ray measurements. Also shown here for some of the nuclei presented were the half-life measurements performed which have compared favourably with previous measurements of these values

Some of the nuclei investigated here are also the subject of Coulomb excitation and in-beam fragmentation measurements [Azai 98] which potentially provides complementary information, as well as the prospect of measuring excited levels in nuclei such as ^{30}Ne where the β-decay precursors are unbound. Data from a recent deep-inelastic experiment using the Euroball array with a ^{26}Mg beam on a ^{208}Pb target will further complement the results presented here.

Increases in the beam intensity and γ-ray detection efficiency that will soon be available will offer new opportunities for extending the present studies as will the future prospect of accelerated radioactive beams. This could lead to further Coulomb excitation and transfer reaction experiments to probe the energy level structure of extremely neutron rich nuclei at the limits of stability.

References

[Ajze 87] F. Ajzenberg-Selove Nucl. Phys. **A475** (1987) 1.

[Ajze 91] F. Ajzenberg-Selove Nucl. Phys. **A523** (1991) 1.

[Anne 87] R. Anne *et al.*, Nucl. Inst. and Meth. **A257** (1987) 215.

[Artu 69] A.G. Artukh *et al.*, Nucl. Phys. **A137** (1969) 348.

[Artu 70a] A.G. Artukh *et al.*, Phys. Letts. B **31** (1970) 129.

[Artu 70b] A.G. Artukh *et al.*, Phys. Letts. B **32** (1970) 43.

[Artu 70c] A.G. Artukh *et al.*, Nucl. Inst. and Meth. **83** (1970) 72.

[Audi 95] G. Audi and A.H. Wapstra, The 1995 Atomic Mass Evaluation, Nucl. Phys. **A595** (1995) 1.

[Azai 98] F. Azaiez *et al.*, Nuclear Structure '98, Gatlinburg, Tennessee, USA (1998).

[Azum 79] R.E. Azuma *et al.*, Phys. Rev. Lett. **43** (1979) 1654.

[Bala 77] D.P. Balamuth *et al.*, Nucl. Phys. **A290** (1977) 65.

[Balt 77] T. Baltakmens, Nucl. Inst. and Meth. **142** (1977) 535.

[Baum 89] P. Baumann *et al.*, Phys. Rev. C **39** (1989) 628.

[Bazi 93] D. Bazin and O. Sorlin, Programme LISE (1993), unpublished.

[Bazi 95] D. Bazin *et al.*, Phys. Rev. Lett. **74** (1995) 3569.

[Beau 92] C.W. Beausang *et al.*, Nucl. Inst. and Meth. **A313** (1992) 37.

[Bert 89] G.F. Bertsch et al., Phys. Rev. C **39** (1989) 1154.

[Beth 68] H.A. Bethe, Ann. Rev. Nucl. Sci. **21** (1971) 93.

[Bevi 69] P.R. Bevington, *Data Reduction and Error Analysis for the Physical Sciences*, Mcgraw Hill (1969).

[Blan 95] B.Blank et al., Phys. Rev. Lett. **74** (1995) 4611.

[Bohr 75] A. Bohr and B. Mottelson, *Nuclear Structure*, Benjamin Publishers, Reading, (1975) Vol 2, p. 592.

[Borr 83] V. Borrel et al., Z. Phys. **A314** (1983) 91.

[Bowm 74] J.D. Bowman et al., Phys. Rev. C **9** (1974) 836.

[Brow 86] B.A. Brown, A. Etchegoyen, W.D.M. Rae, OXBASH, The Oxford-Buenos-Aires-MSU shell model code, Michigan State University Cyclotron Laboratory Report No. **524**(1988).

[Brow 88] B.A. Brown et al., Annals of Physics **182** (1988) 191.

[Camp 75] X. Campi et al., Nucl. Phys. **A251** (1975) 193.

[Catf 89] W.N. Catford et al., Nucl. Phys. **A503** (1989) 263.

[Cern 66] J. Cerny et al., Nucl. Inst. and Meth. **45** (1966) 447.

[Chun 76] W. Chung, Ph.D. Thesis, Michigan State University (1976) (unpublished).

[Curt 86] M.S. Curtin et al., Phys. Rev. Lett. **56** (1986) 34.
         M. Samuel et al., Phys. Rev. C **37** (1988) 1314.

[Desc 95] P. Descouvemont, Nucl. Phys. **A581** (1995) 61.

[Detr 79] C. Detraz et al., Phys. Rev. C **19** (1979) 164.

[Detr 83] C. Detraz et al., Nucl. Phys. **A394** (1983) 378.

[Dufo 84] J.P. Dufour et al., Z. Phys. A **319** (1984) 237.

[Dufo 86] J.P. Dufour et al., Z. Phys. A **324** (1986) 487.

[Dufo 88] J.P. Dufour *et al.*, Phys. Letts. B **206** (1988) 195.

[Endt 90] P.M. Endt, Nucl. Phys. **A521** (1990) 1.

[Fede 79] P. Federman and S. Pittel Phys. Rev. C **20** (1979) 820.

[Ferm 34] E. Fermi, Z. Phys. **88** (1934) 161.

[Fifi 82] L.K. Fifield *et al.*, Nucl. Phys. **A385** (1982) 505.

[Fifi 85] L.K. Fifield *et al.*, Nucl. Phys. **A437** (1985) 141.

[Forn 97] B. Fornal *et al.*, Phys. Rev. C **55** (1997) 762.

[Frei 84] H. Freiesleben and J.V. Kratz, Phys. Rep. **106** (1984) 1.

[Fuku 92] N. Fukunishi *et al.*, Phys. Letts. B **296** (1992) 279.

[Gamt 36] G. Gamow and E. Teller, Phys. Rev. **49** (1936) 895.

[Gelb 78] G.K. Gelbke *et al.*, Phys. Rep. **42** (1978) 312.

[Gill 86] A. Gillibert *et al.*, Phys. Letts. B **176** (1986) 317.

[Gilm 95] G. Gilmore and J. Hemingway *Practical γ-ray Spectrometry*, John Wiley and
Sons Inc., NewYork (1995).

[Goul 75] F.S. Goulding and B.G. Harvey, Ann. Rev. Mod. Phys. **25** (1975) 167.

[Grei 75] D.E. Greiner *et al.*, Phys. Rev. Lett. **35** (1975) 152.

[Grzy 95] R. Grzywacz *et al.*, Phys. Letts. B **355** (1995) 439.

[Guil 84] D. Guillemaud-Mueller *et al.*, Nucl. Phys. **A426** (1984) 37.

[Guil 85] D. Guillemaud-Mueller *et al.*, Z. Phys. A **322** (1985) 415.

[Guil 89] D. Guillemaud-Mueller *et al.*, Z. Phys. A **332** (1989) 189.

[Guil 90] D. Guillemaud-Mueller *et al.*, Phys. Rev. C **41** (1990) 937.

[Hans 93] P.G. Hansen, Nucl. Phys. **A553** (1993) 89c.

[Harv 85] B.G. Harvey, Nucl. Phys. **A444** (1985) 498.

[Haus 88] P.E. Haustein (ed.) Atomic Data and Nuclear Data Tables **39** (1988) 185.

[Henc 94] M. Hencheck *et al.*, Phys. Rev. C **50** (1994) 2219.

[Hoat 86] S. Hoath, Nucl. Inst. and Meth. **A248** (1986) 287.

[Hube 78] G. Huber *et al.*, Phys. Rev. C **18** (1978) 2342.

[Ibbo 98] R.W. Ibbotson *et al.*, Phys. Rev. Lett. **80** (1998) 2081.

[Klot 93] G. Klotz *et al.*, Phys. Rev. C **47** (1993) 2502.

[Knol 89] G.F. Knoll, *Radiation Detection and Measurement*, John Wiley and Sons Inc.,
NewYork (1989).

[Koba 88] T. Kobayashi *et al.*, Phys. Rev. Lett. **60** (1988) 2599.

[Kran 88] K.S. Krane, *Introductory Nuclear Physics*, John Wiley and Sons Inc., NewYork
(1988).

[Lang 85] M. Langevin *et al.*, Phys. Lett. B **250** (1990) 19.

[Leak 68] J.W. Leake, Nucl. Inst. and Meth. **63** (1968) 329.

[Leak 80] J.W. Leake, Nucl. Inst. and Meth. **178** (1980) 287.

[Lee 56] T.D. Lee and C.N. Yang, Phys. Rev. **104** (1956) 204.

[Lewi 89] M. Lewitowicz *et al.*, Nucl. Phys. **A496** (1989) 477.

[Lewi 94] M. Lewitowicz *et al.*, Phys. Letts. B **332** (1994) 20.

[Lewi 96] M. Lewitowicz, private communication.

[Lind 75] P.J. Lindstrom *et al.*, Lawrence Berkeley Laboratory Report (1975) LBL-3650.

[Livi 37] M.S. Livingston and H.A. Bethe Rev. Mod. Phys. **9** (1937) 261.

[Meye 75] S.Meyer, Data Analysis for Scientists and Engineers, Wiley, NewYork, 1975.

[Mill 75] D.J. Millener and D. Kurath, Nucl. Phys. **A255** (1975) 315.

[Moto 95] T. Motobayashi et al., Phys. Letts. B **346** (1995) 9.

[Muel 88] A.C. Mueller et al., Z. Phys. A **330** (1988) 63.

[Muel 90] A.C. Mueller et al., Nucl. Phys. **A513** (1990) 1.

[Muel 91] A.C. Mueller et al., Nucl. Inst. and Meth. B **56/57** (1991) 559.

[Muel 92] A.C. Mueller, Nucl. Phys. **A538** (1992) 321c.

[Muss 84] J.A. Musser and J.D. Stevenson, Phys. Rev. Lett. **53** (1984) 2544.

[Nann 80] H. Nann et al., Phys. Letts. B **96** (1980) 261.

[Nils 55] S.G. Nilsson, Mat. Fys. Medd. Dan. Vid. Selsk **29** (1955) No.16.

[Nole 77] J.A. Nolen et al., Phys. Lett. B **71** (1977) 314.

[Olne 82] J.W. Olness et al., Nucl. Phys. **A373** (1982) 13.

[Orr 89] N.A. Orr et al., Nucl. Phys. **A491** (1989) 457.

[Orr 91] N.A. Orr et al., Phys. Letts. B **258** (1991) 35.

[Ozaw 95] A. Ozawa et al., Nucl. Phys. **A592** (1995) 244.

[Paul 33] W. Pauli *Rapports du Septiéme Conseil de Physique Soway*, Brussels (1933).

[Poug 86] F. Pougheon et al., Europhys. Lett. **2**, (1986) 505.

[Pove 87] A. Poves and J. Retamosa, Phys. Letts. B **184** (1987) 311.

[Pove 94] A. Poves and J. Retamosa, Nucl. Phys. **A571** (1994) 1994.

[Prav 91] M.S. Pravikoff et al., Nucl. Phys. **A528** (1991) 225.

[Proc 95] Proc. Int. Symp. of Unstable Nuclei (Niigata, Japan; 1994) Nucl. Phys. **A588** (1995) 1.

[Ragn 81] I. Ragnarsson et al., Physica Scripta **24** (1981) 215.

[Raim 96] G. Raimann et al., Phys. Rev. C **53** (1996) 453.

[Reed 91] P.L. Reeder et al., Phys. Rev. C **44** (1991) 1435.

[Rega 97] P.H. Regan et al., Acta Physica Polonica B **28** (1997) 431.

[Roek 74] E. Roeckl et al., Phys. Rev. C **10** (1974) 1181.

[Ryka 95] K. Rykaczewski et al., Phys. Rev. C **52** (1995) R2310.

[Sain 87] M.G. Saint-Laurent, Nucl. Inst. and Meth. B **26** (1987) 1273.

[Saku 98] H. Sakurai et al., Second International Conference on Exotic Nuclei and Atomic Masses, Shanty Creek Resort, Bellaire, Michigan, USA (1998).

[Schm 84] K.H. Schmidt et al., Z. Phys. A **316** (1984) 19.

[Schm 87] K.H. Schmidt et al., Nucl. Inst. and Meth. A **260** (1987) 287.

[Shal 53] A. De-Shalit and M.Goldhaber Phys. Rev. **92** (1953) 1211.

[Shel 76] R. Sheline, CERN Publication 76-13 (1976) 351.

[Soko 97] E.A. Sokol et al., Nucl. Inst. and Meth. A **400** (1997) 96.

[Stor 83] M.H. Storm et al., J. Phys. G **9** (1983) L165.

[Suho 98] J. Suhonen, private communication.

[Symo 79] T.J.M. Symons et al., Phys. Rev. Lett. **42** (1979) 40.

[Tani 85] I. Tanihata et al., Phys. Rev. Lett. **55** (1985) 2676.

[Tani 88] I. Tanihata, Nucl. Phys. **A488** (1988) 113.

[Tani 96] I. Tanihata, J. Phys. G **22** (1996) 157.

[Tara 97a] O. Tarasov et al., Phys. Letts. B409 (1997) 64.

[Tara 97b] O. Tarasov, private communication.

[Tara 98] O. Tarasov et al., Nucl. Phys. **A629** (1998) 605.

[Teng 92] O. Tengblad et al., Z. Phys. A **342** (1992) 303.

[Thib 75] C. Thibault *et al.*, Phys. Rev. C **12** (1975) 644.

[Till 93] D.R. Tilley *et al.*, Nucl. Phys. **A565** (1993) 1.

[Till 95] D.R. Tilley *et al.*, Nucl. Phys. **A595** (1993) 1.

[Viei 86] D.J. Vieira *et al.*, Phys. Rev. Lett. **57** (1986) 3253.

[Viyo 79] Y.P. Viyogi *et al.*, Phys. Rev. Lett. **42** (1979) 33.

[Volk 89] V.V. Volkov, *Treatise on Heavy Ion Science*, Edited by D.A. Bromley, Plenium
Press, New York, Vol 8, (1989) 101.

[Warb 89] E.K. Warburton and D.J. Millener, Phys. Rev. C **39** (1989) 1120.

[Warb 90] E.K. Warburton, J.A. Becker and B.A. Brown, Phys. Rev. C **41** (1990) 1147.

[Watt 81] A. Watt *et al.*, J. Phys. G **7** (1981) L145.

[West 79] G.D. Westfall *et al.*, Phys. Rev. Lett. **43** (1979) 1859.

[Wilc 73] K.H. Wilcox, Phys. Letts. **30** (1973) 866.

[Wild 80] B.H. Wildenthal and W. Chung, Phys. Rev. C **22** (1980) 2260.

[Wild 84] B.H. Wildenthal, Progress in Particle and Nuclear Physics **11** (1984) 5.
B.H. Wildenthal and B.A. Brown, Annual Review of Nuclear and Particle Science
38 (1988) 29.

[Wood 85] C.L. Woods, Nucl. Phys. **A437** (1985) 454.

[Wout 88] J.M. Wouters *et al.*, Z. Phys. A **331** (1988) 229.

[Wu 57] C.S. Wu *et al.*, Phys. Rev. **105** (1957) 1413.